12-2021

Structure Analysis of Soft Energy Materials using Neutron Scattering

Luke A. Heroux
University of Tennessee, Knoxville, lheroux@vols.utk.edu

Recommended Citation

Heroux, Luke A., "Structure Analysis of Soft Energy Materials using Neutron Scattering. " PhD diss., University of Tennessee, 2021.
https://trace.tennessee.edu/utk_graddiss/7058

To the Graduate Council:

I am submitting herewith a dissertation written by Luke A. Heroux entitled "Structure Analysis of Soft Energy Materials using Neutron Scattering." I have examined the final electronic copy of this dissertation for form and content and recommend that it be accepted in partial fulfillment of the requirements for the degree of Doctor of Philosophy, with a major in Materials Science and Engineering.

Mark, D, Dadmun, Major Professor

We have read this dissertation and recommend its acceptance:

Claudia J. Rawn, Gila E. Stein, Katharine L. Page

Accepted for the Council:

Dixie L. Thompson

Vice Provost and Dean of the Graduate School

(Original signatures are on file with official student records.)

Structural Analysis of Soft Energy Materials using Neutron Scattering

A Dissertation Presented for the

Doctor of Philosophy

Degree

The University of Tennessee, Knoxville

Luke Heroux

December 2021

Acknowledgements

Thank you most to my family, especially, my wife Jennifer, son Isaiah, and daughter Rosalen, and to my parents Renata and David. You have been my foundation through all my studies, and I could not have managed without your understanding and support.

Thank you as well to Dr. Mark Dadmun and the entire Dadmun group at UTK-Chemistry for help in sample prep, long nights on experiments and many discussions. Additional gratitude to a multitude of people at Oak Ridge National Laboratory, and especially within Neutron Sciences. This was an effort that took the cooperation of countless coworkers to accomplish, and I would not have been able to complete it without the support of and many discussions with so many of you along the way. I also appreciate all the support from everyone in the Breakthrough Electrolytes for Energy Storage - Energy Frontier Research Center, that has brought me in contact with several people to discuss advancement of these experiments and defining projects in soft matter energy fields. Finally, in memorandum of some of my biggest supporters, my grandparents George and Lucille Callahan, who were so supportive of me from the very beginning; and to my mentors Michael Agamalian, for encouraging me to embark down this path with him, and Jack Carpenter, for all the thoughtful discussions.

Abstract

The structure of several materials important in the development of sustainable energy have been determined using multiple neutron scattering methods. Elucidating the structure-property relationships of these conductive polymer blends, microemulsions, and deep eutectic solvents (DES) provides correlation of material assembly to electro-chemical performance.

Conductive films of poly(3,4-ethylenedioxythiophene):poly(styrene sulfonate) (PEDOT:PSS) are found to organize into smaller domains with the addition of dimethyl sulfoxide(DMSO) to a pre-deposition solution. Addition of DMSO disrupts the aggregates and large domains within PEDOT:PSS, enabling alignment of the PEDOT fibrils within the PSS domains, and occurs in both spin-coated and spray-coated depositions. The spin-coated films have consistently smaller domain sizes, indicating the disruption of aggregates occurs when DMSO is added and the smaller domains in spin-coated films are due to faster evaporation rates of the deposited solution.

Microemulsions formed by mixing water, toluene, and an emulsifier of Tween-20® and 1-butonal create lamellar-like layers at surfaces potentially impacting charge transfer to electrodes. Layered structures are monitored for increased surface amphiphilicity and decreased water content in the emulsion. Decreased water in the emulsion results in decreased layer thickness, while increased amphiphilicity creates lamellae-like layers of nearly pure water and oil/emulsifier. The formation of these lamellae increase the surface area of the boundary between the water and the oil, creating a potential to increase charge transfer pathways.

Addition of a hydrogen bond acceptor, choline chloride(ChCl), to a hydrogen bond donor, glycerol, develops interactions between the molecules, forming a DES at 33% ChCl. With increased ChCl to the mixture, the glycerol interacts primarily with the chloride anion while the choline primarily interacts with other choline molecules. This assembly of potential hydrogen bond networks is crucial to the formation of the DES glyceline, where the dominant choline-choline interactions free the chloride ion to interact with the glycerol molecules.

Additionally, monitoring and controlling atomic vibrations in crystals integral to the execution of ultra-small-angle neutron scattering experiments offers insight to increase the signal-to-noise in USANS instruments. The combination of these investigations demonstrate the utility and promise of multiple neutron scattering techniques to advance several important classes of materials in soft matter energy research.

Table of Contents

List of Tables

List of Figures

Chapter I Introduction

Research to advance the performance of energy related materials for improved sustainability is constantly evolving, including interest in materials for a hydrogen economy, improved efficiency of energy transfer processes and improved methods of analysis.[1-3] Recently, energy related materials research has focused on sustaining energy supply from both large networks such as a national grid and more local efforts such as household and personal electronics.[4,5] Organic materials play a significant role in the sustainability of future energy technologies through power generation and storage.[6] Research on soft matter as energy materials has increased significantly over the past decades with growing interest in their use in thermoelectrics, large scale energy storage, and personal power supplies[7-9]. While some applications utilize conjugated polymers in thin films, others use materials that form hydrogen bond networks to transfer energy.[5,6] The rational improvement of these materials is largely dependent on the structures they form, which in turn center on the nature of hydrogen within them.

Neutron Scattering as a tool to study energy related materials began in 1946, when Wollan and Shull demonstrated neutron Bragg diffraction could be used to study the atomic structure of crystalline materials, analogous to existing approaches based on X-ray Bragg Scattering methods.[10-14] Modern neutron scattering envelopes many additional methods, most with X-ray scattering counterparts, including several (like reflectometry and small angle scattering) that are used heavily for soft matter. Neutron scattering as a tool to examine soft materials is largely based on controlling the contrast between components where substituting the hydrogen (H) atoms with deuterium, ^{2}H or D, known as deuteration, increases this contrast between components.[15] Contrast is quantified by the difference in neutron scattering length density (SLD) of materials, a gauge of the extent of scattering from neutrons interacting with materials and provides an important tool in using neutron scattering to measure the structure and dynamics of organic materials. Neutrons have been used to monitor the structure of a variety of materials, especially in energy related materials such as batteries, photovoltaics, biofuels, and capacitors.[2-4,8,16,17]

Neutron Scattering

Neutron scattering includes a broad range of techniques measuring various characteristics of both inorganic materials and soft matter.[18] The breadth of these applications offers the ability to measure the structure and dynamics over several ranges of length scales, from macroscopic (microns) to nanoscale (nm) to atomic structures (Å) as shown in Figure I.1a, as well as providing techniques to characterize surface structures and dynamics.[19-24] Each of these measurements depends on using different techniques such as small-angle neutron scattering (SANS) , Figure I.1c, including very- (VSANS), Figure I.1c, and ultra- small-angle neutron scattering (USANS), Figure I.1b, and wide-angle neutron scattering (WANS), Figure I.1d, commonly referred to as neutron diffraction, to access a large range of length scales.[19-24] Similarly, reflectometry probes depth dependent structures and inelastic scattering provides techniques such as spectrometry and spin echo to monitor material dynamics.[25-30]

Regardless of the technique, the scattering of a neutron by a material involves a similar physical process to the scattering of X-rays by a material. In 1913, Bragg discovered that X-rays directed at a material are scattered from crystalline structures, where the angle of

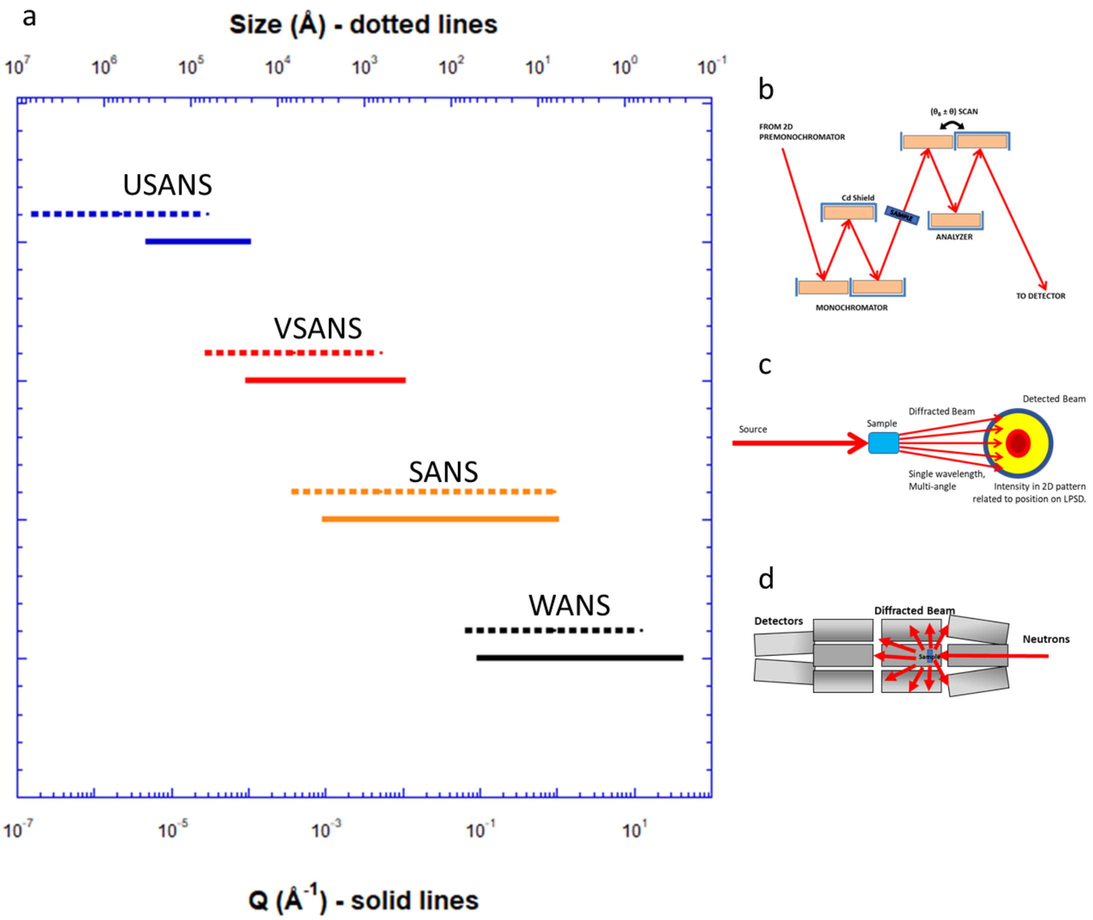

Figure I.1– a) Plot of Q-range (bottom axis-solid lines) and length scales (top axis-dotted lines) measured by various neutron scattering techniques represented on right side of plot, b) USANS, c) SANS and VSANS, d) WANS.

scattering, θ, depends on the wavelength, λ, the order of the scattering, n, and the interplanar spacing , d, as defined in Bragg's law, $n\lambda = 2dsin(\theta)$. [11,14] This relationship was later generalized to correlate the characteristic distance, or distance (d) between scattering objects, of a material to the shift in momentum of the scattered particle, Q, by the relation of $d = \frac{2\pi}{Q}$, where $Q = \frac{4\pi \sin(\theta)}{n\lambda}$. This theory was adapted for neutrons by Wollan and Shull to also determine Bragg scattering of crystalline structures.[10-13] An important effect of X-ray scattering is that the X-rays interact with the electron cloud of the atoms, where the strength of X-ray scattering for a specific atom depends on the number of electrons; therefore the scattering of X-rays from an atom increases with its atomic weight (Z number).[14] A distinction of the scattering of neutrons from that of X-rays is that neutrons interact with the nuclei of an atom, where the strength of scattering depends on an atom's neutron scattering length, which does not vary with Z number.[11] Both techniques allow measurements on a variety of structures, but each can be used to study different materials, such as X-ray scattering for materials with heavier elements and neutron scattering for materials that include hydrogen.[11,14,15]

The neutron diffraction technique developed by Wollan and Shull increased interest in this field of neutron scattering, which led to the development of research reactors for neutron scattering experiments.[11,31] This allows for the delivery of constant wavelength neutron beams to a sample.[31] This was followed many decades later by accelerator-based pulsed sources that use time-of-flight to keep track of the wavelengths of neutrons that are scattered.[32-34] The wavelength in Bragg's Law is replaced by the time it takes a neutron to travel to a detector from the point of its generation, with corrections for the neutron mass and Planck's constant, enabling the simultaneous measurement of the scattering of neutrons with multiple wavelengths.[34] Diffraction measurements performed with single wavelength neutrons measure scattered neutrons over a range of scattering angles to vary Q.[10,24] The development of time-of-flight neutron instruments allows the measurement of the scattering of more neutrons with a breadth of wavelengths, increasing the signal-to-noise of the scattering experiment.[32,34] This also increases the Q-range, allowing total scattering angle coverage and wide-angle neutron scattering in a Q-range of 0.5 Å^{-1} up to 32 Å^{-1}.[24]

Furthermore, specific scattering geometries were readily designed to measure the scattering at lower Q-ranges, opening up techniques to monitor structure on larger length scales.[33] These small-angle scattering geometries create a long focal distance of the scattering particles, so the resolution of length scales studied increases. This increase in resolution allowed the measurement of a signal from a material in Q-ranges of 10^{-3}Å^{-1} up to 1 Å^{-1}.[33] This Q-range overlaps that of wide-angle neutron scattering, but extends it to orders of magnitude lower Q, which correlates to larger molecular sizes, 6 Å - 6280 Å. More recently SANS has been extended to capture scattering at even lower Q through the use of focusing optics, longer distances between the sample and the detectors as well as additional detector arrangements that allow extension of the measured Q-range to 10^{-4} Å^{-1}.[21,22,35]

However, in order to monitor the structure of a material at even larger scales and correlate to complementary techniques such as electron microscopy and light scattering, further instrumentation development was required.[19,23] To measure the structure of a material with neutron scattering at even lower Q, new ultra-small-angle neutron scattering (USANS) instruments based on interferometry were developed based on a double crystal design.[19,23,35] In this instrument, a set of matching large single-crystals scan a reflected beam across a sample and measure the shift in the intensity of the scattered neutrons, extending the measured Q below 10^{-5} Å^{-1}, correlating to 10's of microns in length.[23,33,36]

Additional neutron techniques have also been developed and applied to determine the structure and dynamics of soft matter.[25-30,37] Neutron reflectometry, Figure I.2, is a technique similar to USANS in that a reflection of incident neutrons from the sample is monitored as it is then detected at a given scattered angle, 2θ.[37] However, in neutron reflectometry the incoming neutron, at an angle of θ_{in}, is reflected off an interface at an angle of θ_{out}, that neighbors the material of interest or exists in the material itself. Due to the low incident angle, neutron reflectometry monitors the structure of a material perpendicular to a surface, which is critical to understanding how materials interact with their surrounding environment.[25,37]

While this discussion has been on elastic scattering techniques where the energy of the scattered neutron is the same as the energy of the incident neutron, there is an additional field of techniques using inelastic scattering.[26-30] In these techniques, the change in energy of the scattered neutron is related to the dynamics of the material studied.[26,27] Overall, neutron scattering is a robust technique to measure the structure and dynamics of a range of materials that are of interest for the development of energy related technologies, where

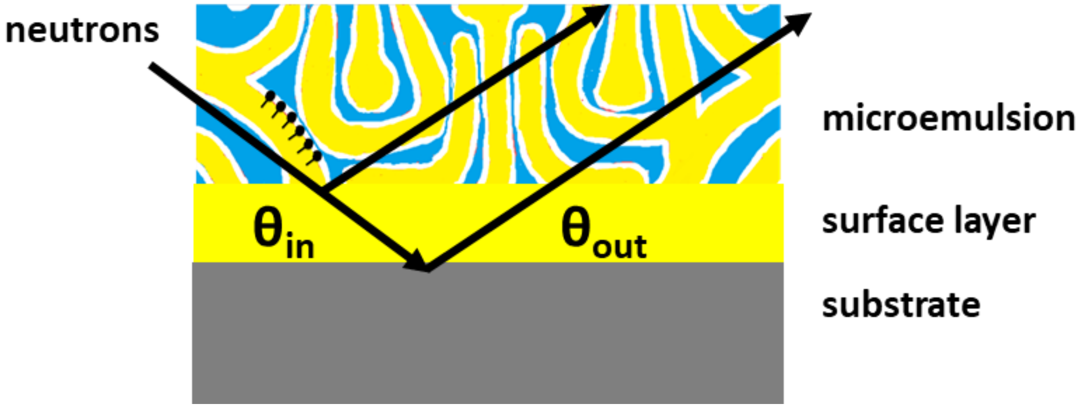

Figure I.2 – Sketch of neutron reflectivity through a bicontinuous microemulsion. Neutrons enter the emulsion at a defined angle, θ_{in}, and reflect off the substrate and surface structures at a detected angle, θ_{out}.

often the use of multiple scattering techniques offer a more thorough understanding of the material under different conditions, including those that are relevant to their operation.

Macromolecular and Nanoscale Structures

Small-angle Neutron Scattering (~1Å-200nm)

Small-angle neutron scattering (SANS) is utilized to measure structural changes of a range of macromolecular materials including polymers, proteins, micelles, and emulsions.[3,16,35,38-42] This technique focuses on scattering in low-Q by measuring the intensity of scattered neutrons at the smallest angles from a material, which relates to structures at relatively large length scales (compared to the size of the neutron) in real space.[20,43] In this discussion, Q is a measure of the momentum change of a scattered neutron, measured in inverse angstroms, $Å^{-1}$, and θ is the angle of the scattered neutron measured. The scattering angle is measured relative to the center of the transmitted beam (beam that travels directly through a sample material), and is normally detected isotropically in a 2π radius, which when summed gives a 1-dimensional (point-space) plot of intensity vs Q. Measurements of low-Q allow the determination of changes in relatively large structures, such as conjugated polymer chains or protein networks. In studying the structure of soft materials with SANS, deuteration of specific polymers or molecules enables control of the contrast between components of a multi-component system.[15,16,38-42] This allows the determination of the structure and assembly of the individual components in the whole structure, including the formation of aggregates, where several molecules may combine to form a larger structure. Interest in SANS continues to grow as research on the structure of a broad range of materials has driven this technique to be an indispensable tool for measuring organic material structures. [18,34]

In particular, SANS have been used to determine the structure and assembly of organic electronic materials such as ionic liquids, thermoelectrics, and microemulsions.[16,38,40,41] Some organic electric materials have exhibited high Seebeck coefficients, a measure of the ability of a thermoelectric material to convert a change in temperature into a voltage, with high electrical conductivity and low thermal conductivity.[44,45] These organic electronics often consist of polymeric mixtures in the form of conjugated polymers, polymer blends or even polymer nanocomposites, but may also include salts and conductive organic solids.[3,41,44,45] These materials are also used in light-emitting diodes, photovoltaics, and even transistors.

Very Small-angle Neutron Scattering(~1nm-500nm)

Additionally, SANS techniques have been expanded to measure the scattering at smaller Q-regions where the characteristics of even larger structures can be monitored.[22] Modifications to instrumentation can extend the Q-range available for the scattering experiments, where adding detectors or extending the distance between sample and detector offers access to these lower Q-ranges and improves data collection. This extension is often termed "very-small-angle neutron scattering" (VSANS) experiments and instruments.[22] The addition of these equipment modifications primarily allow access to lower-Q-range, but also minimizes the measuring time for a scattering curve over multiple orders of magnitude in Q which relates to the structure of the material of interest over a broad range of length scales.[22]

Ultra-small-angle Neutron Scattering (~100nm-50μm)

Access to the structure of a material of interested at even larger length scales is available due to the development of ultra-small-angle neutron scattering (USANS).[35] Ultra-small-angle scattering (USAS) has been utilized to determine structures of micron sized constructs for many years. Analogous to early interferometer instruments, and further developed by Bonse and Hart, USAS has provided structural information of materials over a unique size range that many other methods cannot access.[36]

Bonse and Hart developed USAS to examine the structure of large macromolecules in 1965.[36] This theory was applied to neutron instrumentation, USANS, over 20 years later and continues to be developed and refined.[19, 23,46-50] This technique is slightly different from SANS and VSANS, in that rather than measuring the scattered neutron in the direct geometry of the scattering event, USANS relies on a shift in the wavelength of the scattered neutrons from a scattering event.[22,36,46,48] In the Bonse-Hart arrangement a channel cut monochromator crystal controls the input of the neutron incident beam to the scattering sample, then a matching analyzer crystal is utilized to detect the wavelength shift of the scattered neutrons.[36] By rotating the analyzer through a 2θ scattering angle, the wavelength shift is measured, and the total intensity of the scattered neutrons are measured over a Q-range that is defined by the angle of the analyzer crystal.[19,47] This shift is determined by monitoring the difference of rocking curves of the crystals with and without a sample between them. The intensity of this shift is then used to build a scattering curve in 2-dimensional (slit) space which can be converted to point space to align with a traditional 1-dimensional scattering plot.[46,48]

The channel cuts in the crystals that were developed by Bonse and Hart create a reflective pathway for X-rays (and neutrons) to "bounce" back and forth in both the monochromator and analyzer crystals.[36] This repeated reflection allowed loss of tailing neutrons that would create wings in the rocking curves. Removing the wings was a critical step in reducing the noise in the scattering data and extending these measurements to higher Q, so that the USANS data can be correlated to SANS data.[46,48] Additionally, in USANS, Agamalian determined that cutting the monochromator and analyzer crystals so that the incident reflection is separated from the final reflection further reduced these tails and parasitic reflections from the back face of the monochromator crystal.[48] Adding neutron shielding cadmium between these reflections additionally reduced the parasitic scatter and improved the signal-to-noise ratio of the scattered data, a measurement of quality of the data.[19, 48] Application of this technique at a time-resolved source allows specific neutron wavelengths to be analyzed.[19,47] By focusing on a single wavelength, the signal-to-noise ratio is further improved and allows the natural vibrations of the monochromator and analyzer crystals to be observed. The match between these crystals, which is measured by aligning the monochromator and analyzer at a series of wavelengths, establishes the resolution of the USANS instrument. The deviations in this measurement are then associated with the atomic vibrations within the crystals.[48,49,50] Decreased atomic vibrations allow improvements to the USANS technique, such as increased resolution and improved signal-to-noise and will increase the success of experiments in this field by improving the ability to measure small variations in the structure of soft matter.

With the development and refinement of neutron scattering techniques, research, and development of new materials for energy related applications will improve. USANS offers the opportunity to monitor the structure of soft matter at larger length scales, which can be highlighted by replacing hydrogen with deuterium.[39,51,52] This opens the possibility of measuring the structure of organic materials on length scales that range from 100nm up to 50 μm. USANS is often used to expand on measurements that use SANS and light scattering by connecting and overlapping the measured structure from these other techniques; SANS (~1Å-200nm), VSANS (~1nm-500nm), and light scattering (~800nm-100μm).[22,35,53]

Molecular and Atomic Scale Structures

Wide angle neutron scattering, commonly referred to as neutron diffraction (ND) measures the intensity of the scattered neutrons at wider angles, monitors structure on a much more local length scale, and has been used since Wollan and Shull first observed neutron scattering.[11,13,14] This method measures the total scattering of a system, where changes in the structure of a material will result in shifts in the intensity and position (scattering angle) of Bragg peaks based on the lattice parameters or other features of ordered structures in the material.[11] ND monitors the scattering of neutrons over a large range of Q, quantifying interactions over small length scales (a few Å) such as atomic structures, crystalline networks, and solvation groups.[24] , ND has been used to measure the structure of ordered liquids and solutions.[54,55,56] These materials form structures that may create networks based on non-covalent interactions such as hydrogen bonds and van der

Waal interactions in a system.[4,6, 54,55] ND determines the structure of these systems and (when coupled with sample environments) how changes in temperature, pressure, and composition may alter their interactions and assembly. [54,55] As discussed with the other neutron scattering methods, replacing hydrogen with deuterium (isotopic substitution) increases the specificity of the measured structural changes.[15] Similarly, deuteration of the solvent, crystalline material or both will help determine the morphology of conductive networks formed. [54,55]

Monitoring Material Dynamics

While elastic scattering methods (diffraction and SANS) are utilized to determine the structure of materials, inelastic scattering methods measure the dynamics of a system by monitoring the change in the energy of a scattered neutron.[26-30] Research on energy-related materials such as ionic liquids and deep eutectic solvents, DES, using techniques including back scattering spectroscopy, BSS, and neutron spin echo, NSE, have proven beneficial in the development of these materials.[57,58] Neutron BSS quantifies the length scale dependent changes in system dynamics by measuring the transfer of the energy of the scattered neutrons from the sample that are reflected from an analyzer crystal and then detected.[26-28] This reflection of the neutron back towards the sample material allows the transfer of energy in the sample to be resolved. Neutron spin echo experiments monitor how the spin of a neutron changes its trajectory and energy after being scattered from a material.[29,30] These measurements therefore quantify the dynamics of the sample on longer time scales. Inelastic scattering has provided insight into the dynamics in deep eutectic solvents, including work by Wagle, *et al.*, who measured the dynamics of a glycerol-choline chloride mixture using BSS and NSE.[57,58] These inelastic studies give insight to how the molecules in the mixture, specifically the DES, are interacting within the network of hydrogen bonds.[58]

Structure near Surfaces and Interfaces

Often a material will assemble into a different structure near a hard surface or interface than exists in the bulk. Reflectometry monitors the structure of soft matter at a surface or interface and elucidates how that assembly may differ from that in the bulk.[25,37] Primarily discussed here as neutron reflectometry, NR, involves the reflection of neutrons from an interface or surface, where the structure of the material perpendicular to the interface is then determined from the reflectivity curve.[37]

The intensity of the reflected neutrons is measured as a function of the scattering angle. This technique penetrates surfaces that are 100's and even 1000's of angstroms thick and monitors the structure of the material near the surface or interface. Variation in structure near a surface are important in organic electronics as this may impact charge transport in the sample near a surface or at an electrode.[59-61] Examining materials using a combination of these techniques creates a full picture of the structure and dynamics of materials for a broad range of energy related applications.

Thermoelectrics

Thermoelectrics are materials that absorb thermal energy and use the deviations in temperature to produce electron flow. These are often used industrially in photovoltaic solar panels and sensors and have become essential to the development of a sustainable energy supply.[62,63] Historically, thermoelectrics have been produced using inorganic materials. While these currently demonstrate a higher efficiency of energy production, they are also expensive to obtain and manufacture.[2] Organic thermoelectrics pose an alternative to their inorganic counterparts, where organics are often readily produced, are flexible, durable, and renewable.[62-64] Research in organic electronic materials has recently focused on development of materials that are inexpensive to obtain and manufacture as well as materials that are sustainable. These may be developed not only for thermoelectric energy production, but to be environmentally and biologically safe.[44,45] This expands the possibility that these electronic devices are recyclable and may interact with the human body through heat transmission for either warming or cooling.[44] Promising organic materials for thermoelectrics often include conjugated polymers, polymer blends, and polymer nanoparticles, which are manufactured using common industrial techniques and maintain promising electrical properties.[38-45,63,64]

Conjugated Polymer Blends

Conjugated polymers in conductive polymer blends have become a topic of research for use in photovoltaics and thermoelectrics among other applications. These polymer blends, cast as conductive films, have become popular as potential alternatives to inorganic electronic materials.[9,16,40,44,63,65] While many polymers have low electrical conductivity, some such as Poly(3,4-ethylenedioxythiophene): poly(styrene sulfonate) (PEDOT:PSS) blends demonstrate promising electrical properties, including promising Seebeck values, S, a measure of the voltage produced from an induced thermal gradient in the material related to the conductivity, σ, by $\sigma = \frac{S}{cm}$.[41,42] The variation in the Seebeck value of conjugated polymer blends is related to changes in their structure as a result of deviation in processing techniques or procedures. Determining the structures of the polymer blend with these fabrication processes using several scattering techniques, combined with thermoelectric measurements, offer pathways to correlate the structure at both macro- and microscopic length scales to the electrical performance of the blend.[16,40,65]

Various techniques have been utilized to determine the structure of PEDOT:PSS, including electron microscopy, atomic force microscopy, neutron scattering and UV-vis spectroscopy.[40,65-69] These often correlate the structure of the polymer blend to the electrical performance of the material through thermoelectric analysis and have shown that increased conductivity is associated with organization of the polymers in the blend.[667-69] Small-angle scattering, from SANS to USANS, can be performed on PEDOT:PSS films by using deuterated PSS (dPSS) in this blend, which creates a contrast in the scattering length density of the PEDOT and the PSS.[16,40]

Solvent treatments, such as adding dimethyl sulfoxide (DMSO) or ethylene glycol (EG) to the pre-deposition solution of the polymer blend, have been used to increase the electrical performance of the PEDOT:PSS films. Increases in conductivity by 100 times have been reported for the addition of up to 7.5% DMSO and 5%EG to the pre-deposition solvent.[65-67] This increase in conductivity is measured with the addition of only 5% DMSO to the PEDOT:PSS polymer blend, which allows the thickness of the film to be consistent with a PEDOT:PSS film with no additive.[65]

Observation of the morphological changes in this system have shown that adding DMSO to the pre-cast polymer blend increases the conductivity, and therefore the Seebeck coefficient, of the film.[16,65-69] Structure changes of the cast film with and without a DMSO additive show how the polymer domains in the blend change in size.[16] However, the structure and behavior of these polymer blend films is not well understood. Therefore, structure of PEDOT:PSS blend films that are formed from varying fabrication procedures have been monitored to correlate blend morphology to performance. The changes in fabrication procedure include varying the amount of DMSO in the PEDOT:PSS pre-deposition solution and film casting methods. In terms of film casting methods, film structure formed from spin-coating are compared to films formed from other techniques that may be more industrially scalable, such as ultrasonic spray coating. Elucidating the impact of these coating methods on the structure and performance of the thermoelectric film provides insight that can drive improvement of fabrication methods and performance.

A series of ultra-small and small-angle neutron scattering measurements have been performed to monitor the changes in the size of the domains in films of the polymer blend PEDOT:dPSS. The addition of DMSO to the pre-cast blend shows a breakup of large polymer aggregates into smaller domains along with organization of fibrils within the domains. Additionally, comparison of spin and spray coating deposition methods shows that the disruption of these aggregates is independent of the film-casting method. Increased uniformity of fibrils and formation of smaller domains in the PEDOT:PSS polymer blend with the addition of DMSO and the spin-coated films can be associated with increased conductivity observed in previous measurements.

Microemulsions

One method to achieve improved and sustainable energy storage includes incorporating conductive microemulsions (ME) in redox flow batteries.[5,41] Microemulsions with a redox active component in an aqueous salt solution have become a topic of research for energy technologies in addition to their applications in health, medical and food industries.[5,70,71] The microemulsions that form in a water/surfactant/oil solution have been found to make charge transfer available both within the solution and between the solution and an electrode.[72,73] Past studies have focused on the increased charge transfer in the bulk material of the ME system, but only recently have studies been performed to determine how the structure of an emulsion with a redox active agent near an electrode affects the flow of electrical current, Figure I.3. [61,72,74] With this in mind, the structural changes of the ME near a surface will be monitored by neutron reflectometry as a function of ME composition and surface hydrophilicity. Understanding the organization of these structures offers insight into their assembly near similar electrodes that can provide opportunities to improve electrical performance. Surface layers that form between a bulk solution and a hard interface may improve or inhibit electron charge transfer from the solution to an active electrode and ion transfers across the surfactant boundaries which balance the conductivity of the system.

The structure of a series of microemulsions of deuterated water (D_2O), toluene, polysorbate-20 (TWEEN-20®), and 1-butanol on hydrophilic and amphiphilic surfaces. In these microemulsions, the TWEEN-20® and 1-butanol form a surfactant/co-

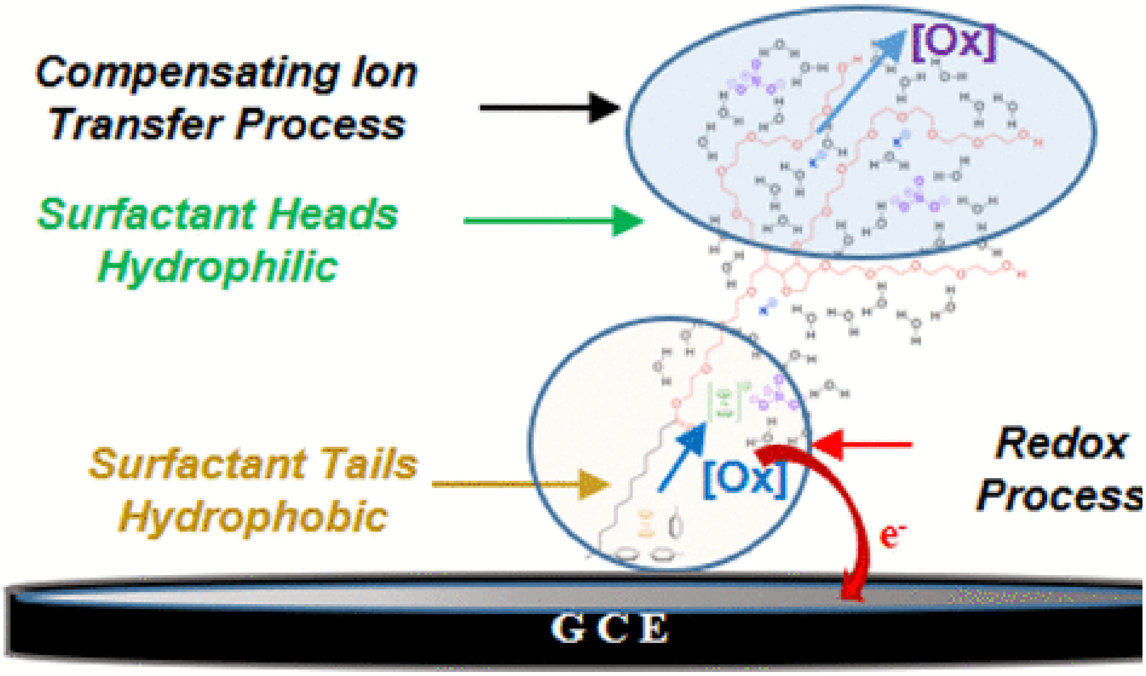

Figure I.3 – A representation of charge transfer from a gold coated electrode through a surfactant boundary in the presence of a redox active species, ferrocene.[72]

surfactant that forms a boundary between the oil (toluene) and water (D_2O) phases of the ME. When exposed to a hydrophilic or an amphiphilic surface these water/surfactant/oil phases form layers based on the preference of water or oil at the surface. The formation of these layers, which are measured using neutron reflectometry, creates a series of lamellae between the surface and the bulk material. The purity and thickness of these lamellae create pathways for charge transfer in the ME between the bulk solution and the electrode. A reduction of both purity and thickness of these lamellae may increase the ion transfer across the surfactant layer and electron transfer at the electrode surface. Therefore, observation of the variation in assembly of these layers, and hence the changes in surface structure, allow development of microemulsions with improved charge transfer.

Deep Eutectic Solvents

Expanding sustainable energy production also requires increased storage capabilities, where additional efforts to industrialize sustainable energy storage include improvement of flow battery materials and processes. These efforts require additional efforts to develop new and improved electrolytes, where one focus area includes ionic liquids and similar materials.[6,73,74] These solutions involve the dissolution of a salt with a low melting temperature liquid, which results a conductive fluid. The solvation of the salt often involves the formation of non-covalent interactions between the two components, which alters their assembly. While the solutions are well mixed at higher temperatures, the many solutions become ionic solids at room temperature.[73] Recent discoveries have shown that there are a class of these solutions, called deep eutectic solvents (DES), that remain liquid at relatively low temperatures.[74]

DES are similar to ionic liquids that are moisture stable fluids. DES are formed when a molecule that consists of an alcohol, amide, or carboxylic acid combined with large nonsymmetric ions with a low lattice energy are used as a hydrogen bond donor to dissolve a halide salt as a hydrogen bond acceptor.[76,77] A small number of halide salt and hydrogen bond donors that may be combined to create a DES were originally proposed by Abbott, *et al.*, Figure I.4.[6] These mixtures are initially immiscible at room temp, but once heated form a miscible solution, and then when cooled to room temperature form conductive liquids that maintain fluidity at substantially lower temperatures than the melting point of either of its components.[76-79] The ability for the DES to form a hydrogen bond network and maintain a liquid state increases the transport of ions and offers the opportunity for their use in energy storage.[54,78-81] However, it is not well understood how the hydrogen bond network varies with the addition of a salt, or what composition of a DES develop the most conductive system. For instance, Wagle, *et al.,* determined, using neutron BSS, that in the DES glyceline, a mixture of 33% choline chloride (ChCl) in glycerol, the dynamics of the choline molecule encompass larger displacements relative to those of the hydrogen bond donor, glycerol.[57] This is counterintuitive to expected behavior of fast-moving hydrogen bond donors on the macroscopic scale. Further understanding of the structure of the DES hydrogen bond network encompassing the glycerol and ChCl assembly can provide insight into the observed dynamic changes in this study.

Wide angle neutron diffraction is used to measure the structure factors of the DES's.[54,55] Changes in this structure factor determine the change in assembly of the DES as the composition varies. Previous studies suggest that the chloride anion of the ChCl

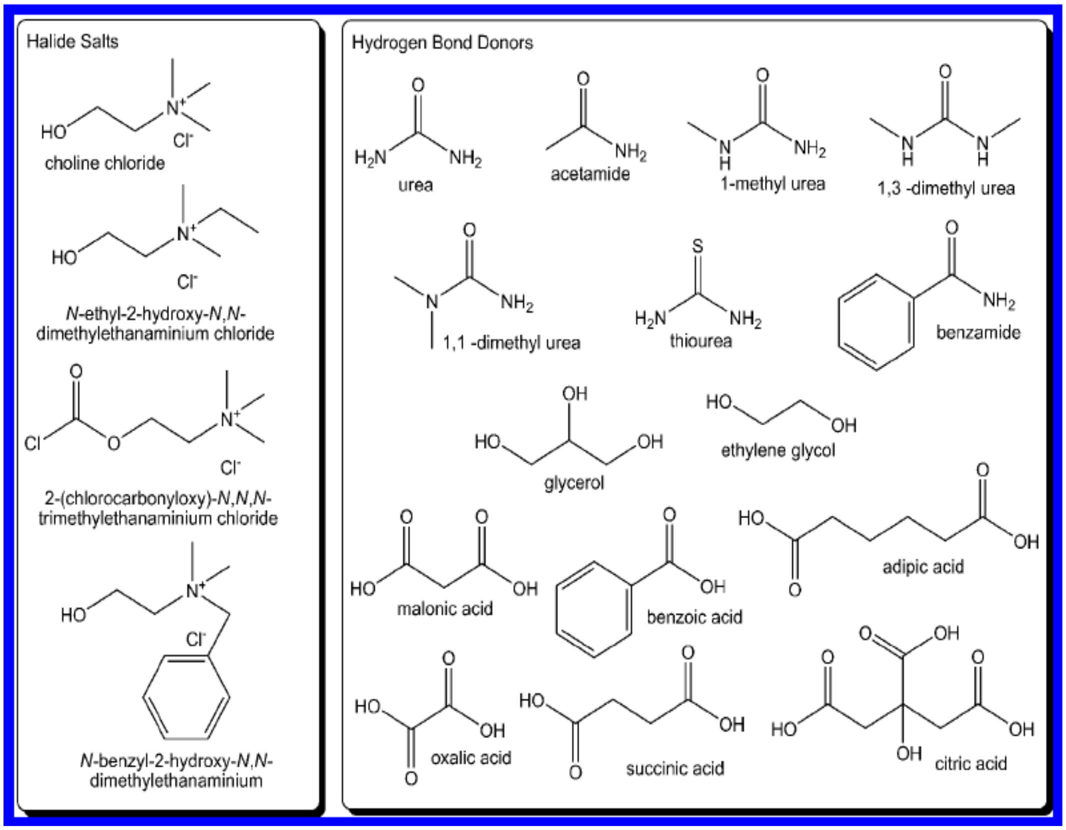

Figure I.4 – A sampling of halide salt (hydrogen bond acceptors) and hydrogen bond donors that are used in the formation of deep eutectic solvents.[6]

salt breaks up the glycerol hydrogen bond network formed in the solvent, such as glycerol or ethylene glycol.[54,55,57,58] Additionally, Holbrey, *et al.*, predict that the choline enters interstitial voids of the glycerol network at higher concentrations of ChCl.[55] However, the structures and networks formed by adding ChCl to these solvents has yet to be fully explored. Mixtures of the components of the DES with varying compositions from the pure solvent to the eutectic solution develop new interactions between the hydrogen bond donor, glycerol, and the hydrogen bond acceptor, ChCl. Changes in the Bragg scattering help us identify changes in the networks formed in the solution. Using deuterated components in these mixtures exemplifies the assembly of the particular molecules of interest. Analysis of the structure factors show that in ChCl:glycerol mixtures, the addition of ChCl causes intensity changes and shifts in Bragg peaks, which can be analyzed to provide insight into how the structure and network of the system adapt as the composition of the mixture approaches the reported eutectic point.[54,55]

The diffraction data is also analyzed in context of molecular dynamic simulations, which can be tailored for both variations in composition and in neutron contrast.[54] Matching the structure factors with molecular dynamic simulations enables precise analysis of the hydrogen bond network that forms in a DES through radial and spatial distribution functions. Combining neutron diffraction with molecular dynamics also improves the characterization of the hydrogen bond networks and the correlation of structural changes to the development of these networks.[54] The spatial analysis of these solutions shows how networks are formed, disrupted, and impeded within a DES. Specifically, in a ChCl:glycerol mixture, interactions between glycerol and the chloride anion form while simultaneously choline molecules primarily interact with other choline molecules. These measured transformations show how structural changes form exclusive interactions in a DES that may be predicted and can lead to improvements in electrochemical behavior.

Summary

Determination of the structures of energy relevant materials is necessary to understand and control their assembly and performance in targeted applications, as well as their integration into commercial products. Neutron scattering is useful in elucidating the structure of organic materials and advancing research and development of materials for energy related applications, such as photovoltaics and redox flow batteries. By exchanging hydrogen for deuterium (^2H or D) in an organic material, the contrast between components (whether atomic, nano or microscale) is increased in a system. This increased contrast enables a variety of characterizations including determining structure size and shape using ultra-, very-, and small-angle neutron scattering of materials such as polymer blends, determining structures formed at a conductive surface using neutron reflectometry, and determining formation and arrangement of hydrogen bonds using wide-angle neutron scattering. While all these methods are performed differently, all benefit from the contrast variation introduced through selectively deuterating the system. Neutron scattering remains a useful tool in the development of materials for energy relevant applications, especially soft matter (polymers, biological materials, liquid crystals) as used in energy storage materials such as redox flow batteries, and energy transfer devices like thermoelectrics and photovoltaics.

Therefore, neutron scattering is utilized in a series of studies that focus on a variety of energy materials, including controlling the structure and performance of PEDOT:PSS polymer blends, understanding the assembly of microemulsions at hard surfaces, and the development of structure in the mixtures that form deep eutectic solvents. Moreover, continued development of instrumentation, specifically improving USANS Q-resolution by reducing vibrations of monochromator and analyzer crystals, will improve the utility of neutron-based techniques to monitor the structure and dynamics of soft matter.

References

1. T. A.; Baker, G. A.; Tuckerman, M. E.; Savinell, R. F.; Sangoro, J. R. Deep Eutectic Solvents: A Review of Fundamentals and Applications. Chemical Reviews 2021, 121 (3), 1232-1285

2. Dudney N.J., Hagaman E.W., Veith G.M., Gill L.W., Sacci R.L., "Lithiated and Passivated Lithium Ion Battery Anodes", (2019).

3. Xie S., Zhang B., Mao Y., He L., Hong K., Bates F.S., Lodge T.P., "Influence of Added Salt on Chain Conformations in Poly(ethylene oxide) Melts: SANS Analysis with Complications", Macromolecules, 53, 7141-7149 (2020).

4. Hansen, B. B.; Spittle, S.; Chen, B.; Poe, D.; Zhang, Y.; Klein, J. M.; Horton, A.; Adhikari, L.; Zelovich, T.; Doherty, B. W.; Gurkan, B.; Maginn, E. J.; Ragauskas, A.; Dadmun, M.; Zawodzinski, T. A.; Baker, G. A.; Tuckerman, M. E.; Savinell, R. F.; Sangoro, J. R. Deep Eutectic Solvents: A Review of Fundamentals and Applications. Chemical Reviews 2021, 121 (3), 1232-1285

5. Ke, X. Y.; Prahl, J. M.; Alexander, J. I. D.; Wainright, J. S.; Zawodzinski, T. A.; Savinell, R. F. Rechargeable redox flow batteries: flow fields, stacks and design considerations. Chemical Society Reviews 2018, 47 (23), 8721-8743

6. Smith, E. L.; Abbott, A. P.; Ryder, K. S., Deep Eutectic Solvents (DESs) and Their Applications. Chemical Reviews 2014, 114 (21), 11060-11082.

7. Heuer, H. W.; Wehrmann, R.; Kirchmeyer, S. Electrochromic window based on conducting poly(3,4-ethylenedioxythiophene):poly(styrene sulfonate). Advanced Functional Materials 2002, 12 (2), 89-94

8. Pal, R. K.; Kundu, S. C.; Yadavalli, V. K. Biosensing using photolithographically micropatterned electrodes of PEDOT:PSS on ITO substrates. Sensors and Actuators B-Chemical 2017, 242, 140-147 DOI: 10.1016/j.snb.2016.11.049.

9. T. Nguyen and R. F. Savinell, Electrochem. Soc. Interface, 2010, 54-56

10. Wollan, E. O.; Shull, C. G. The diffraction of neutrons by crystalline powders. Physical review 1948, 73 (8), 830-841.

11. Shull, C. G.; Wollan, E. O. X-ray, electron, and neutron diffraction. Science 1948, 108 (2795), 69-75.

12. Sawyer, R. B.; Wollan, E. O.; Peterson, K. C.; Bernstein, S. Application of a bent crystal neutron spectrometer to measurements of resonance absorption. Physical review 1946, 70 (9-10), 791-791.

13. Shull, C. G.; Wollan, E. O. The diffraction of neutrons by crystalline powders. Physical review 1947, 72 (2), 168-168.

14. W. H. and W. L. Bragg, crystalline state (the Macmillan company, New York, 1933},p. 189

15. Davidson, W. L.; Morton, G. A.; Shull, C. G.; Wollan, E. O. Diffraction of neutrons by hydrogen and deuterium containing crystals. Physical review 1947, 72 (2), 168-169.

16. Etampawala, T.; Ratnaweera, D.; Morgan, B.; Diallo, S.; Mamontov, E.; Dadmun, M. Monitoring the dynamics of miscible P3HT:PCBM blends: A quasi elastic neutron scattering study of organic photovoltaic active layers. Polymer 2015, 61, 155-162

17. Smith M.D., Pingali S.V., Elkins J.G., Bolmatov D., Standaert R.F., Nickels J.D., Urban V.S., Katsaras J., Davison B., Smith J.C., Petridis L., "Solvent-induced membrane stress in biofuel production: Molecular insights from Small-Angle Scattering and All-Atom Molecular Dynamics Simulations", Green Chemistry, 22, 8278 (2020).

18. Imae, T., Kanaya T., Furusaka M., Torikai N.(eds), Neutrons in Soft Matter, John Wiley and Sons, (2011)

19. Carpenter, J. M.; Agamalian, M.; Littrell, K. C.; Thiyagarajan, P.; Rehm, C. Time-of-flight implementation of an ultrasmall-angle neutron scattering instrument. Journal of Applied Crystallography 2003, 36, 763-768

20. Wignall, G. D.; Bates, F. S. Absolute calibration of small-angle neutron-scattering data. Journal of Applied Crystallography 1987, 20, 28-40.

21. Wignall, G. D.; Littrell, K. C.; Heller, W. T.; Melnichenko, Y. B.; Bailey, K. M.; Lynn, G. W.; Myles, D. A.; Urban, V. S.; Buchanan, M. V.; Selby, D. L.; Butler, P. D. The 40 m general purpose small-angle neutron scattering instrument at Oak Ridge National Laboratory. Journal of Applied Crystallography 2012, 45, 990-998

22. Van Every, E.; Deyhim, A.; Kulesza, J. New Very Small-angle Neutron Scattering (VSANS) Instrument, J. Phys.: Conf. Ser. , 2016 746 012025

23. Barker, J. G.; Glinka, C. J.; Moyer, J. J.; Kim, M. H.; Drews, A. R.; Agamalian, M. Design and performance of a thermal-neutron double-crystal diffractometer for USANS at NIST. Journal of Applied Crystallography 2005, 38, 1004-1011

24. Neuefeind, J.; Feygenson, M.; Carruth, J.; Hoffmann, R.; Chipley, K. K., The Nanoscale Ordered materials Diffractometer NOMAD at the Spallation Neutron Source SNS. Nuclear Instruments & Methods in Physics Research Section B-Beam Interactions with Materials and Atoms 2012, 287, 68-75.

25. Ankner J.F., Tao X., Halbert C.E., Browning J.F., Kilbey II S.M., Swader O.A., admun M.S., Kharlampieva E., Sukhishvili S.A., "The SNS Liquids Reflectometer", Neutron News, 19, 3, 14 (2008).

26. Mamontov E., Zamponi M., Hammons S., Keener W.S., Hagen M., Herwig K.W., "BASIS: a new backscattering spectrometer at the SNS", Neutron News, 19, 3, 22-24 (2008).

27. Meyer, A.; Dimeo R. M.; Gehring P. M.; Neumann D. A., The high-flux backscattering spectrometer at the NIST Center for Neutron Research, Review of Scientific Instruments, 2003, 74, 2759-2777

28. Gehring, P.M. and Neumann, D.A., Physica B: Condensed Matter 241-243, 64–70 (1997)

29. Mezei, F. Neutron spin echo: A new concept in polarized thermal neutron techniques. Z. Physik 255, 146–160 (1972)

30. Richter D., Monkenbusch M., Arbe A., Colmenero J. (2005) Neutron Spin Echo in Polymer Systems. In: Neutron Spin Echo in Polymer Systems. Advances in Polymer Science, vol 174. Springer, Berlin, Heidelberg.

31. McClintock, R. O. The Design, Test, and Use of the Brookhaven National Laboratory (BNL) Reactor Bypass Filter Facility. United States: N. P., 1966.

32. Carpenter, J. M.; Blewitt, T. H.; Price, D. L.; Werner, S. A. Pulsed Spallation Neutron Sources. Physics Today 1979, 32 (12), 42-49

33. Carpenter, J. M.; Price, D. L. Intense Pulsed Neutron Source for Argonne National Laboratory. IEEE Transactions on Nuclear Science 1975, NS22 (3), 1768-1771.

34. Mason, T. E.; Abernathy, D.; Anderson, I.; Ankner, J.; Egami, T.; Ehlers, G.; Ekkebus, A.; Granroth, G.; Hagen, M.; Herwig, K.; Hodges, J.; Hoffmann, C.; Horak, C.; Horton, L.; Klose, F.; Larese, J.; Mesecar, A.; Myles, D.; Neuefeind, J.; Ohl, M.; Tulk, C.; Wang, X. L.; Zhao, J. The Spallation Neutron Source in Oak Ridge: A powerful tool for materials research. Physica B-Condensed Matter 2006, 385-86, 955-960

35. Heller W.T., Cuneo M.J., Debeer-Schmitt L.M., Do C., He L., Heroux L., Littrell K.C., Pingali S.V., Qian S., Stanley C.B., Urban V.S., Wu B., Bras W., "The suite of small-angle neutron scattering instruments at Oak Ridge National Laboratory", Journal of Applied Crystallography, 51, 2, 1-7 (2018).

36. Bonse, U., Hart M., Tailless x-ray single-crystal reflection curves obtained by multiple reflection Appl. Phys. Lett. 7, 238 (1965)

37. Parratt, L. G., Surface Studies of Solids by Total Reflection of X-Rays, Physical Review. American Physical Society (APS). 95 (2): 359–369 (1954)

38. Martin, H. J.; White, B. T.; Scanlon, C. J.; Saito, T.; Dadmun, M. D. Tunable synthetic control of soft polymeric nanoparticle morphology. Soft Matter 2017, 13 (46), 8849-8857

39. Yin X., Hewitt D.R., Preston A.N., Heroux L., Agamalian M., Quah S.P., Zheng B., Smith A.J., Laughlin S.T., Grubbs R.B., Bhatia S.R., "Hierarchical assembly in PLA-PEO-PLA hydrogels with crystalline domains and effect of block stereochemistry", Colloids and Surfaces B: Biointerfaces, 180, 102-109 (2019).

40. Murphy, R. J.; Weigandt, K. M.; Uhrig, D.; Alsayed, A.; Badre, C.; Hough, L.; Muthukumar, M. Scattering Studies on Poly(3,4-ethylenedioxythiophene)-Polystyrenesulfonate in the Presence of Ionic Liquids. Macromolecules 2015, 48 (24), 8989-8997

41. del Rio JG, Hayes DG, Urban VS. Partitioning behavior of an acid-cleavable, 1,3-dioxolane alkyl ethoxylate, surfactant in single and binary surfactant mixtures for 2-and 3-phase microemulsion systems according to ethoxylate head group size. Journal of Colloid and Interface Science. 2010;352(2):424-435.

42. Morgan, B.; Rinehart, S. J.; Dadmun, M. D. Monitoring the Effects of Illumination on the Structure of Conjugated Polymer Gels Using Neutron Scattering. Jove-Journal of Visualized Experiments 2017, (130).

43. Feigin, L., Svergun D., Structure Analysis by Small-Angle X-Ray and Neutron Scattering, Plenum, New York, (1987)

44. Kim, G. H.; Shao, L.; Zhang, K.; Pipe, K. P. Engineered doping of organic semiconductors for enhanced thermoelectric efficiency. Nature Materials 2013, 12 (8), 719-723

45. Dimitriev, O. P.; Grinko, D. A.; Noskov, Y. V.; Ogurtsov, N. A.; Pud, A. A. PEDOT:PSS films-Effect of organic solvent additives and annealing on the film conductivity. Synthetic Metals 2009, 159 (21-22), 2237-2239

46. Carpenter, J. M.; Agamalian, M.; Iop, Aiming for the theoretical limit of sensitivity of Bonse-Hart USANS instruments. In International Conference on Neutron Scattering 2009, 2010; Vol. 251.

47. Agamalian, M.; Heroux, L.; Littrell, K. C.; Carpenter, J. M.; Iop, Progress on The Time-of-Flight Ultra Small-angle Neutron Scattering Instrument at SNS. In 22nd Meeting of the International Collaboration on Advanced Neutron Sources, 2018; Vol. 1021.

48. Agamalian, M.; Christen, D. K.; Drews, A. R.; Glinka, C. J.; Matsuoka, H.; Wignall, G. D. Surface-induced parasitic scattering in Bonse-Hart double-crystal diffractometers. Journal of Applied Crystallography 1998, 31, 235-240

49. Agamalian, M.; Iolin, E.; Rusevich, L.; Glinka, C. J.; Wignall, G. D. Back-face Bragg diffraction from a perfect and ultralightly deformed thick crystal. Physical Review Letters 1998, 81 (3), 602-605

50. Agamalian, M.; Wignall, G. D.; Triolo, R. Optimization of a Bonse-Hart Ultra-Small-Angle Neutron Scattering Facility by Elimination of the Rocking-Curve Wings. Journal of Applied Crystallography 1997, 30, 345-352

51. Shen, B. H.; Armstrong, B. L.; Doucet, M.; Heroux, L.; Browning, J. F.; Agamalian, M.; Tenhaeff, W. E.; Veith, G. M. Shear Thickening Electrolyte Built from Sterically Stabilized Colloidal Particles. ACS Applied Materials & Interfaces 2018, 10 (11), 9424-9434.

52. Burdette-Trofimov M.K., Armstrong B.L., Murphy R.P., Heroux L., Doucet M., Rogers A.M., Veith G.M., "Probing Clustering Dynamics Between Silicon and PAA or LiPAA Slurries under Processing Conditions", ACS Applied Polymer Materials, 3, 5, 2447–2460 (2021).

53. V. Nigro, R. Angelini, S. King, S. Franco, E. Buratti, F. Bomboi, N. Mahmoudi, F. Corvasce, R., Apparatus for simultaneous dynamic light scattering–small-angle neutron scattering investigations of dynamics and structure in soft matter, Rev. Sci. Instrum. 92, 023907 (2021)

54. Zhang, Y.; Poe, D.; Heroux, L.; Squire, H.; Doherty, B. W.; Long, Z. R.; Dadmun, M.; Gurkan, B.; Tuckerman, M. E.; Maginn, E. J., Liquid Structure and Transport Properties of the Deep Eutectic Solvent Ethaline, Published as part of The Journal of Physical Chemistry virtual special issue "Deep Eutectic Solvents". Journal of Physical Chemistry B 2020, 124 (25), 5251-5264.

55. Turner, A. H.; Holbrey, J. D., Investigation of glycerol hydrogen-bonding networks in choline chloride/glycerol eutectic-forming liquids using neutron diffraction. Physical Chemistry Chemical Physics 2019, 21 (39), 21782-21789.

56. Russina, O. & Triolo, A. Chapter 4 - Ionic liquids and neutron scattering. In Fernandez-Alonso, F. & Price, D. L. (eds) Neutron Scattering - Applications in Biology, Chemistry, and Materials Science, vol. 49 of Experimental Methods in the Physical Sciences, 213–278 (Academic Press, 2017).

57. Faraone, A.; Wagel, D. V.; Baker, G. A.; Novak, E. C.; Ohl, M.; Reuter, D.; Lunkenheimer, P.; Loidl, A.; Mamontov, E., Glycerol Hydrogen-Bonding Network Dominates Structure and Collective Dynamics in a Deep Eutectic Solvent. Journal of Physical Chemistry B 2018, 122 (3), 1261-1267.

58. Wagle, D. V.; Baker, G. A.; Mamontov, E., Differential Microscopic Mobility of Components within a Deep Eutectic Solvent. Journal of Physical Chemistry Letters 2015, 6 (15), 2924-2928.

59. Torikai N, Yamada NL, Noro A, *et al*. Neutron reflectometry on interfacial structures of the thin films of polymer and lipid. Polymer Journal. 2007;39(12):1238-1246.

60. Makita Y, Uemura S, Miyanari N, *et al*. Electrochemical Investigation of Dynamic Solution Structures of Bicontinuous Microemulsion at Solid Interfaces. Chemistry Letters. 2010;39(11):1152-1154.

61. Vargas-Ruiz S, Soltwedel O, Micciulla S, *et al*. Sugar Surfactant Based Microemulsions at Solid Surfaces: Influence of the Oil Type and Surface Polarity. Langmuir. 2016;32(45):11928-11938.

62. Heuer, H. W.; Wehrmann, R.; Kirchmeyer, S. Electrochromic window based on conducting poly (3,4-ethylenedioxythiophene)poly(styrene sulfonate). Advanced Functional Materials 2002, 12 (2), 89-94

63. Daoud, W. A.; Xin, J. H.; Szeto, Y. S. Polyethylenedioxythiophene coatings for humidity, temperature and strain sensing polyamide fibers. Sensors and Actuators B-Chemical 2005, 109 (2), 329-333

64. Rinehart, S.; Smart, T.; Dougherty, J.; Dadmun, M. D. Impact of Substrate Rigidity on the Structure of Multilayer Nanoscale ITO Films: Implications for Flexible Electronic Devices. ACS Applied Nano Materials 2020, 3 (3), 2383-2392

65. Zabihi, F.; Xie, Y.; Gao, S.; Eslamian, M. Morphology, conductivity, and wetting characteristics of PEDOT:PSS thin films deposited by spin and spray coating. Applied Surface Science 2015, 338, 163-177

66. Xia, Y. J.; Sun, K.; Ouyang, J. Y. Solution-Processed Metallic Conducting Polymer Films as Transparent Electrode of Optoelectronic Devices. Advanced Materials 2012, 24 (18), 2436-2440.

67. Ouyang, J.; Xu, Q. F.; Chu, C. W.; Yang, Y.; Li, G.; Shinar, J. On the mechanism of conductivity enhancement in poly (3,4-ethylenedioxythiophene): poly(styrene sulfonate) film through solvent treatment. Polymer 2004, 45 (25), 8443-8450

68. Kim, J. Y.; Jung, J. H.; Lee, D. E.; Joo, J. Enhancement of electrical conductivity of poly(3,4-ethylenedioxythiophene)/poly(4-styrenesulfonate) by a change of solvents. Synthetic Metals 2002, 126 (2-3), 311-316

69. Ashizawa, S.; Horikawa, R.; Okuzaki, H. Effects of solvent on carrier transport in poly(3,4-ethylenedioxythiophene)/poly(4-styrenesulfonate). Synthetic Metals 2005, 153 (1-3), 5-8

70. Lawrence MJ, Rees GD. Microemulsion-based media as novel drug delivery systems. Advanced Drug Delivery Reviews. 2000;45(1):89-121.

71. Kalaitzaki A, Emo M, Stebe MJ, Xenakis A, Papadimitriou V. Biocompatible nanodispersions as delivery systems of food additives: A structural study. Food Research International. 2013;54(2):1448-1454.

72. Peng J, Cantillo NM, Nelms KM, *et al.* Electron Transfer in Microemulsion-Based Electrolytes. ACS Applied Materials & Interfaces. 2020;12(36):40213-40219.

73. Kunitake M, Kuraya E, Kato D, Niwa O, Nishimi T. Electrochemistry in bicontinuous microemulsions based on control of dynamic solution structures on electrode surfaces. Current Opinion in Colloid & Interface Science. 2016;25:13-26.

74. Torrealba VA, Hoteit H, Johns RT. Description of Micellar Radii for Phase Behavior and Viscosity Modeling of Aqueous Surfactant Solutions and Microemulsions. Langmuir. 2018;34(50):15327-15334.

75. Niedermeyer, H.; Hallett, J. P.; Villar-Garcia, I. J.; Hunt, P. A.; Welton, T., Mixtures of ionic liquids. Chemical Society Reviews 2012, 41 (23), 7780-7802.

76. Abbott, A. P.; Capper, G.; Davies, D. L.; Munro, H. L.; Rasheed, R. K.; Tambyrajah, V., Preparation of novel, moisture-stable, Lewis-acidic ionic liquids containing quaternary ammonium salts with functional side chains. Chemical Communications 2001, (19), 2010-2011.

77. Abbott, A. P.; Boothby, D.; Capper, G.; Davies, D. L.; Rasheed, R. K., Deep eutectic solvents formed between choline chloride and carboxylic acids: Versatile alternatives to ionic liquids. Journal of the American Chemical Society 2004, 126 (29), 9142-9147.

78. Gurkan B., Squire H., Pentzer E., Metal-Free Deep Eutectic Solvents: Preparation, Physical Properties, and Significance, The Journal of Physical Chemistry Letters 2019 10 (24), 7956-7964

79. Dean W., Klein J., Gurkan B., Do Deep Eutectic Solvents Behave Like Ionic Liquid Electrolytes? A Perspective from the Electrode-Electrolyte Interface2 Journal of The Electrochemical Society, 2021.

80. Hammond, O. S.; Bowron, D. T.; Jackson, A. J.; Arnold, T.; Sanchez-Fernandez, A.; Tsapatsaris, N.; Sakai, V. G.; Edler, K. J., Resilience of Malic Acid Natural Deep Eutectic Solvent Nanostructure to Solidification and Hydration

81. Karimi, M.; Eshraghi, M. J., One-pot and green synthesis of Mn3O4 nanoparticles using an all-in-one system (solvent, reactant and template) based on ethaline deep eutectic solvent. Journal of Alloys and Compounds 2017, 696, 171-176.

Chapter II Controlling the Morphology of PEDOT:PSS Blend Films with Pre-Deposition Solution Composition and Deposition Technique

Abstract

Understanding the relationships between morphology, fabrication processes, and thermoelectric performance in conducting polymers is essential to the development of high- efficiency organic thermoelectrics as an alternative to commonly used rare metals. Altering the film fabrication process of Poly(3,4-ethylenedioxythiophene): poly(styrene sulfonate) (PEDOT:PSS) with the addition of high boiling solvents to the precast solution improves the electrical conductivity and significantly increases its Seebeck value. Neutron scattering monitors the changes in the atomic, nanoscale and mesoscale morphology of PEDOT:PSS thin films with the addition of dimethyl sulfoxide (DMSO) to the aqueous solution prior to film formation and with varying fabrication procedures. The neutron scattering results show a decrease in the deuterated PSS (dPSS) domain size along with systematic variations in PEDOT fibril assemblies in the final blend film with the addition of DMSO to the pre-deposition solution. These structural modifications indicate that the increase in conductivity of PEDOT:PSS blends with DMSO is a result of the DMSO disrupting the solvated PEDOT assemblies and forming smaller PSS domains in the pre-deposition solution, allowing smoother film formation. These improvements are seen significantly with the addition of just 1% DMSO but continue to improve with the addition of up to 5% DMSO to the PEDOT:PSS polymer blend. The fact that the variations in the measured morphology are independent of whether the films were deposited by spin or ultra-sonic spray casting methods emphasizes the crucial importance of the structure of the blend in the pre-deposition solution in determining the final thin film blend morphology.

Introduction

Conducting polymers are an important class of materials, where their use in energy harvesting applications aid in the development of technologies to improve sustainability. Thermoelectric materials transform a temperature gradient to an electric current, or inversely an electric potential to a change in temperature. Thermoelectrics have been useful in commercially available energy technologies; for instance, they are commonly found in photovoltaics for solar-energy generation and light-emitting diodes.[1,2,3]1 The efficiency of a material in converting a thermal gradient to an electric potential is given by the dimensionless figure of merit ZT, which is calculated by $ZT = \frac{S^2\sigma T}{\kappa}$. In this equation, S is the Seebeck coefficient of the material, σ its electric conductivity, T is the temperature, and κ is its thermal conductivity. Most common thermoelectrics with high ZT's are inorganic materials consisting of rare metals. However, these inorganic materials are brittle, and expensive to obtain and fabricate thermoelectrics from. On the other hand, thermoelectric polymers offer a flexible material that can conformally coat an object and offers ease of processing that can be scaled for commercial manufacturing of high-quality films.[4] Consequently, these organic thermoelectrics provide an inexpensive and viable alternative to the brittle rare metals that are currently more common in thermoelectric applications. However, the performance of organic thermoelectrics lags that of inorganic thermoelectrics, and a more thorough understanding of how the thermoelectric performance of these promising materials can be tuned is needed. For instance, previous studies have shown that alteration of the film formation conditions can result in a dramatic improvement in thermoelectric performance. Thus, understanding the relationships between fabrication processes, morphology development during fabrication, and thermoelectric performance in conducting polymer constructs is needed to move this field towards the rational development of organic thermoelectrics with optimal performance.

Poly(3,4-ethylenedioxythiophene):poly(styrene sulfonate) (PEDOT: PSS) is a promising and commonly studied conjugated polymer blend that currently has the highest reported figure of merit ZT of any organic material at room temperature.[5] Moreover, previous studies have shown that altering the film fabrication process such as including the addition of high boiling solvents to its precast solution or immersion of the cast film in ethylene glycol dramatically impacts its electrical conductivity and Seebeck value.[5-1319] More precisely, the addition of dimethyl sulfoxide (DMSO) to the pre-deposition PSS:PEDOT solution has been shown to increase the electrical conductivity and lower the Seebeck coefficient of a film that is formed from that solution.[6] Some of these studies have shown an increase in electrical conductivity by as much as a factor of 1000.[76,7] For instance, Dimitriev , *et al*, reported that the conductivity increased by a factor of 4 with the addition of just 1% DMSO and an order of magnitude increase with the addition of 5% DMSO to the pre-deposition solution.[6] Further studies using small and ultra-small-angle neutron scattering showed that adding DMSO to the pre-deposition solution altered the morphology of spray-coated films.[7,8] In these studies, it was observed that the local fibril-like PEDOT domains decrease in size and become more uniformly shaped with addition of DMSO. This improved uniformity of PEDOT fibrils in the larger PSS domain resulted in enhanced conductivity due to better mesoscale ordering, with increases in conductivity by a factor of 800.[7]

Additional studies, using techniques such as atomic force microscopy (AFM), scanning electron microscopy (SEM), and Raman Spectroscopy have provided insight into how altering the film fabrication technique improves the conductivity of the thermoelectric film. Varying the film coating technique alters the smoothness and wetting, which are monitored by imaging the film surface.[4,8,9] Particularly, the thickness, wetting, and roughness of the deposited films varied with the surface tension, contact angle, viscosity, and deposited drop sizes in spray-coated films, which varied with pre-deposition concentrations of DMSO.[4,8,11] Zabihi, *et al.*, observed that the spin coating created a stratified structure with an upper PSS-rich layer on a PEDOT-rich lower layer. The structure and surface roughness of the upper PSS-rich layer varies with substrate temperature and annealing temperature, which impacts film conductivity.[9] Smoother surfaces, especially surfaces which displayed fewer large domains as observed in AFM and SEM, were the most conductive. [9] These studies also verify that the PEDOT: PSS films are smoother at the meso-scale length scale and exhibit higher conductivity when spin-coated than when spray-coated. These reports also showed that spin cast surfaces tend to be smoother with the addition of DMSO to the pre-deposition solution than without, leading to further increases in conductivity.[9] Additionally, Ouyang *et al*, observed that the increase in conductivity occurs only when additives are included in the liquid pre-deposition solution and are then annealed.[4,11]

To date, few studies have been performed to clearly identify the morphology of PEDOT:PSS blend films and correlate its structure to its performance as an organic thermoelectric. The studies that have been published use various compositions of

PEDOT:PSS solutions and additives with different treatments and coating methods.[5-9] The existing knowledge of morphological changes is often limited to the length scale of the techniques used, including AFM, Raman Spectroscopy or neutron scattering.[6,8,9,11] Of these investigations, only a couple have addressed the changes in morphology over a broad range of length scales.[6,8] Additional studies suggest that the morphology of the PEDOT:PSS system undergoes observable changes across a broad range of length scales, from atomic- to nano- to micron length scales, with incremental variation in pre-deposition solution composition.[9-11] Therefore, analysis of the structure over the various length scales can offer crucial insight into how the morphology of the blend and ordering of its components varies with film formation conditions. In this study, we focus on the variation of the blend film structure with deposition technique (spin coating to spray coating) as well as the loading of DMSO in the pre-deposition solvent. Using small-angle and ultra-small-angle neutron scattering provides insight into the morphological changes in PEDOT:dPSS films on length scales that range from 10's of angstroms up to 100's of microns.[14]

Specifically, we have explored how the morphology of the Poly(3,4-ethylenedioxythiophene): deuterated poly(styrene sulfonate) (PEDOT:dPSS) polymer blend varies when cast by spin coating or spray coating, coupled to the impact of the presence of DMSO in the pre-deposition solution on the structure of the deposited film. We monitored the change in PEDOT:dPSS structure when 1% wt., 3% wt. and 5% wt. DMSO was added to the pre-deposition solution and compared the structure of these as-cast films using small-angle neutron scattering. These results provide insight into the relative importance of deposition technique and predeposition solution structure on final film morphology and provide insight that can be used to optimize the performance of PEDOT:PSS blend films in functional applications.

Experimental Methods

Synthesis

PEDOT:dPSS in aqueous solutions were created by the polymerization of 3,4-ethylenedioxythiophene (EDOT) in a deuterated poly(styrene sulfonate) (dPSS) aqueous solution following the BAYTRON P synthesis as described in the literature.[16-19] In this polymerization, EDOT monomers from TCI America were oxidatively polymerized in an aqueous dPSS (Mw 429 kDa, PDI 1.15, Polymer Source Inc. Canada) solution using charge balancing counter ions $Na_2S_2O_8$ (Sigma-Aldrich, USA) and $Fe_2(SO_4)_3 \cdot 5H_2O$ (Acros-Organics, USA). This bulk solution was separated into smaller volumes to create a series of solutions with a range of DMSO loadings. To remove large aggregates that may have formed, the blend solutions were then filtered 3 times through 5 μm syringe filters.

Film Formation

The solutions were deposited to form films by spin coating and spray coating onto Silicon crystal wafer substrates that have been etched with piranha (3:1 sulfuric acid and hydrogen peroxide) and oxidized under ultra-violet light. All cast films were annealed at 413K for 20 minutes to remove any excess water and dopant. Films were roughly measured to be 20 nm – 40 nm thick using a micrometer.

Spin-coated films were fabricated using 1ml of solution spun at 1000 rpm for 90 seconds as illustrated in Figure II.1. Speed and duration of deposition were chosen based on common parameters used in other studies as well as to optimize consistency of the

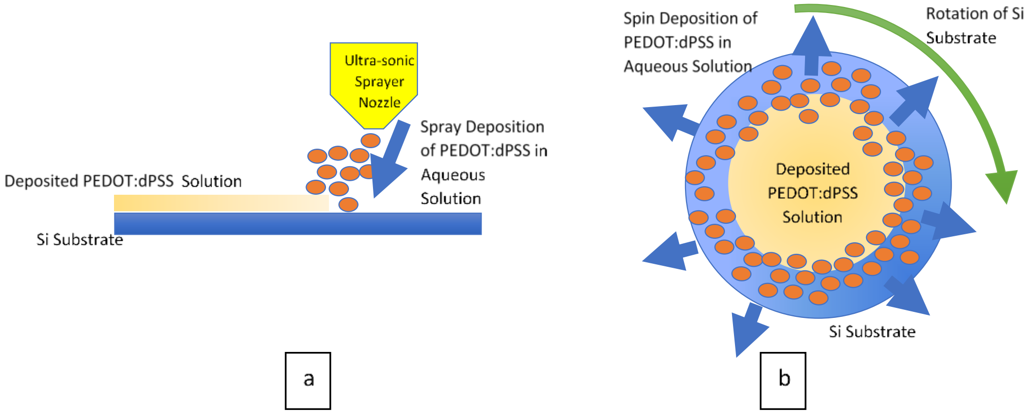

Figure II.1 – Illustration of deposition processes that occur during the formation of PEDOT:dPSS films on Si Substrates. Spray coating with use of custom built ultra-sonic nozzle (a) and spin coating (b).

coating and maintain a conductive surface. The conductivity in all films was confirmed using an ohmmeter.

Spray-coated films were deposited using a custom-built jet-nozzle sprayer that transitions across the substrate as illustrated in Figure II.1. Nozzle speed was adjusted to a minimum spray speed of around 0.05 ml/sec to achieve a smooth consistent coating that was also conductive. 30 spray passes were made to achieve well distributed visually consistent films.

Neutron Scattering

Substrates with deposited films were physically divided into smaller pieces of 1.2cm squares post-deposition to fit into sample containers on all neutron scattering instruments.[13] Si wafers with polymer film were stacked to increase scattering statistics, giving a calculated total film thickness in the neutron beam of 650 μm. All neutron measurements were taken at room temperature (~298K) and were normalized to transmission as well as for thickness of samples.[20] Sample container and Si wafer background scattering were subtracted from sample scattering to obtain the scattering of the PEDOT:dPSS films.

To monitor the structure of the PEDOT:dPSS blend films over a broad range of length scales, four neutron scattering instruments were used. At Oak Ridge National Laboratory (ORNL), these were the General Purpose Small-angle Neutron Scattering (GP-SANS) instrument at the High Flux Isotope Reactor with a neutron wavelength (λ) range of λ = 4.75Å, 6 Å, and 18Å; and the Ultra-Small-angle Neutron Scattering (USANS) instrument at the Spallation Neutron Source with distinct wavelengths of λ/n, where λ=3.6Å, and the harmonic peak n=1-5.[14,21] At the National Institute of Standards and Technology (NIST) Center for Neutron Research, the instruments used were the Very Small-Angle Neutron Scattering (VSANS) instrument, measured using two wavelengths of λ=5Å and λ=17Å; and the USANS instrument, measured using λ=5Å.[22] The combinations of these experiments provide data over a merged Q-range, from 1 x 10^{-6} A^{-1} up to 5 x 10^{-1} A^{-1}, which covers real space length scales that span microns to nanometers using USANS and nanometers to angstroms using the SANS/VSANS instruments and is defined by the scattering vector, Q, in reciprocal space according to Bragg's Law, $Q = \frac{4\pi \sin(\theta)}{\lambda}$, where λ is the wavelength of the neutrons, and θ is the scattering angle.

Reduction of the raw data from ORNL was performed using Mantid, while reduction of the raw data from NIST was performed using IGOR pro 8.[23,24] All data were combined and USANS point-space data was scaled to the normalized SANS data.[25] The VSANS data overlays the GP-SANS data and was therefore omitted from the final fits but was used to properly scale USANS data. Fitting and analysis were performed using SasView.[26] The data were fit to models that included a combination of the Debye-Anderson-Brumberger (DAB) model and the elliptical cylinder form factor.[27-30] The DAB model is captured in the first term of Equation 2.1 below, which was developed to model, and often used to characterize, the structure of two-phase systems.[7,27,28] The elliptical cylinder form factor is described as the second term in Equation 2.1 and has been applied to model and characterize the parallelepiped and cylindrical shaped structures in crystalline assemblies.[7,31,32] The DAB equation models the phase separated structure of the polymer blend, describing the morphology and size of the two polymer domains, parameterized as the correlation length, L, which is a measure of the average distance between dPSS domains. This structural feature dominates the scattering in the lowest Q region and is primarily measured using USANS. The elliptical cylinder models the average cross-sectional size and shape of the PEDOT fibrillar crystals that form in the phase separated polymer blend. The elliptical cylinder model quantifies the size of the cross section of the PEDOT crystals by providing the minor radius, r_{min}, and ratio of minor and major radii, ν, which is then used to calculate the major radius, $r_{maj} = {}^{\nu}/_{r_{min}}$, as well as the length of the cylinder, H. These length scales are primarily measured in the mid to high Q regions using SANS.

$$I(q) = A_1 \frac{L^3}{(1+(q\times L)^2)^2} + A_2 \frac{1}{V_{cyl}} \left(\frac{J(a)sin(b)}{ab} \right)^2 + background \qquad \text{Equation 2.1}$$

In Equation 2.1, L is the correlation length of the PSS:PEDOT film and the normalization factor, $A_1 = 8\pi\Phi(1-\Phi)\Delta\rho^2$. Here $\Delta\rho^2$ is the neutron scattering length density contrast of the two phases , and Φ represents the volume fraction of one phase. In the second term, A_2 is a pre-factor, V_{cyl} is the volume of the cylinder, and $J(a)$ is the Bessel function, where a and b are the radii defined as, $a=Qr'$, and $b = QH$, where H is the cylinder length and $r' = r_{min}\sqrt{2(1+\nu^2)}$.

Results

The neutron scattering curves of PEDOT:dPSS films that were formed from aqueous solutions containing varying amounts (0% wt., 1% wt., 3% wt., and 5% wt.) of DMSO were measured. The impact of deposition technique was also studied, where both spin-coated and spray-coated films were examined. These scattering curves are analyzed to determine the impact of these fabrication parameters on the nanoscale and mesoscale structure of the formed polymer blend thin films. These scattering curves and their fits to the DAB-elliptical cylinder model as described in Equation 2.1 are shown in Figures II.2 and II.3.

The correlation length (L) of the phase separated domains, as well as the minor (r_{min}), and major radius (r_{maj}) of the PEDOT fibrils are also presented in Table II.1 for the samples studied. The fitting of the data to the model was insensitive to the cylindrical length, H, which consistently attained large values (> 31000 Å).

Impact of addition of DMSO to pre-deposition solution on blend morphology

Inspection of these results shows that as DMSO is added to the solution, the sizes of the dPSS domains in the film dramatically decrease, as quantified by the change in the correlation length. The correlation length in the spin-coated films decreases from 5.2 μm to about 1.5 μm with the addition of 1% DMSO, a 70% decrease in size. Addition of more DMSO to the pre-deposition solution, 3% and 5% DMSO, further decreases the correlation length to 1.2 μm and 0.75 μm, respectively. These values correspond to a 78% and 85% decrease, respectively, in domain size when compared to the domains formed from pure aqueous solution. This decrease in correlation length establishes the formation of smaller dPSS domains in the spin-cast films with the addition of DMSO to the pre-deposition solution. This is consistent with the formation of smaller dPSS domains in solution with addition of DMSO to the pre-deposition solution, as illustrated in Figure II.4a. These results are also consistent with studies that showed smoother surfaces and increases in conductivity in PEDOT:PSS films with addition of DMSO to pre-deposition solutions.[5-7,9] While analysis of the lowest Q region provides information on the micron-scale domain structure (L), analysis of the higher Q regions (smaller length scales) provides

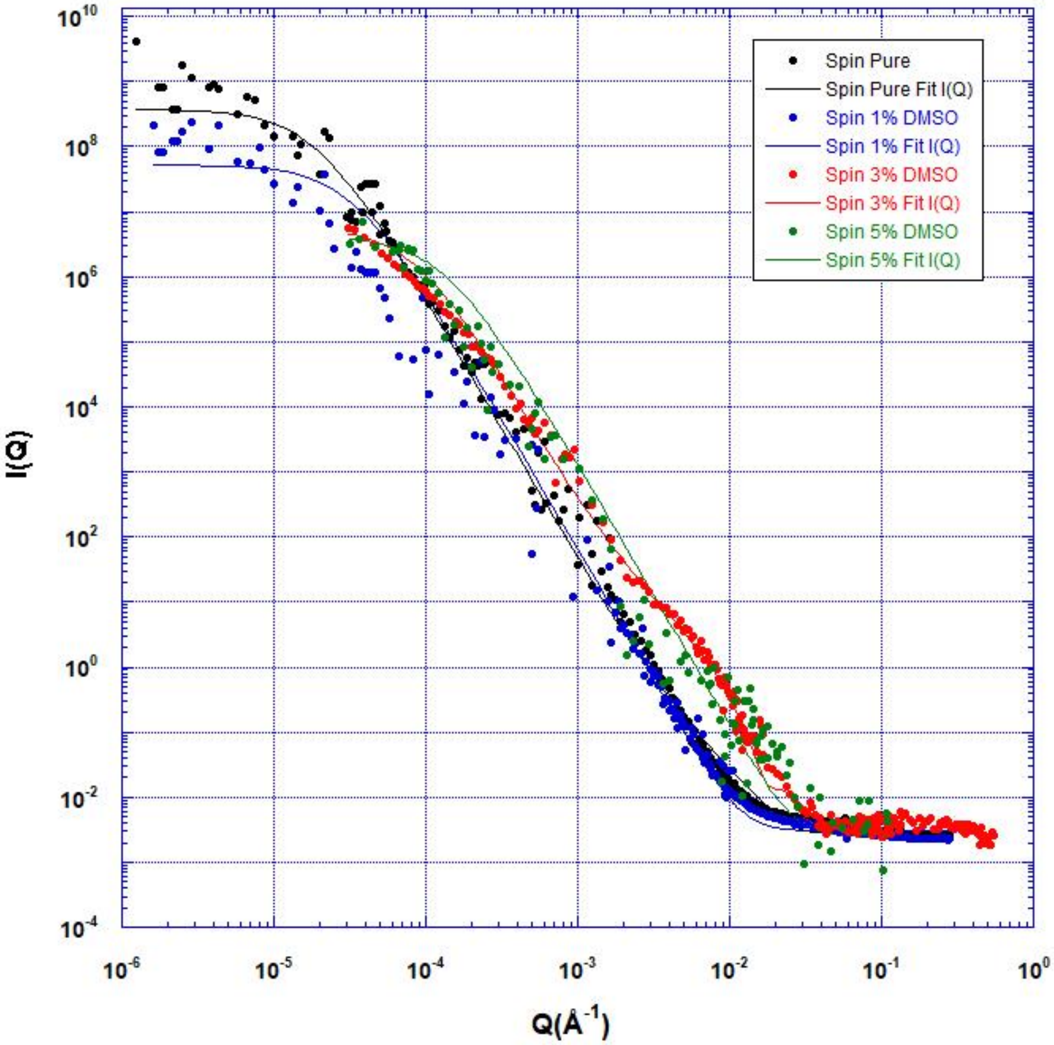

Figure II.2 – Plot of neutron scattering intensity (I(Q)) as a function of Q (Å^{-1}) for spin-coated films. SANS data for Pristine (black), 1%wt DMSO (blue), 3%wt DMSO (red), and 5%wt DMSO (green) solutions are dots and corresponding fits to Equation 1 are lines.

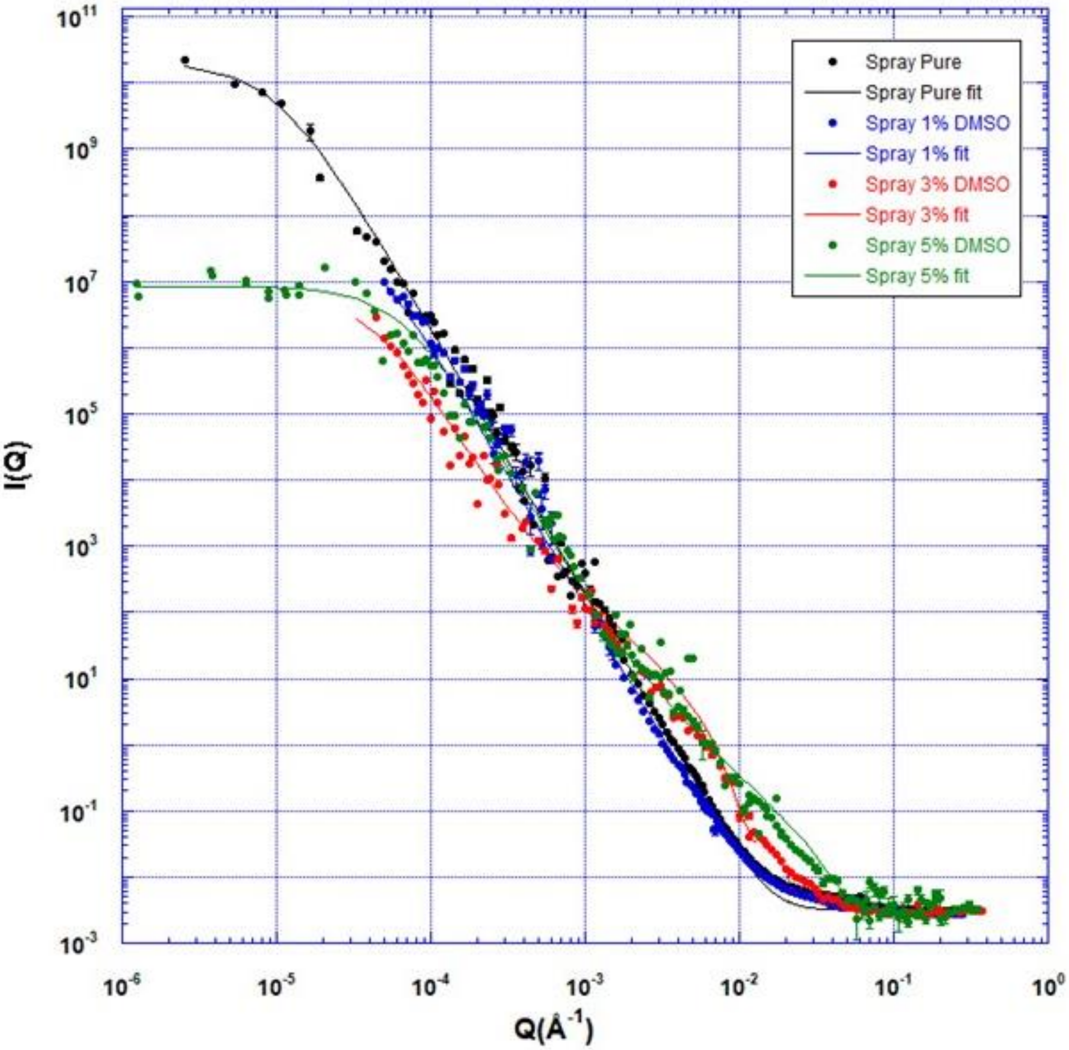

Figure II.3 – Plot of neutron scattering intensity (I(Q)) as a function of Q (Å^{-1}) for spray-coated films. SANS data for Pristine (black), 1%wt DMSO (blue), 3%wt DMSO (red), and 5%wt DMSO (green) solutions are dots and corresponding fits to Equation 1 are lines.

Table II.1- Correlation length (L), minor (r_{min}) and major (r_{maj}) radii in both spin and spray deposited films.

Film	Cor length, L (Å)	Minor Radius , r_{min} (Å)	Major Radius, r_{maj} (Å)
Spin Pristine	52776	90.00	540
Spin 1% DMSO	15000	0.04	12
Spin 3% DMSO	11700	200.00	10000
Spin 5% DMSO	7500	12.00	12
Spray Pristine	100000	9.00	810
Spray 1% DMSO	29000	4.46	3416
Spray 3% DMSO	22788	82.00	9102
Spray 5% DMSO	15000	50.00	750

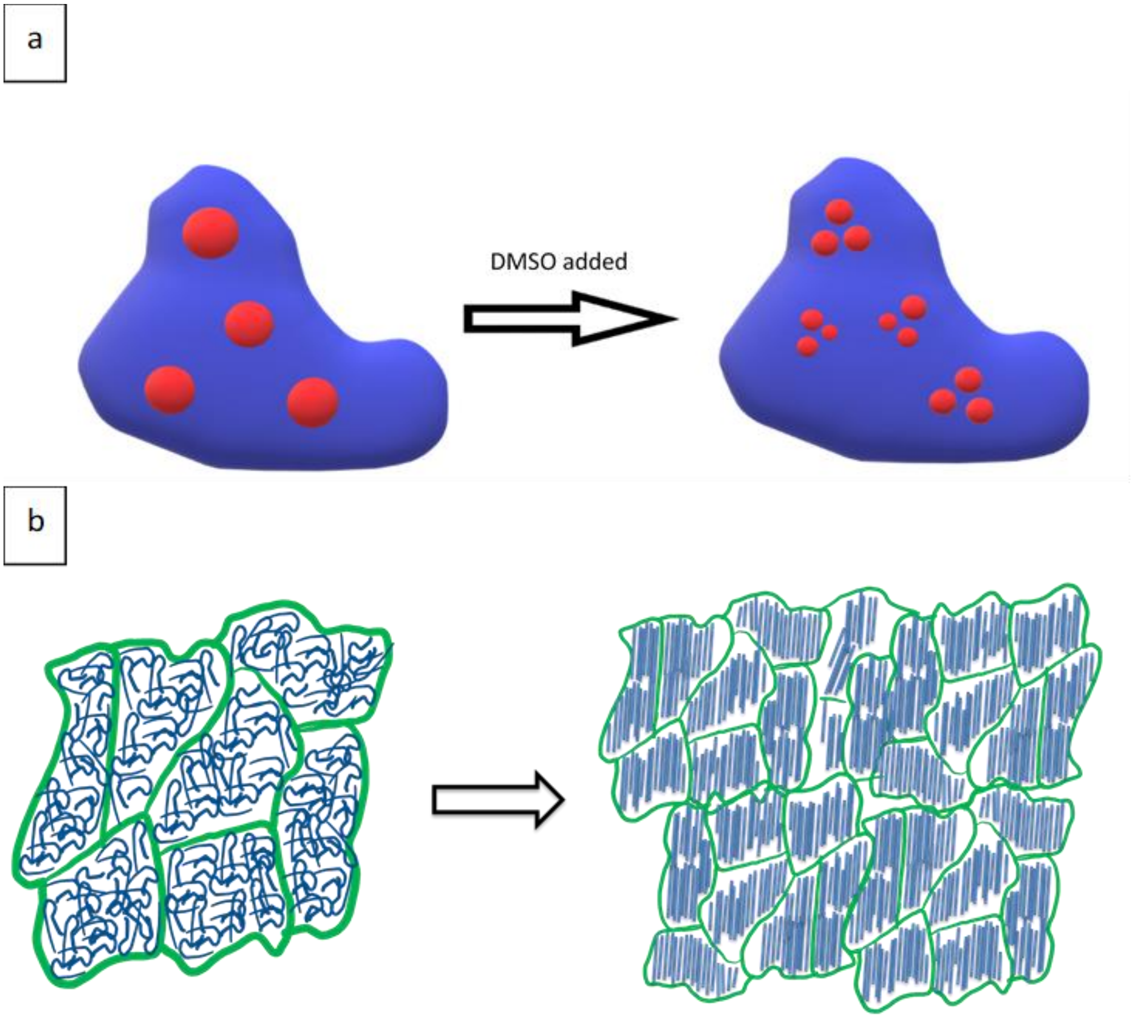

Figure II.4 – Sketch to illustrate change in domain (a) and fibril structure (b) with the addition of DMSO to the pre-deposition aqueous solution of PEDOT:dPSS. Large dPSS domains with randomly oriented fibrils break-up and shrink when DMSO is added and PEDOT fibrils become well-aligned.

information on the smaller PEDOT crystalline fibril structure (r_{min} & r_{maj}). This analysis shows that the PEDOT crystalline fibrils form domains with rectangular or elliptical cross-sections and the size of these fibrils in the film changes with the addition of DMSO to the pre-deposition solution and with the deposition technique. First, the addition of 1% DMSO to the pre-deposition solution decreases both the minor radius and the major radius of the fibril in the film, starting a fluctuation of size that is consistent with the disruption of the dPSS domains and a reorganization of the PEDOT crystals with the addition of DMSO, as illustrated in Figure II.4b. This trend reverses with the addition of more DMSO (3%). However, the major radius remains significantly greater than the minor radius, indicating that eccentric crystal domains are formed. The further addition of DMSO (5%) again reverses the size trends, where the elliptical cross section of the fibrils becomes more symmetric, shown by the decrease in r_{maj} and r_{min}. This variation indicates that the increase in DMSO to 5% drives the domains and PEDOT fibrils to eventually form a uniform elliptical shape.

This analysis indicates that the addition of DMSO initiates a reorganization of the fibrils that increases their packing and concurrently decreases the domain size. When PEDOT:dPSS is added to water, the hydrophilic dPSS domains encapsulate the hydrophobic PEDOT fibrils. Furthermore, when the water evaporates during film formation, the dPSS domains trap the PEDOT fibrils in place.[11] The observed changes in PEDOT radius and uniformity, combined with the decrease in correlation length, show a decrease in all structure sizes from the micron to the nanoscale by nearly an order of magnitude with the addition of DMSO. Structural changes of this magnitude are consistent with the size and smoothness changes as well as conductivity increases reported by other groups.[6,7,9]

Impact of Deposition Technique on Blend Structure

To monitor the impact of deposition procedure on the morphology and structure of the phase separated blend film, the neutron scattering curves of PEDOT:dPSS films formed by spray coating were also measured and analyzed as shown in Figure II.2. A qualitative inspection of these curves shows similar trends to those observed in the films formed by spin coating, most notably as the decrease in low Q scattering of the PEDOT:dPSS blends with the addition of DMSO. Quantitatively, the decrease in domain size (as monitored by the correlation length) is consistent with that of the spin-coated films. Spray-coated films show a 70% decrease in domain size relative to those formed from the aqueous solution (10 μm to 2.9 μm) with the addition of 1% DMSO, followed by further decreases in domain size with additional DMSO (a 77% size reduction with 3% DMSO and 85% size reduction with 5% DMSO). As with the spin-coated samples, the phase separated structure decreases systematically from that of the pure (0% DMSO) PEDOT:dPSS solutions. Given that the qualitative and quantitative changes in dPSS domain size in the film with addition of DMSO to the pre-deposition solution is similar for both deposition techniques, it appears that the morphological changes in the film are due to the structural changes of the blend in the pre-deposition solution with addition of DMSO and not a result of the mechanics of the film formation processes associated with the deposition technique.

Analysis of the neutron scattering curves at smaller length scales (higher Q value) also shows similar morphological changes of the samples fabricated by the two deposition techniques. The addition of DMSO to the pre-deposition solution also results in PEDOT fibrillar domains that fluctuate in size with DMSO loading for the samples fabricated by spray coating. In the spray-coated samples, the r_{min} initially decreases with added DMSO, followed by an increase in domain size at 3% DMSO and a slight decrease with 5% DMSO. The r_{maj} initially increases significantly with addition of 1% and 3% DMSO, then decreases as 5% DMSO is added to the pre-deposition solution, leading to a more symmetric cross-section of the PEDOT crystalline fibrils at this highest DMSO loading. These results, therefore, demonstrate the disruption of the PSS and PEDOT domains with DMSO addition to the pre-deposition solution is dominant in determining the structure of the PEDOT:dPSS phase separated polymer blend film. This is accompanied by a reorganization of the PEDOT fibrils with addition of DMSO. As the amount of DMSO is increased in the pre-deposition solution, the dPSS domains continue to break up into smaller domains, while the PEDOT fibrils become more uniformly aligned. This observation is consistent with an increase in packing density of the PEDOT fibrils within the smaller dPSS domains. Therefore, it appears that similar morphological formation processes occur during film development in the spray-coated films as with the spin-coated films.

Discussion

Figure II.5 plots the domain size of the spin and spray-coated samples as a function of amount of DMSO in the pre-deposition solution. Careful inspection shows that not only are the trends of the two samples similar, but quantitatively follow each other. This

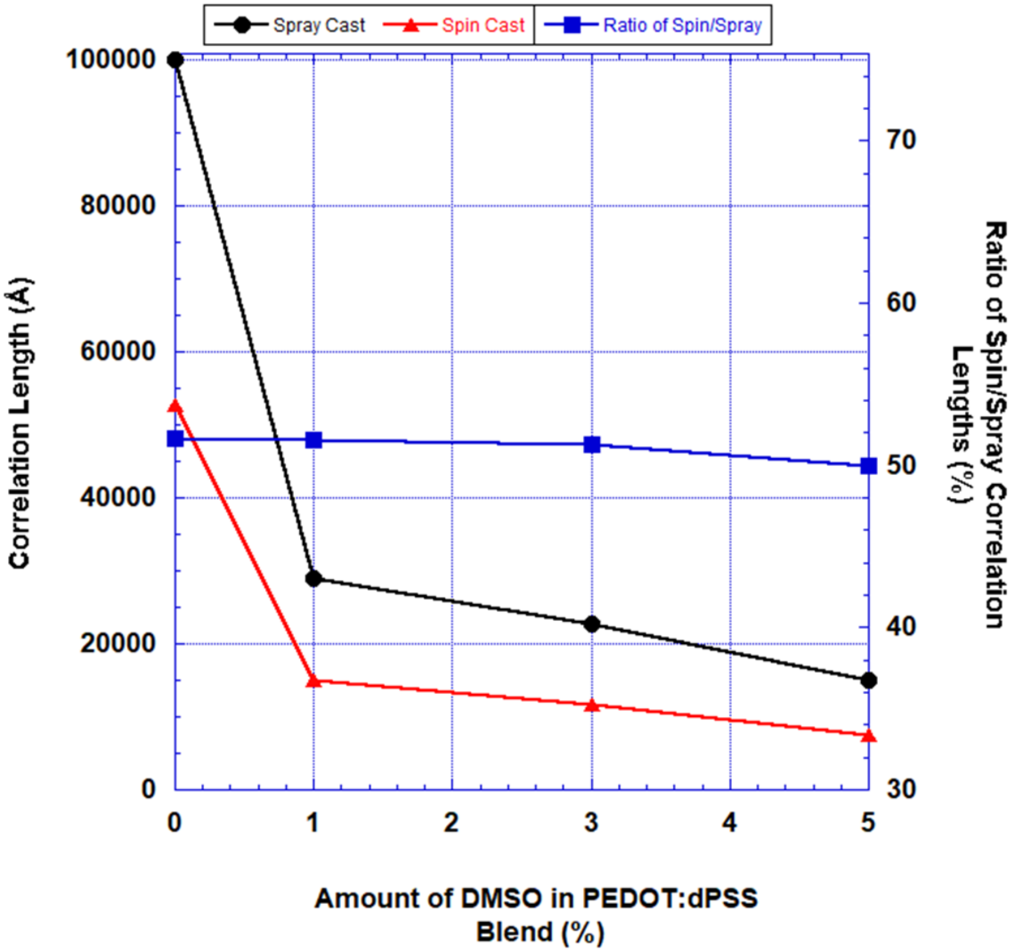

Figure II.5 – Comparison of changes in domain size, as monitored by correlation length, of PSS:PEDOT films with the addition of DMSO to pre-deposition solutions for both spin- (red triangles) and spray- (black spheres) coated samples. The ratio of the correlation lengths of spin-coated to spray-coated films (blue squares) remains constant and is denoted on the right axis.

is exemplified by plotting the ratio of the domain size in the spin-coated samples to that in the spray-coated samples, where this ratio is consistently about 50%. Accordingly, the domains in the spray-coated films are systematically twice as large as those in the spin-coated films. This observed difference in structure with a change in film formation conditions is consistent with reported smoothness and size changes showing that spin-coated films have consistently smoother surfaces with increased conductivity relative to spray-coated films.[7,9] This is also qualitatively consistent with the significant increase of conductivity of PSS:PEDOT films when 1% DMSO is added to the pre-deposition solution, which is followed by smaller increases in conductivity when increasing the DMSO concentration to 3% and 5%.[6]

Given the similarity of the morphology of both the spin-coated and spray-coated films with the addition of DMSO, it is our interpretation that the structure of the deposited films are guided by the structure of the PSS:PEDOT assemblies that exist in solution prior to deposition. PSS:PEDOT forms aggregates in the aqueous solution. Consequently, addition of DMSO to a PEDOT:PSS aqueous solution disrupts the conductive PEDOT assemblies, thereby creating smaller PSS domains in solution, as depicted in Figure II4a. Even though the PEDOT fibrils remain encapsulated by a layer of PSS, the smaller fibril assemblies remain in proximity to one another and the distance between the domains decreases. The PSS layer between the fibril assemblies also decreases as a result. This thin insulating PSS layer with small PEDOT fibrils enables a relatively smooth and more conductive film to form which translates to the observed morphology of the domains in the film upon deposition. We ascribe the large increase in conductivity with the addition of up to 5%

DMSO in the pre-deposition solution to the formation of smaller dPSS domains in solution with well aligned PEDOT fibrils.

However, the difference in domain size in the phase separated blend films with coating procedure appears to be primarily influenced by solvent evaporation during film formation. The formation of consistently smaller domains in the films deposited using spin coating can be attributed to the faster evaporation times commonly experienced in spin-coating techniques. For instance, in spin coating, the solution spreads quickly and evenly, coating the entire surface while excess solvent in the solution is cast beyond the edge of the Si substrate. Subsequent drying allows the remaining solvent to evaporate quickly and evenly throughout the film. In comparison, when spray coating a solution onto a silicon substrate, the small droplets of solution impact the surface and dynamically spread in a localized area, each leaving a polymer solution droplet on the film surface. Additional spray passes deposit additional droplets. By dynamically wetting the substrate, a uniform film is created on the surface. During film formation, the solvent coalesces as a thicker layer on top of the film than that in the spin-coated samples. Evaporation time of the solvent during annealing takes longer in spray-coated samples than in spin-coated, and this slow drying allows for the polymer to aggregate more in the process. Smaller domains are therefore found in the faster evaporating spin-coated samples than in the spray-coated samples. Thus, samples formed by spin-coating exhibit a more well dispersed network of smaller connected domains than spray-coated samples, which results in smoother surfaces and improved performance. It is interesting that this variation with coating technique does not fluctuate with the addition of DMSO to the solution, strongly suggesting that the presence of the DMSO does not alter the relative evaporation kinetics of the two deposition techniques.

A subset of the samples reported here (pristine and 5%wt DMSO PEDOT:dPSS films created by spray coating) coincide with samples that have previously been studied using SANS/USANS.[7] Qualitatively, the results reported here are consistent with those reported previously, however previous studies report smaller domain and PEDOT fibrillar structures. We believe that the quantitative difference can be ascribed to variation in substrate and slight deviation in deposition conditions that were required to enable the direct comparison of spin and spray-coated samples in this study. These changes resulted in the formation of thicker samples in this study than were examined on the previous study. The thicker films contain larger domains and aggregates, as demonstrated by the large correlation lengths reported in Table II.1. It is interesting that the impact of this increased film thickness does not appear to alter the underlying physics that control film formation with the addition of DMSO to the pre-deposition solution, as the structure of dPSS domains and PEDOT fibrils in the final conjugated polymer blend film follow similar trends for all systems studied.

Conclusions

The neutron scattering results reported here provide insight into the structure of PEDOT:dPSS thin films over length scales that range from angstroms to microns. These results show that the addition of DMSO to pre-deposition PEDOT:dPSS polymer blend aqueous solutions significantly decreases the correlation length of the fabricated phase separated blend film, regardless of deposition technique. The decrease in correlation length is greatest when just 1% DMSO is added to the PEDOT:dPSS polymer blend and continues to decrease with the addition of 3% DMSO and 5% DMSO. These results demonstrate an increased dispersion of the PSS domains, which results in the improved alignment of PEDOT fibrils within the domains. Smaller domains with well aligned fibrils are consistent with previously observed increased conductivity of PEDOT:PSS films formed from solutions containing DMSO.

Spin coating PEDOT:dPSS films resulted in consistently smaller domains than ultra-sonic spray coating due to faster evaporation times, which inhibits aggregation of domains and traps the aligned PEDOT fibrils. However, the qualitative similarity in the changes in blend morphology for films formed with the two deposition techniques is interpreted to indicate that the structures of the deposited films are intimately dependent on the structure of the PSS:PEDOT assemblies that exist in solution prior to deposition. These results therefore provide important structural insight into the film formation process in conjugated polymer blend films, which is valuable in rationally designing film fabrication procedures to attain targeted morphologies and performance.

Acknowledgement

This work was supported by the National Science Foundation DMR-1808946. A portion of this research used resources at the High Flux Isotope Reactor and Spallation Neutron Source, a DOE Office of Science User Facility operated by the Oak Ridge National Laboratory. Access to CHRNS Very Small-angle Neutron Scattering provided by the Center for High Resolution Neutron Scattering, a partnership between the National

Institute of Standards and Technology and the National Science Foundation under Agreement No. DMR-2010792. We acknowledge the support of the National Institute of Standards and Technology, U.S. Department of Commerce, in providing the neutron research facilities used in this work.

References

1. Heuer, H. W.; Wehrmann, R.; Kirchmeyer, S. Electrochromic window based on conducting poly (3,4-ethylenedioxythiophene)poly(styrene sulfonate). Advanced Functional Materials 2002, 12 (2), 89-94 DOI: 10.1002/1616-3028(20020201)12:2<89::aid-adfm89>3.0.co;2-1.

2. Andersson, P.; Nilsson, D.; Svensson, P. O.; Chen, M. X.; Malmstrom, A.; Remonen, T.; Kugler, T.; Berggren, M. Active matrix displays based on all-organic electrochemical smart pixels printed on paper. Advanced Materials 2002, 14 (20), 1460-+ DOI: 10.1002/1521-4095(20021016)14:20<1460::aid-adma1460>3.0.co;2-s.

3. Daoud, W. A.; Xin, J. H.; Szeto, Y. S. Polyethylenedioxythiophene coatings for humidity, temperature and strain sensing polyamide fibers. Sensors and Actuators B-Chemical 2005, 109 (2), 329-333 DOI: 10.1016/j.snb.2004.12.067.

4. Xia, Y. J.; Sun, K.; Ouyang, J. Y. Solution-Processed Metallic Conducting Polymer Films as Transparent Electrode of Optoelectronic Devices. Advanced Materials 2012, 24 (18), 2436-2440 DOI: 10.1002/adma.201104795.

5. Kim, G. H.; Shao, L.; Zhang, K.; Pipe, K. P. Engineered doping of organic semiconductors for enhanced thermoelectric efficiency. Nature Materials 2013, 12 (8), 719-723 DOI: 10.1038/nmat3635.

6. Dimitriev, O. P.; Grinko, D. A.; Noskov, Y. V.; Ogurtsov, N. A.; Pud, A. A. PEDOT:PSS films-Effect of organic solvent additives and annealing on the film conductivity. Synthetic Metals 2009, 159 (21-22), 2237-2239 DOI: 10.1016/j.synthmet.2009.08.022.

7. Etampawala, T.; Tehrani, M.; Nematollahi, A.; He, L. L.; Dadmun, M. The impact of solvent doping on the morphology and performance of spray-coated PEDOT:dPSS: A USANS and SANS study. Organic Electronics 2017, 51, 86-93 DOI: 10.1016/j.orgel.2017.08.030.

8. Murphy, R. J.; Weigandt, K. M.; Uhrig, D.; Alsayed, A.; Badre, C.; Hough, L.; Muthukumar, M. Scattering Studies on Poly(3,4-ethylenedioxythiophene)-Polystyrenesulfonate in the Presence of Ionic Liquids. Macromolecules 2015, 48 (24), 8989-8997 DOI: 10.1021/acs.macromol.5b02320.

9. Zabihi, F.; Xie, Y.; Gao, S.; Eslamian, M. Morphology, conductivity, and wetting characteristics of PEDOT:PSS thin films deposited by spin and spray coating. Applied Surface Science 2015, 338, 163-177 DOI: 10.1016/j.apsusc.2015.02.128.

10. Kim, J. Y.; Jung, J. H.; Lee, D. E.; Joo, J. Enhancement of electrical conductivity of poly(3,4-ethylenedioxythiophene)/poly(4-styrenesulfonate) by a change of solvents. Synthetic Metals 2002, 126 (2-3), 311-316 DOI: 10.1016/s0379-6779(01)00576-8.

11. Ouyang, J.; Xu, Q. F.; Chu, C. W.; Yang, Y.; Li, G.; Shinar, J. On the mechanism of conductivity enhancement in poly (3,4-ethylenedioxythiophene): poly(styrene sulfonate) film through solvent treatment. Polymer 2004, 45 (25), 8443-8450 DOI: 10.1016/j.polymer.2004.10.001.

12. Kim, Y. H.; Sachse, C.; Machala, M. L.; May, C.; Muller-Meskamp, L.; Leo, K. Highly Conductive PEDOT:PSS Electrode with Optimized Solvent and Thermal Post-Treatment for ITO-Free Organic Solar Cells. Advanced Functional Materials 2011, 21 (6), 1076-1081 DOI: 10.1002/adfm.201002290.

13. Ashizawa, S.; Horikawa, R.; Okuzaki, H. Effects of solvent on carrier transport in poly(3,4-ethylenedioxythiophene)/poly(4-styrenesulfonate). Synthetic Metals 2005, 153 (1-3), 5-8 DOI: 10.1016/j.synthmet.2005.07.214.

14. Heller, W. T.; Cuneo, M.; Debeer-Schmitt, L.; Do, C.; He, L. L.; Heroux, L.; Littrell, K.; Pingali, S. V.; Qian, S.; Stanley, C.; Urban, V. S.; Wu, B.; Bras, W. The suite of small-angle neutron scattering instruments at Oak Ridge National Laboratory. Journal of Applied Crystallography 2018, 51, 242-248 DOI: 10.1107/s1600576718001231.

15. Groenendaal, B. L.; Jonas, F.; Freitag, D.; Pielartzik, H.; Reynolds, J. R. Poly(3,4-ethylenedioxythiophene) and its derivatives: Past, present, and future. Advanced Materials 2000, 12 (7), 481-494.

16. Jonas, F.; Heywang, G. Technical applications for conductive polymers. Electrochimica Acta 1994, 39 (8-9), 1345-1347 DOI: 10.1016/0013-4686(94)e0057-7.

17. Jonas, F.; Krafft, W.; Muys, B. Poly(3,4-ethylenedioxythiophene) - conductive coatings, technical applications and properties. Macromolecular Symposia 1995, 100, 169-173 DOI: 10.1002/masy.19951000128.

18. Jukes, P. C.; Martin, S. J.; Higgins, A. M.; Geoghegan, M.; Jones, R. A. L.; Langridge, S.; Wehrum, A.; Kirchmeyer, S. Controlling the surface composition of poly(3,4-ethylene dioxythiophene)poly(styrene sulfonate) blends by heat treatment. Advanced Materials 2004, 16 (9-10), 807-+ DOI: 10.1002/adma.200306487.

19. Lefebvre, M.; Qi, Z. G.; Rana, D.; Pickup, P. G. Chemical synthesis, characterization, and electrochemical studies of poly(3,4-ethylenedioxythiophene)/poly(styrene-4-

sulfonate) composites. Chemistry of Materials 1999, 11 (2), 262-268 DOI: 10.1021/cm9804618.

20. Wignall, G. D.; Bates, F. S. Absolute calibration of small-angle neutron-scattering data. Journal of Applied Crystallography 1987, 20, 28-40 DOI: 10.1107/s0021889887087181.

21. Wignall, G. D.; Littrell, K. C.; Heller, W. T.; Melnichenko, Y. B.; Bailey, K. M.; Lynn, G. W.; Myles, D. A.; Urban, V. S.; Buchanan, M. V.; Selby, D. L.; Butler, P. D. The 40 m general purpose small-angle neutron scattering instrument at Oak Ridge National Laboratory. Journal of Applied Crystallography 2012, 45, 990-998 DOI: 10.1107/s0021889812027057.

22. Barker, J. G.; Glinka, C. J.; Moyer, J. J.; Kim, M. H.; Drews, A. R.; Agamalian, M. Design and performance of a thermal-neutron double-crystal diffractometer for USANS at NIST. Journal of Applied Crystallography 2005, 38, 1004-1011 DOI: 10.1107/s0021889805032103.

23. Borreguero, J. M.; Campbell, S. I.; Delaire, O. A.; Doucet, M.; Goswami, M.; Hagen, M. E.; Lynch, V. E.; Proffen, T. E.; Ren, S.; Savici, A. T.; Sumpter, B. G.; Tms, Integrating Advanced Materials Simulation Techniques into an Automated Data Analysis Workflow at the Spallation Neutron Source. 2014; p 297-308.

24. S. R. Kline; Reduction and analysis of SANS and USANS data using IGOR ProJ. Appl. Cryst. 2006, 39, 895-900 https://doi.org/10.1107/S0021889806035059

25. Ilavsky, J. and P. R. Jemian (2009). "Irena: tool suite for modeling and analysis of small-angle scattering." Journal of Applied Crystallography 42: 347-353.

26. Archibald, R. K.; Doucet, M.; Johnston, T.; Young, S. R.; Yang, E.; Heller, W. T. Classifying and analyzing small-angle scattering data using weighted k nearest neighbors machine learning techniques. Journal of Applied Crystallography 2020, 53, 326-334 DOI: 10.1107/s1600576720000552.

27. Debye, P.; Bueche, A. M. Scattering by an Inhomogeneous Solid. Journal of Applied Physics 1949, 20 (6), 518-525 DOI: 10.1063/1.1698419.

28. Debye, P.; Anderson, H. R.; Brumberger, H. Scattering by an Inhomogeneous Solid .2. The Correlation Function and Its Application. Journal of Applied Physics 1957, 28 (6), 679-683 DOI: 10.1063/1.1722830.

29. Svergun, D. I.; Semenyuk, A. V. Solution Of Integral-Equations Of The Convolution Type In The Processing Of Data On Small-Angle Experiment. Kristallografiya 1987, 32 (6), 1365-1372.

30. L A Feigin and D I Svergun, *Structure Analysis by Small-Angle X-Ray and Neutron Scattering*, Plenum, New York, (1987)

31. G.M. Newbloom, K.M. Weigandt, D.C. Pozzo, Electrical, mechanical, and structural characterization of self-assembly in poly(3-hexylthiophene) organogel networks, Macromolecules 45 (2012) 3452e3462.

32. H.P. Chen, J.H. Chen, W. Yin, X. Yu, M. Shao, K. Xiao, K.L. Hong, D.L. Pickel, W.M. Kochemba, S.M. Kilbey, M. Dadmun, Correlation of polymeric compatibilizer structure to its impact on the morphology and function of P3HT: PCBM bulk heterojunctions, J. Mater. Chem. A 1 (2013) 5309e5319.

Chapter III Surface Structure of Bicontinuous Microemulsions on Hydrophilic and Amphiphilic Substrates.

Abstract

Microemulsions (MEs) are a popular research topic with many industrial applications. Recent developments have shown that MEs can be utilized for electrochemical applications, including potentially in large-scale batteries. Understanding the structure and dynamics of these systems is needed to understand and direct their electrochemical behavior. While some bulk solution measurements have provided insight, surface structures also impact the electron (to the electrode) and ion (across the surfactant) charge transfer processes in the system. Neutron reflectivity has been performed using a series of deuterated water (D_2O)/Tween-20/Toluene ME compositions on hydrophilic and amphiphilic surfaces to determine the interface's structure between an electrode and a bulk ME. The surface structures formed by these solutions demonstrate that they form layered structures near the hard electrode surface. Decreasing the D_2O concentration in the ME increases the number of and purity of the layers established on the solid surface. These lamellar-type layers transition from the surface to the bulk microemulsion as a series of mixed layers (i.e., contain oil, water, and surfactant) that are consistent with the perforation of the lamellae. Additionally, these mixed lamellae may become more perforated with oil and water pathways on an amphiphilic surface. The purity and thickness of these layers can limit charge transport, where increased purity directly at the electrode surface would increase electron transfer. In contrast, perforated pathways through the lamellae increase the ion transfer through the oil, surfactant, and water boundary.

Introduction

Interest in microemulsions (ME) has spanned several decades. Research efforts focused on their use in various industrial applications from food products to pharmaceuticals and healthcare to energy materials, with a recent concentration on their electrochemical functionality for use in energy-related devices.[1-5] MEs consist of oil, water, and surfactants with a hydrophilic head group and a hydrophobic tail group. [6-7] The head and tail of the surfactant molecules arrange at the interface between these immiscible liquids of oil and water, where the hydrophilic head aligns with the water phase, while the hydrophobic tail aligns with the oil/non-polar phase. These mixtures create one of 3 types of emulsions, oil droplets in water (O/W), water droplets in oil (W/O), or a bicontinuous microemulsion (BME).[6-10] BMEs, also known as Winsor III-type (W-III) emulsions, are low-viscosity, isotropic mixtures that naturally occur when separate continuous oil and water channels form with the surfactant acting as the boundary lowering the interfacial tension between the oil channel and the water channel.[7,9,10] Research has shown that BME structures consist of well-distributed channels in the bulk.[5,10] However, preferential layering of the oil and water at solid surfaces occurs due to the polarity of the surface, oil, water, and surfactant.[11-14] Leading to an interruption of the bicontinuous morphology in a region near the surface, impacting transport properties. This ordering at the surface is important given that until more recently research on the electrochemical behavior of microemulsions has focused on the bulk structure of these systems, with few studies focusing on the impact of surface morphology on their performance.[4,1216-15,16]

In electrochemical applications, charge transport must occur at the electrode surface, where the electrode hydrophobicity can vary with the polarity of the electrode material. This variation in polarity, ranging from hydrophilic to hydrophobic, can direct the ME structure at the surface, which can differ substantially from that of the bulk structure.[11,13,177,188] To understand how the surface ordering of a ME relates to electrochemical performance, the self-assembly of the ME near an impenetrable surface must be determined over a variety of hydrophilicities to provide insight into the behavior of the ME near a range of potential electrode surfaces. Neutron reflectivity is one method that provides the required resolution and contrast control to determine the surface ordering of MEs for this purpose.[188,19] Using deuterated water (D_2O) in the microemulsion system, the contrast in scattering length density (SLD) between the protonated oil/surfactant and the D_2O increases. This strong contrast provides the required resolution and statistics to elucidate the structure of the surfactant/oil and water mixture in the system and is used to determine the morphology of the microemulsion at a surface.[14] Previous studies have shown that bicontinuous microemulsions may form near-lamellar, ordered structures at a hard surface that can vary with surface polarity.[13,177,19] These lamellae may also perforate as more well-ordered near-surface layers transition to the bicontinuous structure of the bulk. The layered structure and transition to a bicontinuous bulk are dependent on the surface polarity and the presence of an applied stress parallel to the interface.15[15,1919] Growing interest in renewable energy devices has increased research on microemulsions for electrochemical storage devices, focusing on the lamellar structures that form at the surface of the electrode and how the functionality of the device changes with these structures.[2,4,9,177]

Recent studies have shown that microemulsions do not stop the transfer of electrons at the surface of an electrode or the transfer ions within the microemulsion from the oil phase to the water phase.[4, 20] Bard, *et al.*, demonstrated electron and ion transfer using cyclic voltammetry and collision experiments, where the addition of an ionic liquid allowed both electron transfer and ion transfer.[20] It is postulated that when the electron transfers from a redox active agent in the surfactant, either a negative ion transfers out of or a positive ion may transfer into the aqueous phase through the surfactant.[20] Peng *et al.* also observed that structuring a 66% water BME at the surface allowed the transfer of electrons from the electrode to the ferrocenium and a compensatory transfer of an ion from the surfactant head to the aqueous solution.[4] The bicontinuous channels in the microemulsion examined in this study are 48 Å on average and form layers on an amphiphilic electrode.[4]

It is important to understand the correlation of the ordering of a microemulsion near a surface to its electrochemical performance, we have explored the near surface ordering of a series of bicontinuous microemulsions on surfaces of varying hydrophilicity. Neutron reflectivity monitors the surface structure of BMEs as a function of microemulsion composition, where the microemulsion incorporates deuterated water to increase contrast in the scattering experiments. The ordering of the bicontinuous microemulsion near the impenetrable surfaces provides insight into the role of surface ordering on the electrochemical performance of BMEs. These surface measurements can also provide guidance to design electrode surfaces for improved performance in electrochemical applications.

Experimental methods

Microemulsion Preparation

All ME compositions were prepared by using an 82.5% Tween®-20 (poly(ethylene glycol) (20) sorbitan monolaurate, Sigma Aldrich, St Louis, MO), 17.5% 1-butanol (purity >99%, Sigma Aldrich), by mass as the emulsifier. The emulsifier then had a constant 10:1 mass ratio with the oil. In these mixtures, the Tween®-20 serves as the surfactant, with hydrophilic head groups and hydrophobic tail groups, and the 1-butanol is the co-surfactant with the Tween®-20 helping reduce the interfacial tension further. For neutron reflectivity, MEs were prepared as 80% D_2O, 60% D_2O, and 30% D_2O, by volume. The remaining contents of the microemulsion were an emulsifier/toluene (high-performance liquid chromatography [HPLC] grade, Fisher Scientific, Pittsburgh, PA) mixture. ME compositions studied are presented in the ternary phase diagram of the Tween-20/Toluene/D_2O system in Figure III.1. Additionally, the phase diagram shows the phase boundary between the two-phase and one-phase regions, as previously reported for this system.[4] Microemulsion solutions were prepared and provided by Brian Barth of the Zawodinski group at the University of Tennessee Knoxville.

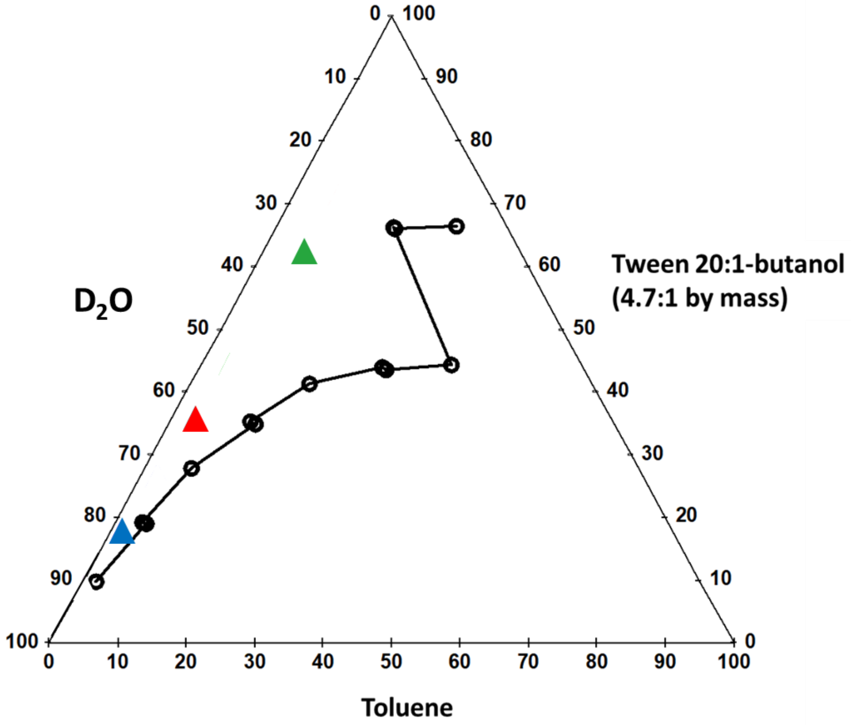

Figure III.1 – Ternary phase diagram of microemulsion examined, including concentrations studied in neutron reflectivity measurements. Colored triangles indicate examined compositions (30% D_2O- green, 60% D_2O-red, and 80% D_2O-blue). Black line indicates phase boundary between 1 and 2 phase domains.

Neutron Reflectometry

Silicon substrates of varying hydrophilicity were prepared in advance of the neutron scattering experiments. Each silicon surface was first cleaned with a piranha solution (3:1 sulfuric acid/hydrogen peroxide) to remove any surface contaminants. Both Si wafers were then exposed to UV-Ozone to create a controlled hydrophilic silicon oxide surface.

The first Si wafer, referred to as the hydrophilic substrate, was then used as prepared. The other Si wafer was transferred to a glove box, where the amphiphilic surface was prepared by silanization of the wafer. The reaction proceeded by placing the oxidized wafer in a 4 wt% n-octadecyltrimethoxysilane solution in toluene for three days. The amphiphilic substrate was then sonicated in toluene for 30 minutes prior to being rinsed with toluene and dried with air. The water contact angle of each substrate was then determined to quantify its hydrophilicity, where the hydrophilic substrate was found to have a water contact angle of 23°, while the amphiphilic substrate has a water contact angle of 66°.

Neutron reflectivity measurements were performed on the NG7 horizontal axis reflectometer at the NIST Center for Neutron Research. The MEs were loaded into a solution cell on the horizontal axis reflectometer, where the neutrons travel through the Si substrate to the SiO_x-microemulsion interface. Neutrons then reflect off the structure at the interface, where changing the incident angle controls the depth of the scattered neutrons.[22,23] The resulting intensity of reflected neutrons is then recorded as a function of wavevector, Q, which is defined as, $Q = \frac{4\pi \sin(2\theta)}{\lambda}$. In this equation, λ is the wavelength of the neutrons, and 2θ is the angle of reflection. ME samples were loaded as prepared into solution cells with either the hydrophilic (Silicon) substrate or the amphiphilic (Silane) substrate. Reflectivity curves were obtained over a Q-range of 0.005 $Å^{-1}$ to 0.15 $Å^{-1}$. Data reduction was performed using Reductus software, and data analysis was performed by fitting the measured reflectivity curve to a multi-layer model using IGOR Pro 8 with the Motofit add-on for reflectometry.[21,24,25] Fits were performed using least-squares methods to minimize the error between the measured data and the calculated fit, where the quality of the fit is reported as the square of the gradient χ^2. Initially, genetic optimization was applied to find global minimum χ^2, followed by the Levenberg-Marquardt method to find the local minimum χ^2.[23] χ^2 is calculated using Equation 3.1 as described in the literature, where L is the number of points in the data, P is the number of points in the fit, $y_{n,obs}$ represents the observed intensity of the reflected neutron beam, while $y_{n,calc}$ is the calculated intensity in the least-squares fit, and $y_{n,err}$ is the local error between the fitted value and the actual measurements. [24]

$$\chi^2 = \sum_{n=1}^{L} \frac{1}{L-P} \left(\frac{y_{n,obs} - y_{n,calc}}{y_{n,err}} \right)^2 \qquad \text{Equation 3.1}$$

$$\rho_z = \sum_{i=0}^{N} \frac{\rho_i - \rho_{i+1}}{2} \left(1 + err \frac{z - z_i}{\sqrt{2\sigma_i}} \right) \qquad \text{Equation 3.2}$$

The SLD profile, ρ_z, is then determined using Equation 3.2, where N is the total number of layers, ρ is the scattering length density of each layer, err is the error function, z is the distance from the solid-liquid interface, and σ is the roughness between the layers. To further confirm the results of the reflectivity data, the mass balance as an integral of volume fraction profiles of D_2O in each microemulsion were calculated and not allowed to deviate more than 10% from known values. These calculations are presented in the supporting information.

The mass balance, MB, as an integral of volume fraction profiles of D_2O in each microemulsion across the surface structure was calculated using Equation 3.3,

$$MB = \int Vol. Frac. of D_2O(z)dz = \int \frac{SLD_{D2O-} - SLD_{meas}(z)}{SLD_{D2O-} + SLD_{oil+surf}} dz, \qquad \text{Equation 3.3}$$

where SLD_{D_2O} is the scattering length density of the D_2O (ca. 6.393×10^{-6} Å^{-2}), $SLD_{meas}(z)$ is the scattering length density of the microemulsion at depth z, and $SLD_{oil+surf}$ is the total scattering length density of the protonated components of toluene and the surfactant (ca. 4.83×10^{-7} Å^{-2}). The composition profiles of the layers were calculated as a function of distance from the solid-liquid interface. The mass balance results, shown in Table III.1, were all within ±5% of the expected values. The calculated mass balance indicates that the systems maintain expected concentrations within the surface structures consistent with the bulk solution.

Results

Reflectivity Results

Neutron reflectivity data for the hydrophilic wafer, dry, in contact with D_2O, and with all three MEs are presented in Figure III.2. In contrast, Figure III.3 shows the reflectivity curves for these same conditions for the amphiphilic wafer. Figures III.2 and III.3 also include the fits to the experimental data using the multi-layer model to determine the structure of each ME near the hydrophilic and amphiphilic surfaces.

Table III.1- Calculated mass balances of D_2O at the Si surface from Equation 3.

Substrate	30% D_2O	60% D_2O	80% D_2O
Hydrophilic Si	32.69	61.94	75.27
Amphiphilic Silane	29.97	60.85	80.10

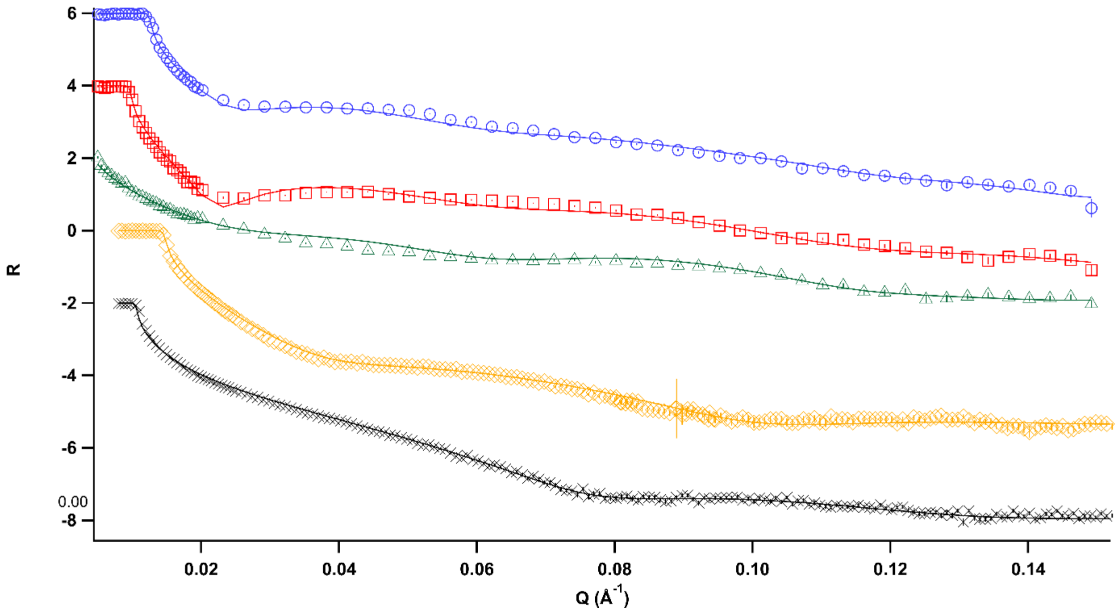

Figure III.2 – Neutron reflectivity data and fits of Dry (black), Wet (orange), 30% D_2O (green), 60% D_2O (red), and 80% D_2O (blue) on hydrophilic Si Substrate.

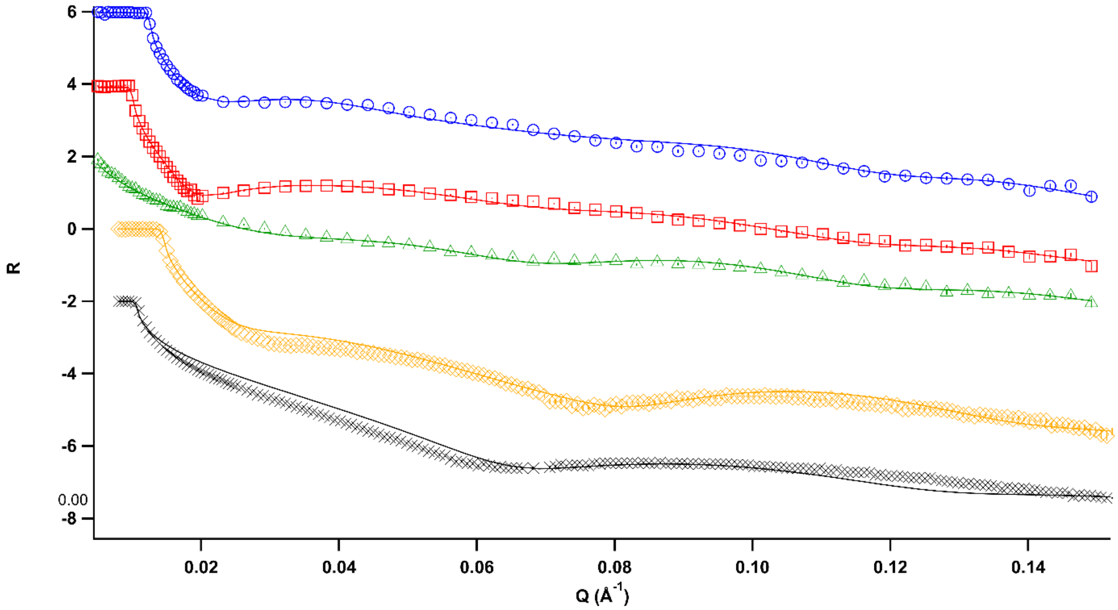

Figure III.3 – Neutron Reflectometry data and fits of Dry (black), Wet (orange), 30% D_2O (green), 60% D_2O (red), and 80% D_2O (blue) on amphiphilic Si Substrate.

Figures III.4 and III.5 show the scattering length density profiles of all three MEs near the hydrophilic and amphiphilic surfaces, respectively. Figures III.2 through III.5 also show the reflectivity curves and scattering length density profiles resulting from the fitting process for each wafer dry (in the air) and in contact with D_2O. The structural details of all samples studied on the hydrophilic and amphiphilic substrates are listed in Tables III.2 and III.3, respectively. All fits had a $\chi^2 < 0.04$. The scattering length density of each layer in the samples as determined by the reflectivity fits of the various compositions on a hydrophilic substrate are presented in Table III.2, while the fits for compositions on the amphiphilic substrate are presented in Table III.3. Moreover, the calculated SLDs of the components in the microemulsion or silicon wafer are presented in Table III.4.

Structure of Si Substrates

Inspection of the results reveals the structure of the hydrophilic and amphiphilic surfaces in air and D_2O. These results confirm an oxidized layer (SiO_x) on each substrate that formed from treating the wafer with piranha and UV-Ozone. The hydrophilic substrate in the air has an oxidation layer 84 Å thick and an SLD of 2.700×10^{-6} Å^{-2}, which confirms the formation of SiO_x. For the Si substrate with the silane, the SiO_x layer was found to be 97 Å thick, with an SLD of 3.390×10^{-6} Å^{-2}.

The SiO_x layer on the amphiphilic wafer transitions into a silane layer that is 51 Å thick with an SLD of 0.358×10^{-6}Å^{-2}, which is higher than the estimated $\mathrm{SLD}_{\mathrm{Silane}} = -0.157x10^{-6}$ Å^{-2}. This variation can be attributed to the capture of moisture from the atmosphere attracted to the hydrophilic Si in both the silane and at the SiO_x layer during this experiment. The thickness of the pure silane layer (51 Å) is also larger than

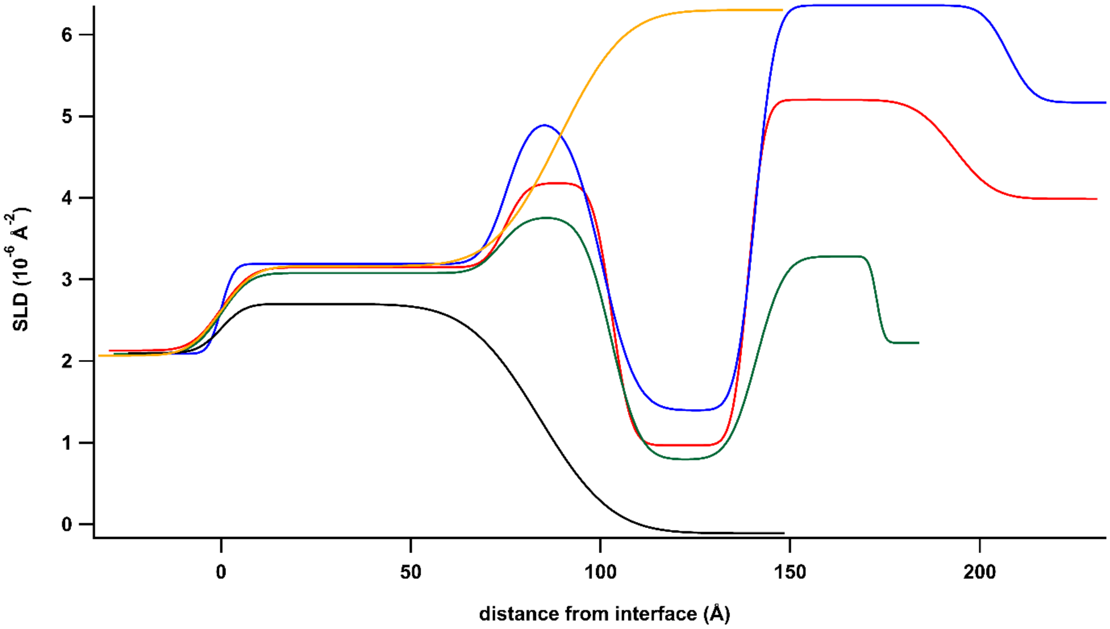

Figure III.4 – Scattering length density profile of Dry (black), Wet (orange), 30% D_2O (green), 60% D_2O (red), and 80% D_2O (blue) on hydrophilic Si Substrate.

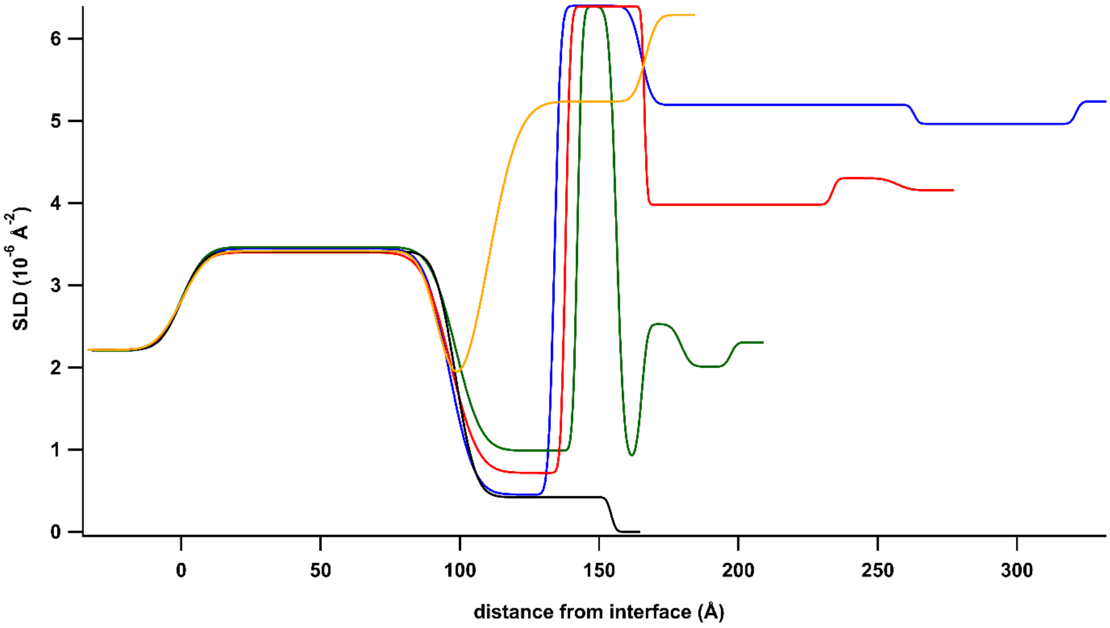

Figure III.5 – Scattering length density profile of Dry (black), Wet (orange), 30% D_2O (green), 60% D_2O (red), and 80% D_2O (blue) on amphiphilic Si Substrate.

Table III.2 - Scattering length density (SLD x 10^{-6} Å^{-2}), thickness (z, Å), and roughness (R, Å) of layers in microemulsions on hydrophilic Si substrate determined from reflectometry fits.

Microemulsion		SiOx	Layer 1	Layer 2	Layer 3	Bulk
Dry	SLD	2.700	-	-	-	0.000
	Z	84.0	-	-	-	-
	R	14.9	-	-	-	4.9
Wet	SLD	3.164	-	-	-	6.302
	Z	89.1	-	-	-	-
	R	6.8	-	-	-	13.5
80% D_2O	SLD	3.190	4.537	1.230	6.360	5.169
	Z	75.2	31.7	39.2	70.4	-
	R	2.6	5.7	2.1	4.3	5.6
60% D_2O	SLD	3.149	4.036	0.967	5.202	3.988
	Z	75.0	31.2	36.1	54.3	-
	R	6.1	4.3	4.0	3.4	8.1
30% D_2O	SLD	3.079	3.767	0.793	3.283	2.223
	Z	73.6	29.2	38.4	31.7	-
	R	5.9	5.2	6.0	5.8	1.6

Table III.3 - Scattering length density (SLD x 10^{-6} Å^{-2}), thickness (z, Å), and roughness (R Å of layers in microemulsions on amphiphilic silane substrate determined from reflectometry fits.

Microemulsion		SiOx	Layer 1	Layer 2	Layer 3	Layer 4	Layer 5	Bulk
Dry	SLD	3.390	0.358	-	-	-	-	0.000
	Z	97.2	50.8	-	-	-	-	-
	R	9.9	1.1	-	-	-	-	1.1
Wet	SLD	3.416	1.249	5.236	-	-	-	6.289
	Z	92.6	17.3	56.7	-	-	-	-
	R	7.2	5.6	8.8	-	-	-	3.2
80% D_2O	SLD	3.445	0.453	6.399	5.194	4.963	-	5.236
	Z	96.2	37.8	31.1	98.0	58.1	-	-
	R	6.8	7.1	1.7	3.0	1.4	-	1.5
60% D_2O	SLD	3.398	0.717	6.392	3.981	4.301	-	4.156
	Z	96.6	41.4	28.3	67.5	23.2	-	-
	R	6.7	7.9	1.4	0.8	1.5	-	3.9
30% D_2O	SLD	3.464	0.987	6.390	0.880	2.527	2.009	2.305
	Z	98.5	43.7	14.0	9.1	14.1	17.7	-
	R	6.7	7.3	1.3	2.1	1.6	2.7	1.7

Table III.4 - Calculated scattering length density of components in microemulsion systems.

Component	Density (g/cm^2)	Ca. SLD (x10^{-6} Å^{-2})
Si	2.329	2.073
SiO	2.130	2.897
SiO_2	2.200	3.475
D_2O	1.110	6.393
Toluene	0.867	0.941
1-butanol	0.810	-0.330
Tween®20	1.100	0.594
n-octadecyltrimethoxysilane	0.883	-0.155
Emulsifier (82.5% Tween-20/17.5% 1-butanol)	*ca.* 1.049	0.432
Protonated components of ME (10:1 ratio Emulsifier: Toluene)	*ca.* 1.031	0.483

the expected size of a dry n-octadecyltrimethoxysilane monolayer, which has been previously reported to be 21 Å and calculated from Avogadro Geometry Optimization to be 25 Å. Therefore, these results indicate that the silane forms multiple (2-3) layers on the Si surface during the silanization reaction.

When the hydrophilic surface is in contact with D_2O, the SiO_x layer is hydrated, as evidenced by the SLD increasing to $3.164 x 10^{-6}$ $Å^{-2}$, while the layer thickness increased from 84 Å to 89 Å. This experiment also shows that a transition layer exists between the SiO_x layer and the bulk D_2O, $SLD_{D_2O} = 6.393x10^{-6} Å^{-2}$. The SLD and thickness of the SiO_x layer on the amphiphilic substrate did not vary with water. However, the silane layer did contract when exposed to water, where the silane layer thickness decreases to 17 Å when exposed to water.

This collapse of the silane layer coupled to the emergence of an additional transitional layer between pure silane and pure D_2O can be attributed to the adsorption of D_2O into the top portion of the silane layer. Since the water contact angle is 66° on the silane, it is reasonable that water and oil may penetrate this porous layer to some extent. While the oil will adsorb on the n-octadecyltrimethoxysilane chains, water is attracted to the Si attached to the substrate through the porous silane. Therefore, in a pure water environment the silane may adapt to allow water to penetrate. The composition of this transitional layer appears to be dominated by D_2O, as its SLD is $5.236 x 10^{-6}$ $Å^{-2}$. Moreover, the thickness of this transitional layer is 56.7 Å that, when combined with the thickness of the pure silane layer (17.3 Å), reveals that the silane layer partially swollen with water is *ca*. 23.2 Å thicker than the dry silane layer.

The final layer in the SLD profiles in Figures III.4 and III.5 are the bulk system that is not influenced by the presence of the surface. For dry substrates, this layer air (SLD=0.000x10^{-6} Å^{-2}), and for wet substrates, this layer is pure D_2O (SLD=6.393x10^{-6} Å^{-2}). For each ME, the composition and SLD of the final layers is dependent on the concentrations of water/surfactant/oil in the specific microemulsion. All of the layers have lower SLDs than that of pure D_2O and higher than that of the emulsifier/oil mix. In the following analysis and discussion, if the SLD of a layer is higher than that of the bulk microemulsion SLD, the layer is termed D_2O-rich. Conversely, if the layer has an SLD lower than that of the bulk solution, the layer is considered emulsifier-rich.

Ordering of the Microemulsions on a Hydrophilic substrate

The layered structure of all MEs on the hydrophilic surface, shown in Figure III.4, exhibits similar trends. The MEs form three layers between the silicon surface and the bulk microemulsion. The Si wafer consists of the bulk silicon, topped with a *ca.* 73.6 Å to 89.1 Å silicon oxide layer, as shown in the wet and dry samples. Each ME produces a layer next to the SiO_x layer that has an SLD greater than the SiO_x layer. A higher SLD corresponds to more D_2O in the layer, and the maximum SLD of each layer increases from 3.767x10^{-6} Å^{-2}, 4.036x10^{-6} Å^{-2}, and 4.537x10^{-6} Å^{-2} as the D_2O concentration increased from 30%, 60%, and 80%, respectively. The increased SLD in the layer demonstrates that D_2O appears to be attracted to the SiO_x surface, although it is not pure D_2O and therefore must be a mixture of D_2O and oil/emulsifier. This is because the calculated SLDs of the components in the system are 6.393x10^{-6} Å^{-2}, 0.941x10^{-6} Å^{-2}, and 0.432x10^{-6} Å^{-2} for D_2O, toluene, and the emulsifier, respectively. Thus, any layer with an SLD above 0.941x10^{-6} Å^{-2} must contain some D_2O, and any layer with an SLD below 6.393x10^{-6} Å^{-2} must contain some oil and/or surfactant. Therefore, the initial layer of the microemulsion on the hydrophilic surface appears to be a mixture of water and surfactant head group. The SLD of this first layer scales with the amount of D_2O in the system, further indicating that the amount of oil/surfactant in the layer neighboring the surface increases with a decrease in water concentration. Regardless of microemulsion composition, this initial layer is consistently around 30 Å thick, although growing roughness when less water is in the system. This roughness may be attributed to the fact that at lower D_2O concentrations, the lower contrast between layers results in a decrease in reflectivity, manifesting as an increase in interlayer roughness due to limited resolution between these layers.

The second layer that forms in the microemulsion is mainly composed of surfactant/oil, as indicated by the low SLD (~ 1 x 10^{-6} Å^{-2}) of the layer. Only the 30% ME has an SLD below 0.941x10^{-6} Å^{-2} indicating the absence of water in this layer. Also, the 60% and 80% D_2O samples form a second layer with SLDs of 0.967x10^{-6} Å^{-2} and 1.280x10^{-6} Å^{-2}, respectively, suggesting both layers have some D_2O but are predominately protonated oil/emulsifier. Similar to the layer next to the SiO_x, this layer also retains an equal thickness for all D_2O compositions (~37Å). At the same time, the roughness of the layering increases with the decrease in scattering intensity.

The third layer formed after the surfactant/oil-rich layer represents another D_2O-rich layer, as indicated by the increase in SLDs above the bulk values of each microemulsion. In this layer, the SLDs for the 30%, 60%, and 80% D_2O samples are 3.283x10^{-6} Å^{-2}, 5.202x10^{-6} Å^{-2}, and 6.360x10^{-6} Å^{-2}, respectively. This layer in the 80%

D_2O microemulsion is nearly pure D_2O, while the layers formed in the 30% and 60% microemulsions show modest D_2O concentrations. Additionally, the 80% D_2O and 60% D_2O have SLDs above the SLD of the layer adjacent to the SiO_x surface and the bulk layer. In comparison, this layer in the 30% D_2O microemulsion has an SLD lower than the layer near the SiO_x but higher than the bulk microemulsion. An indication that there is more D_2O in the D_2O-rich third layer than at the SiO_x surface for the higher water concentrations. However, for 30% D_2O microemulsion, more water is present at the SiO_x-liquid interface than in the third layer.

Each ME forms three well-defined layers between the solid-liquid interface and the bulk solution on the hydrophilic surface. From the Si surface to the bulk, these layers alternate from high concentration of D_2O to an emulsifier/oil-rich layer followed by another water-rich layer. The compositions of these layers vary with overall ME composition as expected that is more D_2O is in the D_2O-rich layers for the MEs with higher water content. Additionally, the thicknesses of the first two layers do not vary with ME composition, while the thickness of the third layer scales with the amount of water in the ME.

Microemulsion Ordering on an Amphiphilic Substrate

The ordering of the MEs on the amphiphilic silane surface, as shown in Figure III.5, is organized to a different structure than observed on the hydrophilic surface, Figure III.4, while maintaining a similar general layering. On this surface, the analysis of the reflectivity data shows the presence of the *ca.* 50 Å silane layer on the *ca.* 100 Å SiO_x layer, as demonstrated in the SLD profiles of the dry (air) and wet (D_2O) samples. It is worth noting that the increase in the SLD of the silane layer in the presence of D_2O indicates penetration of the D_2O into the porous amphiphilic layer. When the 30%, 60% , and 80% D_2O MEs are in contact with the amphiphilic surface, the contents of the ME also penetrate the silane, increasing its SLD as more ME penetrates the layer. Interestingly, the presence of the emulsifier and water appears to compress the silane layer. The 30% D_2O ME compresses this layer to 44Å, while the 60% D_2O (41Å) and 80% D_2O (38Å) MEs compress the layer further. The SLDs (and composition) of this layer also show interesting changes with ME composition. The silane layer in the presence of the 80% D_2O ME has a low SLD (0.453×10^{-6} Å^{-2}) close to the SLD of only the protonated components. However, the silane layer with the 60% D_2O ME increases its SLD slightly to 0.717×10^{-6} Å^{-2}. Moreover, the SLD of the silane increases further to 0.987×10^{-6} Å^{-2} with the 30% D_2O ME. This silane layer maintains an SLD lower than that of toluene in the presence of the 60% and 80% D_2O MEs, suggesting that the layer is swollen by emulsifier/oil but not water. The size and SLD of the silane layer with the 80% D_2O microemulsion indicate that a small amount of emulsifier/oil penetrates this amphiphilic layer, increasing its SLD. However, the presence of the surfactant boundary between the oil and water phases allows the water to compress the silane/emulsifier in the oil phase while little D_2O penetrates the layer resulting in an overall compression of the silane. As the amount of water in the microemulsion decreases, the SLD of this layer increases, suggesting more emulsifier/oil penetrates the layer. At the same time, the thickness of this layer increases, consistently correlating the amount of water in the microemulsion to the amount of layer compression. Thus, with more emulsifiers and oil in the microemulsion, the silane adsorbs the oil or emulsifier, raising the SLD of the layer. In all cases, the presence of the microemulsion compresses the thickness of the silane-surfactant/oil layer relative to that of the dry silane thickness.

A layer rich in D_2O exits in all MEs, with SLDs between 6.389x10^{-6} Å^{-2} (30%) and 6.399x10^{-6} Å^{-2} (80%) that neighbors the silane-emulsifier/oil layer. This layer is present in all the MEs and has an SLD comparable to D_2O indicative of a nearly pure D_2O layer forming next to the silane-emulsifier/oil layer. However, the thickness varies with the concentration of D_2O. Careful inspection shows that this layer in the 80% D_2O ME is at its thickest (31 Å) while decreasing slightly in the 60% D_2O microemulsion to *ca.* 28 Å, and a thickness of 14 Å in the 30% D_2O ME. Indicating that while a nearly pure water layer does form, the layer thickness is constrained by the composition of the ME and the thickness and composition of its surrounding layers.

Further from the silane layer beyond this D_2O-rich layer, each ME forms multiple layers with SLDs fluctuating between oil-rich and D_2O-rich before reaching the bulk ME. The number, depth, and breadth of the oscillations are directly correlated with the ME composition. The 80% D_2O ME forms thick neighboring layers of 98.0 Å and 58.1 Å, where the SLD of these layers (5.194x10^{-6} Å^{-2} and 4.963x10^{-6} Å^{-2}) are both slightly below the bulk microemulsion SLD of 5.236x10^{-6} Å^{-2}. This suggests that in this ME, the compositions of these layers differ somewhat from that of the bulk and must form three-dimensional morphologies that connect the highly ordered layering at the surface to the tortuous bicontinuous morphology of the bulk. A decrease in water loading in the ME to 60% D_2O leads to a similar structure, where two neighboring layers exist but are slightly thinner with layer thicknesses of 67.5 Å and 23.2 Å. Layers in the 60% D_2O ME alternate from the SLD of the penultimate layer (SLD = 3.981x10^{-6} Å^{-2}), being lower than the bulk (SLD =

4.16×10^{-6} Å^{-2}), while the SLD of the last layer (SLD = 4.301×10^{-6} Å^{-2}) increases back above that of the bulk. This alternating layering indicates that the concentration of each layer is fluctuating between emulsifier-rich and D_2O-rich layers. Layers with SLDs that are close to the bulk solution indicate the presence of both emulsifier/oil and D_2O in these layers, suggesting the formation of three-dimensional morphologies that connect the highly ordered layering at the surface to the bulk bicontinuous morphology. The 30% D_2O ME layers show a similar alternating structure, where the layers alternate in SLD below and above that of the bulk solution. However, in this ME, the layering decreases further in thickness (9.1 Å, 14.1 Å, and 17.7 Å), accompanied by an increase in the number of distinct layers from two to three. Furthermore, the change in SLD is more extreme (8.80×10^{-7} Å^{-2}, 2.527×10^{-6} Å^{-2}, and 2.009×10^{-6} Å^{-2}) before reaching the bulk solution (SLD = 2.305×10^{-6} Å^{-2}). Interestingly, the total thickness of the three layers combined (41 Å) is similar to the estimated thickness of the domains of the surfactant channels measured by a collaborator in the bicontinuous bulk morphology (21 Å - 45 Å, which is the distance from one Tween®-20 head group to the next Tween®-20 head group). However, the difference of SLDs between layers in the 30% D_2O ME increases as compared to the 60% D_2O and the 80% D_2O ME implying the layering is well defined between the emulsifier/oil-rich and D_2O-rich transitional layers, that is the layers decrease in thickness but increase in richness of either emulsifier or D_2O.

Discussion

Hydrophilic surface structures

The neutron reflectivity results clearly show that each of the MEs forms three definite layers on the hydrophilic surface before reaching the bulk composition at 175-200 Å from the silicon wafer surface. The layer closest to the SiO_x surface is a mixture of emulsifiers and D_2O, and the amount of D_2O in this layer increases with increasing D_2O loading. However, this initial layer is not D_2O-rich for the 60% and 80% D_2O MEs, as the peak SLD for this layer is less than that of the bulk ME. Unfortunately, the composition of the layer does not precisely identify the morphology of the ME at the surface. However, careful interpretation of the layers can provide insight into the ME structure in the near-surface layers.

D_2O and the hydrophilic headgroups of the surfactant are attracted to the hydrophilic SiO_x surface creating a mixed layer that contains water and surfactant. One morphology, illustrated in Figure III.6a, consistent with this mixed layer, contains elongated droplet-like aggregates of surfactant that enclose oil in a continuous water phase. This assembly has been suggested in previous studies of microemulsions and creates perforations in the water lamellae by oil/surfactant droplets.[9,11] These perforations can be thought of as channels between layers of oil and water separated by surfactant boundaries, forming the BME channels. As the concentration of water decreases, the volume fraction of the surfactant head groups on this layer increases, consistent with the decreasing SLD of this layer as the ME composition changes from

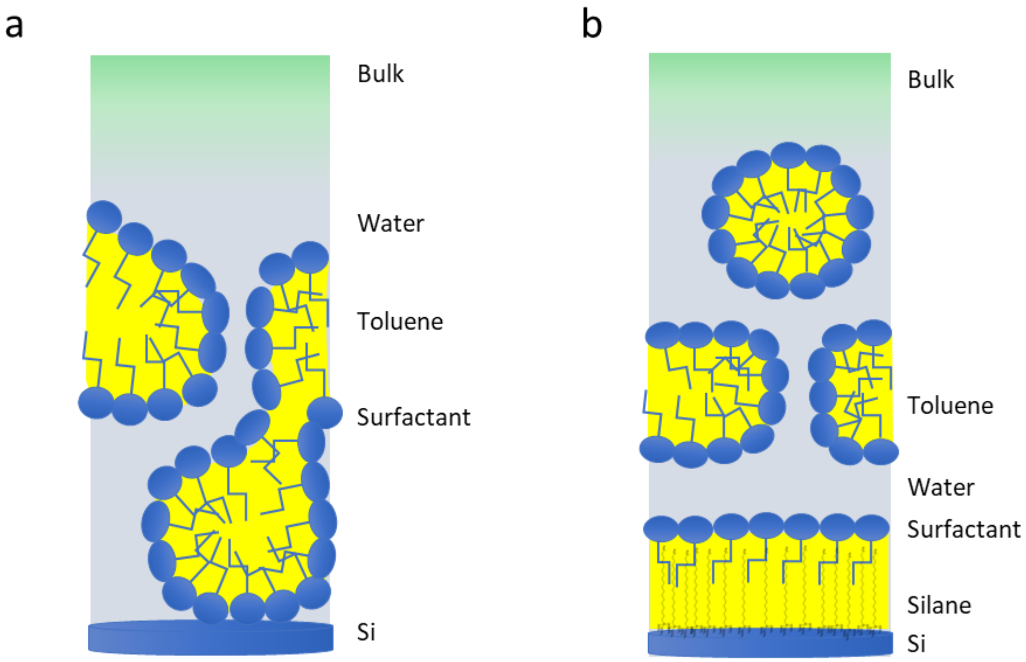

Figure III.6 – Sketch of proposed microemulsion structures at a hydrophilic Si surface (a) and amphiphilic silane surface (b), illustrating how lamellar may form with perforations as they approach the bulk solution.

80% to 60% and 30% D_2O. Moreover, the thickness of this layer remains around 31 Å, which is near the reported size of the surfactant molecule, 35 Å,[4, 7], suggesting the size of the surfactant molecule and its alignment (nearly) perpendicular to the surface controls the thickness of this layer.

The transition from the first to the second layer consists of a mixture of hydrated surfactant headgroups and oil with the surfactant tails, which then transitions to an oil-rich layer. However, this layer consists primarily of oil and surfactant. At higher D_2O concentrations, the SLD increases, which can be attributed to the presence of small water channels throughout the continuous surfactant/oil layer. The SLD of this layer in the 30% D_2O ME indicates the layer being dominated by emulsifier and toluene. The SLD of this layer in the 60% and 80%D_2O ME is higher, meaning increased D_2O in this layer. The increased amount of D_2O appears to drive the surfactant to enclose a region of toluene in the layer, allowing small pockets of D_2O to exist in this layer. These pockets of D_2O are the beginning perforations that form as the distance from the solid-liquid interface increases.

The initial layers formed are distinct and may have droplets of oil/emulsifiers in water or hydrated surfactant heads. However, further from the surface, the SLD of the layers approaches the bulk through dampening fluctuations in SLD. The closer the measured SLD of the layer is to the bulk SLD indicates a mixture of oil/emulsifier and water that more closely resembles the bulk solution. Therefore, as the SLD approaches the bulk, perforations of oil in D_2O-rich layers or D_2O in oil-rich layers increase gradually, transitioning to the bulk solution where oil and water channels with the emulsifier at the interface have formed the bicontinuous morphology of the bulk.

The third layer that forms in the MEs on a hydrophilic surface has SLDs that indicate a D_2O-rich layer, where the amount of D_2O in the layer increases with ME D_2O content. In the 80% D_2O ME, the layer is almost pure D_2O and thicker than any other layer discussed yet. The dominant presence of water in this layer forms a lamella encompassed by the surfactant/oil-rich layer closer to the surface and the bulk microemulsion further from the surface. Inspection of this layer in the 60% D_2O ME shows a thinner layer and a lower SLD than the 80% D_2O ME. Hence, this layer is a mixture of emulsifier/oil and D_2O, which suggests that it contains emulsifier/oil aggregates in a primarily D_2O layer, forming perforations of the water layer. The structure of this layer in the 30% D_2O ME further suggests that perforations of emulsifier/oil aggregates are developing in the D_2O-rich lamellae. In this layer, the SLD is still above that of the bulk SLD and is mostly water. However, the SLD of this layer in the 30% ME is lower than the same layer in the 60% or 80% D_2O MEs, indicating more oil and less water in this layer relative to the composition of this layer in MEs with higher D_2O loadings.

Overall, the MEs form a triple layer assembly on the hydrophilic surface, alternating between D_2O-rich, emulsifier/oil-rich, and D_2O-rich layers. In the D_2O-rich layers, increased D_2O loading in the ME corresponds to higher D_2O loading in each layer. The layers are not pure D_2O or emulsifier/oil, indicating that droplets of the minor phase perforate the layers. Additionally, the transitions between surfactant-rich and D_2O-rich layers are gradual, consistent with forming channels between the layers.

Ordering of the Microemulsions on the Amphiphilic surfaces

On the amphiphilic surface, the MEs assemble slightly differently than on the hydrophilic surface. The amphiphilic surface contains a porous grafted silane layer that forms the first layer near the SiO_x layer. This silane layer is penetrated by the emulsifier and oil while compressed by the D_2O, resulting in an SLD and layer decrease with increasing D_2O. Adsorption of oil and emulsifier on the silane at this layer suggests the ME forms a layer of primarily hydrophobic surfactant tails and oil in the silane with minimal D_2O penetrating the silane. The sharp transition from the silane layer to the neighboring ME layer suggests that Tween®-20 surfactant heads align to form a boundary that is nearly parallel to, with the surfactant tails aligning perpendicular to, the surface and the surfactant bordering the adjacent D_2O-rich layer. The silane and surfactant tails are free move in the oil phase, while the boundary of surfactant heads creates a surface to where increased water in the microemulsion will compress it closer to the SiO_x layer. In all three MEs, the D_2O-rich layer is well-defined and nearly pure, which indicates the layering of the MEs on the amphiphilic surface is more definitive than their ordering of the hydrophilic surface.

These initial layers near the hard surface transition to multiple (2-3) layers that oscillate in composition (and SLD) above and below that of the bulk microemulsion. These layers in the 80% and 60% D_2O microemulsion contain D_2O-rich lamellae intermixed with patches of emulsifier/oil, or vice-versa. An additional layer is present in the 30% D_2O microemulsion (3), each with decreased thicknesses that dampen as they approach the bulk. These features suggest that the microemulsions form elongated surfactant aggregates in these layers at higher water content. These aggregates act as the boundaries between oil and water channels and increase in volume fraction as the layers approach the bulk solution, as illustrated in Figure III.6b. Interestingly, the SLD only varies slightly from the SLD of the bulk (± 5%), indicating that the layering in this area is not determinate for the 60% and 80% MEs. However, in the 30% D_2O microemulsion, the SLD oscillations beyond the first two layers are more significant (+10%, -50%), indicating that more defined layers form in these MEs and perforations in these layers are fewer than at higher D_2O loadings.

Impact of Surface Structures on Electrochemical Performance

Static measurements of the near-surface structures of microemulsions also provide insight into the MEs' potential electrochemical performance. Previous studies have determined that pure, thick layers of oil and surfactant or water inhibit charge transfer.[4,19,20] Therefore, the presence of mixed layers on a surface should provide pathways for charge transfer from the bulk to the surface, potentially increasing the rate of charge transfer at the electrode surface.

On the hydrophilic surface, the 30% D_2O and 60% D_2O MEs assemble into mixed layers near the surface that are consistent with perforated lamellae, which should be more conductive. The multiple pathways will allow efficient transfer of charges across the surfactant and to the electrode surface. However, the 80% D_2O ME forms a thick, nearly pure layer of D_2O that would inhibit charge transfer through this portion of the ME. Conversely, the 30% D_2O ME on the amphiphilic surface shows increased mixed layers, more fluctuations, and thinner layers than both the 60% D_2O and the 80% D_2O

MEs on the same surface, suggesting the 30% D_2O ME could allow charge transfer of ions across the surfactant boundary and electrons at the electrode surface. The increased availability of emulsifier/oil and water at the surface in a perforated lamellae should increase the charge transfer in the structures of these systems.

However, the MEs assemble into different layered structures on the amphiphilic surface. Here, the formation of pure (for all compositions) and thicker (for 60% D_2O and 80% D_2O) lamellae suggests the conductivity of a ME on this surface is limited. In contrast, a ME (30% D_2O and 60% D_2O) performance on the hydrophilic surface would benefit from the thinner and more perforated layering. Therefore, the formation of perforated lamellae in these MEs should increase charge transfer. Increasing the water concentration increases the thickness and purity of the surface layers, creating fewer pathways for charge conduction, leading to a prediction that charge transfer would be optimal on a hydrophilic surface and the 30% D_2O ME would exhibit significant conductivity on either a hydrophilic or amphiphilic electrode surface. However, it must be noted that these measurements monitor the structure of a static sample with no external electric field. The application of an electric field could alter these assemblies and alter charge transfer performance. Future experiments are planned to examine the assembly of microemulsions near various surfaces in an electric field.

Conclusions

The assembly of bicontinuous microemulsions near surfaces with varying hydrophilicity are monitored. Structures of different concentrations of BMEs in aqueous solutions on hydrophilic and amphiphilic substrates have been observed. The microemulsions examined here form multiple lamellar-like layers on hydrophilic and amphiphilic surfaces, where each layer is rich in water or emulsifier/oil. The layers transition to bulk material over 100-200 Å, where the layers can be described as perforated lamellae. MEs on the hydrophilic surface form layers consistent with perforated lamellae for all compositions studied. On the hydrophilic surface, the increased D_2O content forms thick D_2O-rich layers that may inhibit charge transfer. However, on the amphiphilic surface, the microemulsions form more layers that are rich in water or oil/emulsifier. Therefore, the MEs on the hydrophilic surface create perforated lamellar assemblies that provide pathways that should improve charge transfer near the surface.

The thicknesses of the layers decrease with decreased water content in these MEs on both surfaces. The 30% D_2O ME forms thinner layers relative to those formed in the 60% D_2O and 80% D_2O microemulsions, primarily when in contact with an amphiphilic surface. While thicker layers formed at a surface have been shown to inhibit charge transfer from the bulk to the electrode, these thinner surface structures may increase charge transfer at this surface.[4,20] Finally, the observed multiple mixed layers between the surfaces and the bulk solution are consistent with the existence of perforated lamellae, which will allow increased electrical performance due to the increased availability of pathways for charge transfer at an electrode surface.

Acknowledgments

This work was supported as part of the Breakthrough Electrolytes for Energy Storage (BEES), an Energy Frontier Research Center funded by the U.S. Department of

Energy, Office of Science, Basic Energy Sciences under Award# DE-SC0019409. We acknowledge the support of the National Institute of Standards and Technology, U.S. Department of Commerce, in providing the neutron research facilities used in this work.

References

1. Kalaitzaki A, Emo M, Stebe MJ, Xenakis A, Papadimitriou V. Biocompatible nanodispersions as delivery systems of food additives: A structural study. Food Research International. 2013;54(2):1448-1454.

2. del Rio JG, Hayes DG, Urban VS. Partitioning behavior of an acid-cleavable, 1,3-dioxolane alkyl ethoxylate, surfactant in single and binary surfactant mixtures for 2-and 3-phase microemulsion systems according to ethoxylate head group size. Journal of Colloid and Interface Science. 2010;352(2):424-435.

3. Lawrence MJ, Rees GD. Microemulsion-based media as novel drug delivery systems. Advanced Drug Delivery Reviews. 2000;45(1):89-121.

4. Peng J, Cantillo NM, Nelms KM, *et al.* Electron Transfer in Microemulsion-Based Electrolytes. ACS Applied Materials & Interfaces. 2020;12(36):40213-40219.

5. Kunitake M, Kuraya E, Kato D, Niwa O, Nishimi T. Electrochemistry in bicontinuous microemulsions based on control of dynamic solution structures on electrode surfaces. Current Opinion in Colloid & Interface Science. 2016;25:13-26.

6. Moumen N, Pileni MP, Mackay RA. Polymerization of methacrylate in a W O microemulsion stabilized by a methacrylate surfactant. Colloids and Surfaces a-Physicochemical and Engineering Aspects. 1999;151(3):409-417.

7. Mackay RA, Myers SA, Bodalbhai L, Brajtertoth A. Microemulsion structure and its effect on electrochemical reactions. Analytical Chemistry. 1990;62(10):1084-1090.

8. Kulkarni V, Shaw C. Essential Chemistry for Formulators of Semisolid and Liquid Dosages, Chapter 2 - Surfactants, Lipids, and Surface Chemistry, Page: 5-19 2016

9. Torrealba VA, Hoteit H, Johns RT. Description of Micellar Radii for Phase Behavior and Viscosity Modeling of Aqueous Surfactant Solutions and Microemulsions. Langmuir. 2018;34(50):15327-15334.

10. Makita Y, Uemura S, Miyanari N, *et al*. Electrochemical Investigation of Dynamic Solution Structures of Bicontinuous Microemulsion at Solid Interfaces. Chemistry Letters. 2010;39(11):1152-1154.

11. Vargas-Ruiz S, Soltwedel O, Micciulla S, *et al*. Sugar Surfactant Based Microemulsions at Solid Surfaces: Influence of the Oil Type and Surface Polarity. Langmuir. 2016;32(45):11928-11938.

12. Torikai N, Yamada NL, Noro A, *et al*. Neutron reflectometry on interfacial structures of the thin films of polymer and lipid. Polymer Journal. 2007;39(12):1238-1246.

13. Kuraya E, Nagatomo S, Sakata K, *et al*. Simultaneous Electrochemical Analysis of Hydrophilic and Lipophilic Antioxidants in Bicontinuous Microemulsion. Analytical Chemistry. 2015;87(3):1489-1493.

14. Lipfert F, Kerscher M, Mattauch S, Frielinghaus H. Stability of near-surface ordering of bicontinuous microemulsions in external shear-fields. Journal of Colloid and Interface Science. 2019;534:31-36.

15. Kawano S, Kobayashi D, Taguchi S, Kunitake M, Nishimi T. Construction of Continuous Porous Organogels, Hydrogels, and Bicontinuous Organo/Hydro Hybrid Gels from Bicontinuous Microemulsions. Macromolecules. 2010;43(1):473-479.

16. Mackay RA, Dixit NS, Hermansky C, Kertes AS. Conductivity and diffusion measurements in micellar and o/w microemulsion systems - a comparative-study. Colloids and Surfaces. 1986;21:27-39.

17. Huo L, Du P, Zhou H, Zhang K, Liu P. Fabrication and tribological properties of self-assembled monolayer of n-alkyltrimethoxysilane on silicon: Effect of SAM alkyl chain length. Applied Surface Science 396 (2017) 865–869

18. Zhou XL, Chen SH. Theoretical foundation of x-ray and neutron reflectometry. Physics Reports-Review Section of Physics Letters. 1995;257(4-5):223-348.

19. Zhou XL, Lee LT, Chen SH, Strey R. Observation of surface-induced layering in bicontinuous microemulsions. Physical Review A. 1992;46(10):6479-6489.

20. Deng HQ, Dick JE, Kummer S, Kragl U, Strauss SH, Bard AJ. Probing Ion Transfer across Liquid-Liquid Interfaces by Monitoring Collisions of Single Femtoliter Oil Droplets on Ultramicroelectrodes. Analytical Chemistry. 2016;88(15):7754-7761.

21. Maranville B, Ratcliff W, Kienzle P. Reductus: a stateless Python data reduction service with a browser front end. Journal of Applied Crystallography. 2018;51:1500-1506.

22. Nevot L, Croce P. Characterization of surfaces by grazing x-ray reflection - application to study of polishing of some silicate-glasses. Revue De Physique Appliquee. 1980;15(3):761-779.

23. Parratt LG. Surface studies of solids by total reflection of x-rays. Physical Review. 1954;95(2):359-369.

24. Nelson A. Co-refinement of multiple-contrast neutron/X-ray reflectivity data using MOTOFIT. Journal of Applied Crystallography. 2006;39:273-276.

25. P.A. Kienzle, K.V. O'Donovan, J.F. Ankner, N.F. Berk, C.F. Majkrzak; http://www.ncnr.nist.gov/reflpak. 2000-2006

Chapter IV The Evolution of Structure in Mixtures of Choline Chloride and Glycerol in Forming the Deep Eutectic Solvent Glyceline

Abstract

Deep Eutectic Solvents (DES) are similar to ionic liquids and are formed by heating immiscible pairs of solids that consist of a hydrogen bond donor and a hydrogen bond acceptor. These compounds thermodynamically mix when melted and form a solution that remains a liquid when cooled below the melting point of either individual component. DES have generated interest as potential components in large scale batteries at ambient temperatures due to the network of hydrogen bonds that form in the mixture that creates the potential for electrochemical behavior in the liquid. Glyceline, a mixture of 33% choline chloride (ChCl) in glycerol, forms networks of glycerol and chloride that develop with the addition of ChCl to glycerol. Neutron diffraction combined with deuteration of the DES components and molecular dynamics offers a robust method to monitor the evolution of the mixture structure as the composition approached the eutectic. The results show that the availability of the chloride ion to disrupt the intermolecular hydrogen bonding network that exists in pure glycerol is realized by the preference of choline to assemble with other choline molecules as the concentration of choline chloride increases and the solution approaches the eutectic point. Understanding the morphology of these mixtures and how their assembly change as Glyceline forms is critical to developing paths to improve their performance in electrochemical applications.

Introduction

Deep eutectic solvents (DES) have become a material class of keen interest since first reported by Abbott, *et al.*, in 2001.[1] DES are similar to ionic liquids that are moisture stable and have similar electrochemical behavior, including the potential to form conductive liquid structures.[1-4] However, the original components in a DES are usually immiscible at room temperature and only form a mixture with intricate hydrogen bonds when heated together.[1,5] These hydrogen bond networks are then maintained when cooled back to room temperature, where the solvent remains liquid well below the melting point of the individual components. [1,5] DES's rely on the formation of extensive hydrogen bonds at certain chemical compositions that include hydrogen bond donors (HBD), typically a halide salt, and acceptors (HBA), typically an alcohol, amide, or carboxylic acid . Many common mixtures form DES's and have been the topic of substantial research including Reline (ChCl:urea), Maline (ChCl:malonic acid), Ethaline (ChCl:ethylene glycol) and Glyceline (ChCl:glycerol).[6-10] These mixtures show some similar behavior to each other and to ionic liquids, where their mixed structure and presence of ions open the potential for their use in many applications including synthesis, gas adsorption, drug delivery and large-scale liquid battery energy storage. [7-16]

A large number of methods have been used to determine and analyze the structure and dynamics of DES's, including broadband dielectric spectroscopy, Raman spectroscopy, and neutron scattering.[5,17-21] The dynamics of DES have been measured over a broad range of compositions to show that the addition of a halide salt to the hydrogen bond donor solvent at a temperature above the melting point of this solvent allows the materials to mix and form conductive networks.[22-26] These mixtures can be tuned and used to store energy. Research to determine the structure and dynamics of DES's have been performed using X-ray and neutron scattering techniques to determine how the hydrogen bonds and interactions formed in the DES's change with solution composition and at elevated temperatures, and how this affects the energy storage performance of the material.[11,23,28] Neutron spectroscopy and neutron spin echo have determined that the glycerol is the major component in the hydrogen bond network formed in Glyceline.[29,30] Concurrently, wide angle neutron diffraction has been utilized to determine how the components of a mixture assemble to form a DES.[6,7,22,31-33] Neutron scattering offers an opportunity to dial in contrast between components by selective deuteration. This change in contrast provides a method to elucidate the structure of the hydrogen bonding network by examining the HBD and HBA independently and has been explored by deuteration of the different components as well as of the groups within a molecule.[32,33]

For instance, Holbrey, *et al*, have shown that the glycerol in the eutectic Glyceline (33%ChCl:glycerol) forms a hydrogen bond network that is disrupted at higher loadings of ChCl, i.e., at 50% ChCl:glycerol.[33] In this study, they report that choline enters interstitial voids in the hydrogen bond network that consists of glycerol and chloride anions, thereby acting like a plasticizer within this connected system, which only breaks up at higher concentrations of ChCl. The use of Empirical Potential Structure Refinement (EPSR), a Monte Carlo modeling method, aids in the analysis of the neutron diffraction studies.[22,31,33] However, molecular dynamics (MD) has also been used to computationally model liquid structures.[32] Simulations from both classical MD (CMD) and ab-initio MD (AIMD) build reliable interaction models between the molecules in the system and can provide molecular level insight into the assemblies that contribute to neutron diffraction data.[32]

Continued efforts have been made to determine the structures in DES's, such as Glyceline and Ethaline. Previously reported results of ChCl in ethylene glycol mixtures have shown that shifts in neutron diffraction peaks are modeled by CMD and further correlated by AIMD.[32] The shifts in these neutron diffraction peak positions and heights can be related to changes in structure by following coordination numbers of the functional groups in the hydrogen bonded network, employing spatial distribution functions (SDFs), and showing that the number of chloride ions increases in the first solvation shell of ethylene glycol in the DES Ethaline.

Dynamic measurements of Glyceline have shown that on the sub-nanometer scale, the diffusion of choline occurs faster than that of glycerol, which is contrary to the translational diffusion that is measured on macroscopic scales.[30] The faster localized diffusive motions of choline, where the long-range diffusion is inhibited, are potentially due to glycerol being spatially constrained by its interactions with chloride.[29,30]

In this work, we combine neutron diffraction measurements and classical molecular dynamics to monitor the change in structure in mixtures of choline chloride and glycerol (ChCl:Gly) as a function of ChCl loading up to the reported eutectic point of Glyceline (33%ChCl:glycerol). These data provide insight into the change in assembly and structure of the glycerol hydrogen bonding network as the eutectic is approached. Combining neutron diffraction and CMD results provides detailed insight into how the interactions develop between the choline anion, chloride cation and glycerol hydrogen bond network in the formation of the deep eutectic solvent, Glyceline.

Experimental methods

Solvent Preparation and Measurements

The total neutron scattering of mixtures of choline chloride and glycerol with varying compositions of choline chloride were measured using d-choline chloride (trimethyl-d9, 98%) and d-glycerol (d8, 99%). Both deuterated components were purchased from Chemical Isotopes Laboratory. A representation of the molecules in the mixtures are shown in Figure IV.1, where individual atoms are labeled. These labels will be used in the analysis of data to elucidate the presence or absence of specific pairwise interactions. Glycerol was fully deuterated whereas choline was deuterated only at the methyl groups on the nitrogen ion. The glycerol/choline chloride mixtures were prepared in a glove box with $\leq$ 0.2ppm O_2, where choline chloride was heated at 378 K for 2 hours. The glycerol was heated to 353 K and choline chloride was added at molar ratios of 0:1 (0%ChCl), 1:2 (33% ChCl), 1:6 (18% ChCl), 1:9 (10% ChCl), and 1:19 (5% ChCl) choline chloride to glycerol. After a 1-hour solvation period, solutions were cooled to room temperature, then sealed in 3 mm diameter quartz capillaries with a height of at least 1.5 cm for the scattering experiment.

The total neutron scattering measurements were performed at the Nanoscale Ordered Materials Diffractometer at the Spallation Neutron Source at Oak Ridge National Laboratory over a diffraction range of Q = 0.1 A^{-1} up to Q = 30 A^{-1}, where the Q, the transfer of momentum of a scattered neutron, is defined by $Q = \frac{4\pi \sin(\theta)}{\lambda}$. Here θ

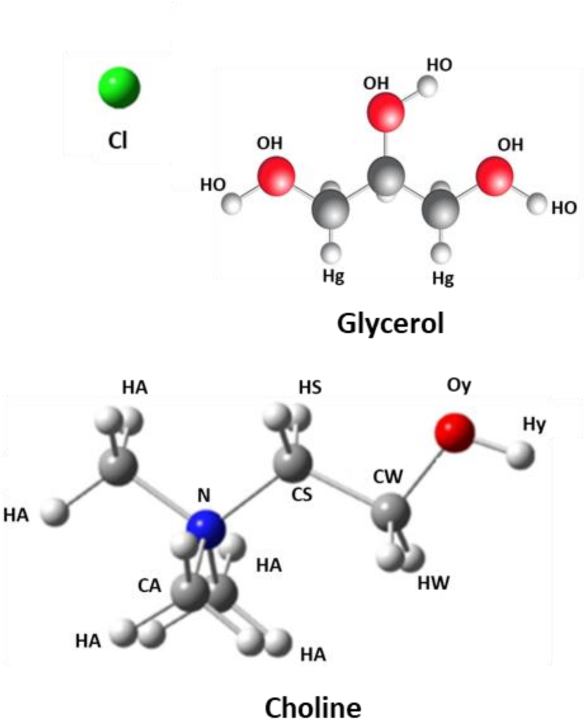

Figure IV.1 – Representation of molecules used in ChCl:glycerol studies. Atoms and groups are labeled for RDF and coordination number analysis. All hydrogens (H) in glycerol and on hydrogens on methylene groups (HA) in choline are deuterated for neutron diffraction.

is the scattering angle and λ is the wavelength of the scattered neutrons.[34] The total scattering curve is measured in 30-minute intervals, where multiple sets of the same composition were summed together prior to reduction to improve statistics. The structure factor, $S(Q) = \frac{I_{coh} - I_{poly}}{I_{poly}} + 1$, of the samples were obtained by reducing the raw scattering data using ADvanced DIffraction Environment (ADDIE) by normalizing the coherent scattering, I_{coh}, to polymorphic standard scattering data, I_{poly}. Coherent scattering was obtained by subtracting quartz capillary background scattering from the total sample scattering and normalizing to scattering from vanadium.[34,35]

Molecular Dynamics

Fully atomistic equilibrium molecular dynamics simulations were performed with the LAMMPS package with the inter- and intra-molecular interactions described by the general AMBER force field (GAFF).[36,37] Initial molecular configurations of glycerol and choline molecules were optimized via Gaussian 09 using a B3LYP/aug-cc-pvdz basis set and Lennard-Jones (LJ) sigma and epsilon values for atoms were adapted from a study by Perkins *et al.*[38,39] Atomic partial charges were adapted from the same study but with a change in overall choline and chloride net charges from the study's 0.9 e to this study's 0.7 e in order to more correctly match eutectic mixture behavior as a function of choline chloride content.[38,39] Glycerol partial atomic charges were unmodified from the referenced paper.[38,39] Related studies from a collaborating group showed that Perkins *et al.*'s force field worked well at 33 mol% ChCl, but it did not correctly replicate mixture dynamics trends at lower concentrations of choline chloride, necessitating the more aggressive charge scaling to 0.7 e. For all LAMMPS simulations, a 1 fs timestep, velocity

Verlet integrator, all periodic boundary conditions, 12 Å cutoff for both LJ and Coulombic interactions with tail corrections, and a particle-particle particle-mesh long range solver were used.

Simulation boxes were filled a specific number of glycerol and choline chloride molecules to achieve the desired ChCl mol% in glycerol, the details of which are in Table IV.1. Initial conformations were loosely and randomly packed into a cube with Packmol.[40,41] All simulations were run at 300K. The systems were first equilibrated for 2 ns with an isothermal isobaric (NPT) ensemble at one atmosphere ensuring that the last 1 ns achieved a converged density and total energy. The average box dimensions of the last 1 ns were used to initialize a canonical (NVT) ensemble production runs of 20 ns for all systems except for pure glycerol, which needed 40 ns to reach the diffusive regime and ensure adequate conformational sampling for structural analysis. A Nosé-Hoover-chain thermostat and Nosé-Hoover-chain barostat with a chain length of 3 and time constant of 100 fs were used for all applicable simulations.

Molecular dynamic simulations and probabilities of coordination numbers were performed and provided by Derrick Poe of Dr. Maginn's group at the University of Notre Dame. Preparation of mixtures, neutron scattering, and lead of data analysis were performed by Luke Heroux of Dr. Dadmun's group at the University of Tennessee.

Results

Structure Factors

Wide angle neutron diffraction (ND) curves of 0%, 5%, 10%, 18%, and 33% mixtures of choline chloride (ChCl) in glycerol were measured. The raw data were reduced to obtain

Table IV.1 - Composition of molecular dynamics simulation boxes

ChCl mol%	Number of Glycerol	Number of ChCl	Number of Total Atoms
0	715	0	10010
5	665	35	10080
10	612	68	10064
18	533	117	10036
33	400	200	10000

the structure factor S(Q) of each sample as a function of Q over a Q-range of 0.5Å^{-1} to 32 Å^{-1} as shown in Figure IV.2. Figure IV.2 shows the change in scattering intensity and peak position as the composition of the ChCl/glycerol mixture changes. However, the scattering intensity above $Q = 10$ Å^{-1} is low and varies little with Q, and therefore are not included in the further analysis. Therefore, the S(Q) over a range from 0.5 Å^{-1} to 10 Å^{-1} is the focus of the analysis and is shown in Figure IV.3A. The overall trends observed in the structure factor with increasing ChCl loading can be interpreted to provide insight into how the structure of the mixture and hydrogen bonding network of the glycerol emerges with addition of ChCl. The position of peaks in the experimentally determined S(Q) can be related to the density distribution function of the sample through Fourier transformation, and thus can be interpreted to quantify the average distances between two atoms or functional groups. The intensity of diffraction peaks in S(Q) are proportional to the number of interactions between the atoms or functional groups. An inverse Fourier transform can be performed on measured S(Q) data to provide a real-space representation of structure through radial distribution functions (RDF's) represented by g(r) plots. The RDF describes the isotopic positioning of molecules within the system. Alternatively, the radial distribution function of the system can be calculated using CMD simulations. For instance, Figure IV.4 shows the g(r) of two hydroxyl groups in glycerol as determined by CMD. The simulated neutron scattering structure factor, S(Q)$^{\text{sim}}$, of this assembly can then be determined by taking its Fourier transform as shown in Equation 4.1.

$$S(Q)^{sim} = \frac{\rho_0 \Sigma_i \Sigma_j x_i x_j f_i f_j \int_0^{L/2} 4\pi r^2 \left(g_{ij}(r)-1\right) \frac{\sin(qr)}{qr} W(r)\, dr}{[\Sigma_i x_i f_i]^2} \qquad \text{Equation 4.1}$$

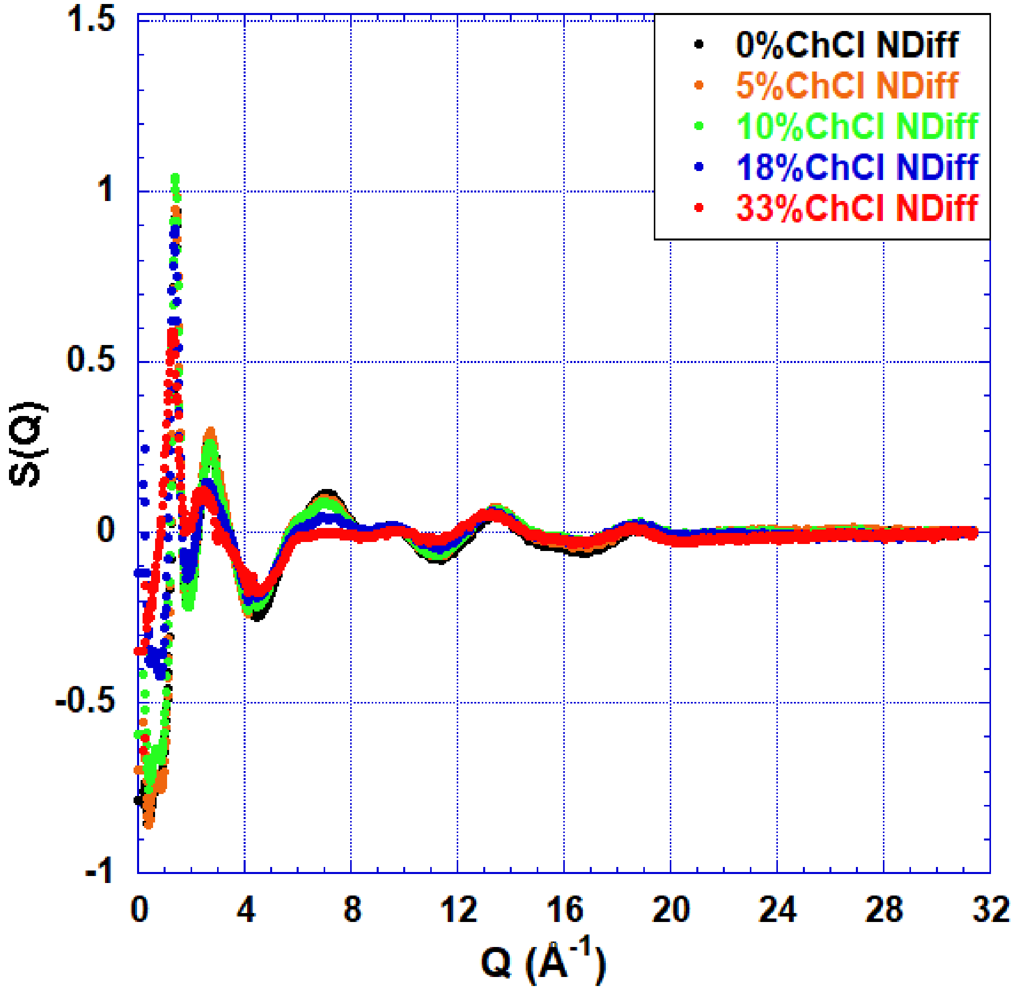

Figure IV.2 – Structure factor plot of total scattering from neutron diffraction (dots) on compositions of 0% (red), 5% Orange, 10% (green), 18% blue, and 33% (black) ChCl:glycerol over the range of Q= 0 Å^{-1} to 32Å^{-1}.

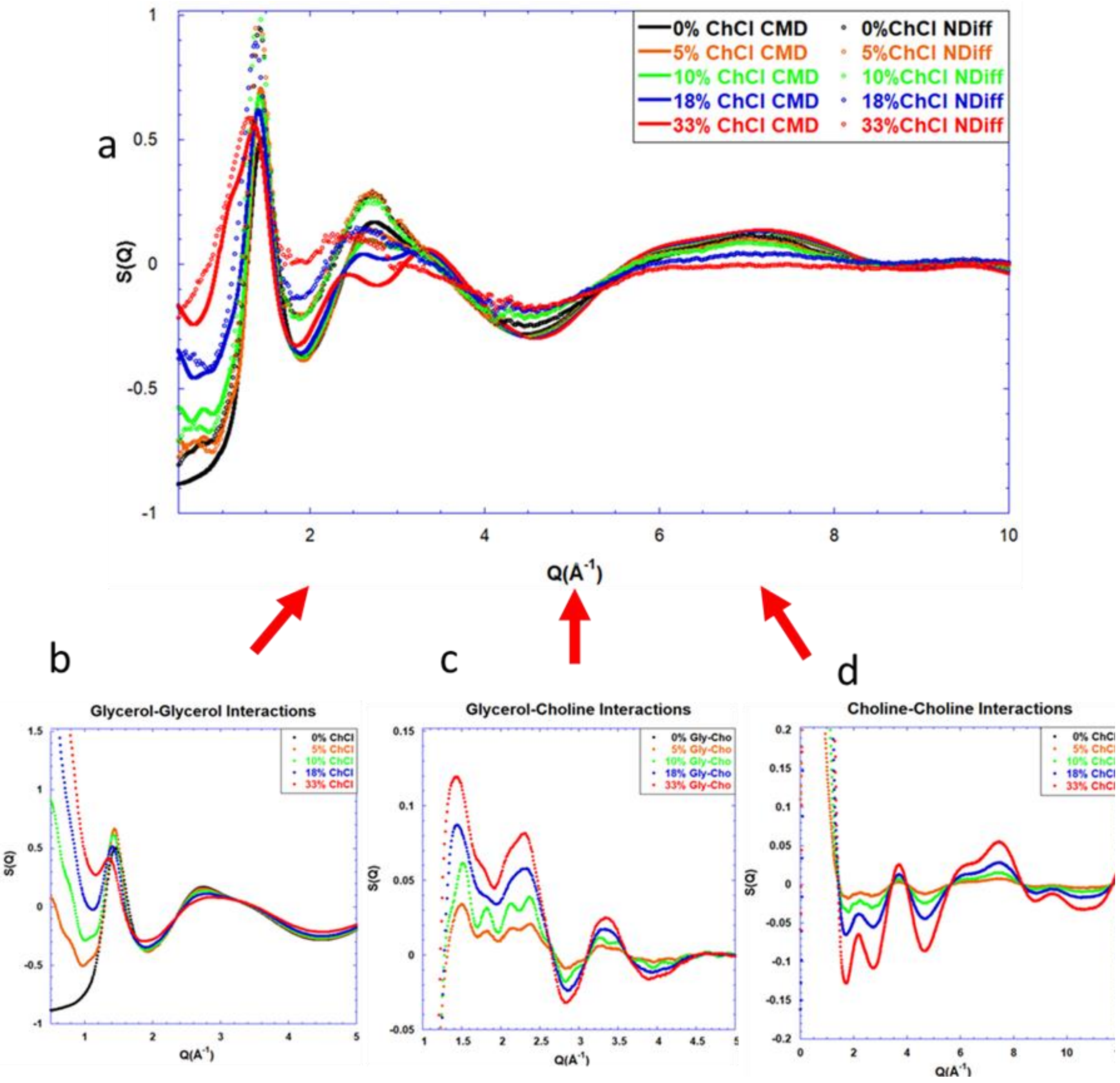

Figure IV.3 – S(Q) plots for wide-angle neutron diffraction a) compared to classical molecular dynamic simulations over a range of 0-10Å^{-1}, b) glycerol-glycerol interactions, c) glycerol-choline interactions, d) choline-choline interactions.

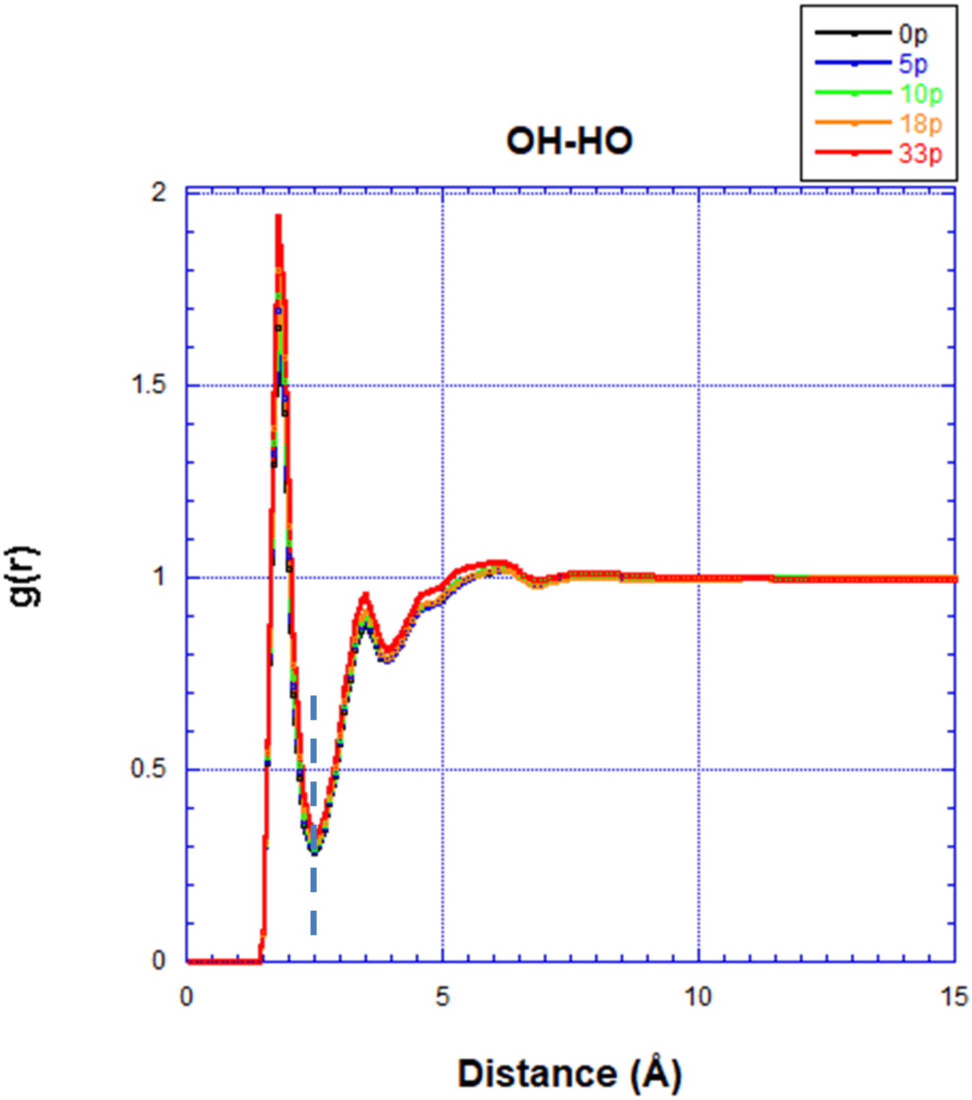

Figure IV.4 – Example of partial Radial Distribution Functions of hydrogen bond locations, as glycerol-glycerol. Dotted line indicates solvation shell location used for coordination number analysis.

where ρ_0 is the total count density, x_i and x_j are the mole fractions of atoms i and j, f is the neutron scattering length for atoms i and j, L is the simulation box length, $g_{ij}(r)$ is the radial distribution function between atoms i and j, and $W(r) = si\,n(2\pi r/L)\,/(2\pi r/L)$ is a Lorch window function to account for finite size truncation of the $g_{ij}(r)$ at large r, radius from a central particle.

This conversion provides an analysis protocol that provides the structure factor of the assemblies that emerge from classical molecular dynamics simulation that can be directly compared to the measured neutron diffraction, where $S(Q)^{sim}=S(Q)$. Therefore, the comparison of the $S(Q)^{sim}$ from the CMD calculation to the collected neutron diffraction S(Q) offers detailed insight into the structure and assembly of the hydrogen bond network that exists in the ChCl/glycerol mixtures.

Figure IV.3 shows a plot of the structure factor, S(Q), of the ChCl/glycerol mixtures as determined by both neutron diffraction (points) and classical molecular dynamics (lines), over a Q-range of 0.5 $Å^{-1}$ to 10 $Å^{-1}$. The overall trends between the ND and the CMD are consistent, especially in the 0% ChCl data set. These data show that there are 3 Q-ranges that exhibit significant changes in the structure of the glycerol hydrogen bond network with the addition of ChCl. The lowest Q-range of interest is from Q = 1.4 $Å^{-1}$ to 2 $Å^{-1}$. The peak in this region corresponds mostly to glycerol-glycerol interactions, given that the peak at 1.4$Å^{-1}$ is present in the pure glycerol sample, i.e., 0% ChCl. In both the ND and CMD data, this peak decreases in intensity and shifts to lower Q, albeit slightly more in the neutron diffraction data than the CMD simulations, with increased ChCl in the system. This demonstrates the accuracy of the CMD simulations to model the glycerol-glycerol interactions in the systems measured by neutron diffraction. The decrease in intensity demonstrates that the average amount of inter-molecular interactions between glycerol molecules decreases with increased addition of ChCl, while the shift to lower Q indicates that these molecules are moving further apart as well.

The next Q-range of interest is from Q = 2.2 $Å^{-1}$ to 3.8 $Å^{-1}$. The intensity of the peak at 2.8 $Å^{-1}$ decreases in both the ND and CMD results with addition of ChCl to the mixture. Both data sets also shift of this peak to lower Q to around Q = 2.2 $Å^{-1}$ for the 33% ChCl sample. However, there is second peak that forms at 3.4 $Å^{-1}$ with addition of the ChCl to the system in the CMD data that appears as a shoulder to the dominant peak in the neutron diffraction data. The decrease in the intensity of the peak at 2.2 $Å^{-1}$ to 2.8 $Å^{-1}$ can be correlated to the weakening of intermolecular interactions between and separation of glycerol molecules but may also correlate to the formation of new intermolecular interactions as ChCl is added to the system. The formation of the peak at 3.4 $Å^{-1}$ can almost solely be attributed to the formation of intermolecular interactions that include the ChCl, and therefore increase with the addition of ChCl to the system.

Focusing on the higher Q-range , there is a formation of a valley at 4.5 $Å^{-1}$ and a broad peak at Q = 5.5 $Å^{-1}$ to 8.3 $Å^{-1}$. The intensity measured by ND here shows a consistent decrease in intensity at both locations with almost no scattering measured at 33% ChCl from the interactions formed in the peak. However, the CMD data provides an opposite trend, where the addition of ChCl to the system increases the intensity of both this valley and this peak over the whole range. Neither ND nor CMD demonstrate a shift in this peak. The CMD simulation of the 0% ChCl does match the neutron diffraction of pure glycerol over this range of Q. Therefore, the discrepancies that are seen in higher concentrations of ChCl require validation.

To provide further insight into the specific pair interactions that contribute to each peak in the structure factors, partial S(Q) were determined by taking the Fourier transform of partial radial distribution functions (pRDF's) of specific pairs of molecules. For instance, Figure IV.4 shows the pRDF of the interactions of two -OH groups on neighboring glycerol molecules. Figures IV.3b through IV.3d show the particle structure factors of glycerol-glycerol interactions (g-g), glycerol-choline interactions (g-c), and choline-choline interactions (c-c), respectively. The g-g S(Q), Figure IV.3b, displays the peak at $Q = 1.25$ Å^{-1} that follows the ND and CMD data, exhibiting a decrease in intensity and shift to lower Q with an increase of ChCl to the system. Additionally, the intensity of the peak at 2.8 Å^{-1} decreases in intensity with addition of ChCl as is observed in the ND and CMD results. However, this peak does not shift to lower Q, nor is there a peak at 3.4 Å^{-1} with the addition of ChCl. Thus, these changes in the ND and CMD results must also be influenced by other interactions beyond glycerol-glycerol. Finally, the scattering intensity from 4 Å^{-1} to 8 Å^{-1} decreases in Figure IV.3b with addition of ChCl to the mixture, closely matching the trends found in ND data.

The partial structure factor that accounts for interactions between glycerol and choline (g-c interactions), which are presented in Figure IV.3c, show an increase in intensity in peaks that form at 1.4 Å^{-1}, accompanied by a shift to lower Q with an increase in ChCl in the system. This can be associated with the peaks, but with a smaller shift in the CMD than the ND at this position observed in total S(Q). Additionally, in

Figure IV.3c, increasing the ChCl concentration increases the absolute intensity of the peaks at 2.4 Å^{-1} and 3.4 Å^{-1}, as well as the valley at 2.8 Å^{-1}. These changes correlate to the shift in Q of the peak from 2.5 Å^{-1} to 2.2 Å^{-1} in the ND data accounting for changes in the scattering that are not observed in the g-g correlations (Figure IV.3b). The variation in the S(Q) at 3.4 Å^{-1} also corresponds to the formation of the shoulder in the ND data and the peak in the CMD results at 3.4 Å^{-1}.

Finally, the contribution of choline-choline interactions to the measured structure factor can be elucidated by examining the partial S(Q) for the c-c interaction, Figure IV.3d. In this data, there is a large peak at 3.5 Å^{-1} that clearly contributes to the peak and shoulder in the CMD and ND data in this Q region. At larger Q, the valley in S(Q) at 4.5 Å^{-1} to 5 Å^{-1} and the broad-shouldered peak at Q ~ 5.5 Å^{-1} to 8 Å^{-1} both increase in intensity with an increase in ChCl. Therefore, the c-c interactions contribute to the observed differences in the ND and CMD data in this Q regime.

Coordination Numbers

Analysis of the pRDF's of specific pair interactions allows the determination of probability of interactions between functional group pairs in the ChCl:glycerol mixtures. The extent of these interactions can be quantified by defining a coordination number of a specific pair of functional groups as the number of these pairwise interactions that can occur within the first solvation shell. The first solvation shell is defined by the minima in the RDF immediately following the first maxima, denoted as a vertical dotted line on the OH-HO pRDF plot in Figure IV.4. Insight into the assembly of the glycerol and choline molecules can be characterized by plotting the probability that a given functional group is coordinated with *n* other functional groups as a function of *n*, as is presented in Figure IV.5 for specific functional group pairs for varying choline chloride:glycerol mixture compositions. Glycerol-glycerol interactions are monitored in the first plot, Figure IV.5a, which examines the coordination of glycerol hydroxyl groups with other glycerol hydroxyl groups as the OH-HO pair. This plot shows a decrease in probability that the OH groups are coordinated to 1 (CN1) or 2 (CN2) OH groups from other glycerol molecules in the first solvation shell as more ChCl is added to the mixture. At the same time, the probability that the central glycerol hydroxyl groups do not coordinate with intermolecular OH groups (CN0) increases from 21% to 48%, with the addition of choline chloride. This plot also shows that the probability that 3 (or more) OH groups are coordinated to the central glycerol hydroxyl group is zero, indicating that no more than 3 glycerol molecules are coordinated in these mixtures and in pure glycerol.

Figure IV.5b, which monitors the probability of the hydroxyl groups on choline molecules (OY-HY) coordinating with each other as the choline loading increases. At 5% ChCl loading, there is a 78% chance that there are no Oy-Hy interactions (CN0) and only a 20% chance that they are coordinated as discrete pairs (CN1). As the loading of ChCl increases to 33%, the probability that a choline OH is not coordinated to another choline OH drops to 16%, while the probability that it coordinates with one other choline molecule (CN1) increases to 35%. At the same time, the probability that two (CN2), three (CN3), or four (CN4) of their neighboring molecules are also choline increase to 30%, 15%, and 4%, respectively. This plot therefore quantifies the extent of interactions between choline molecules as more ChCl is added to the mixture.

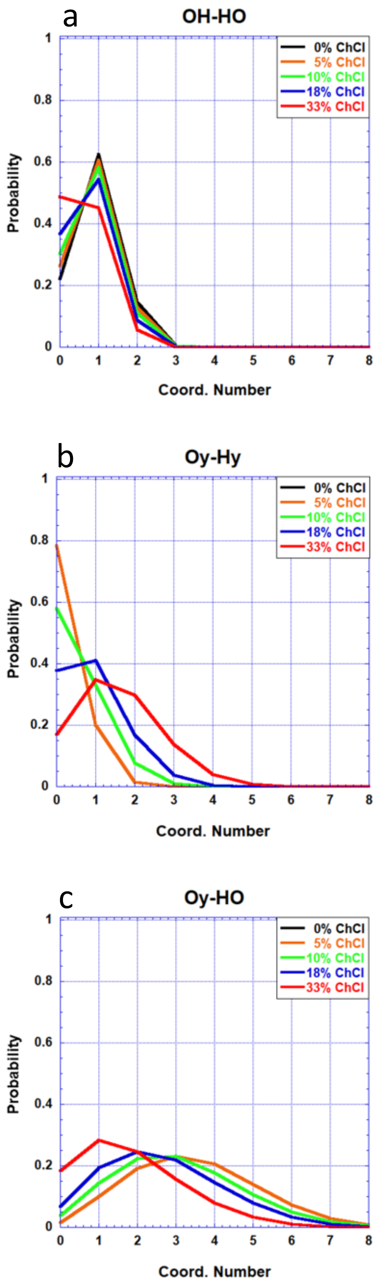

Figure IV.5 –Probabilities of hydrogen bond interactions forming as a function of coordination number for varying mixture compositions, a) glycerol-glycerol as OH-HO bonds, b) choline-choline as Oy-Hy bonds, and c) choline-glycerol as Oy-HO bonds.

Figure IV.5c, presents the probability of forming glycerol-choline interactions between their hydroxyl groups (Oy-HO). At 5% ChCl:glycerol, the coordination with the highest probability (22%) has three glycerol molecules coordinating with the central choline. As more ChCl is added to the system, this optimum coordination number shifts to fewer groups interacting, where for 33% ChCl:glycerol system, the most common assembly has each choline only coordinated to one glycerol (CN1). Additionally, as the ChCl loading increases, the probability of the assembly with the most probable CN increases from 22% to 30%. This indicates that the choline is more likely to form interactions with fewer glycerol molecules as more choline is added to the system, suggesting that the choline hydroxyl group is not driving the disruption of the glycerol hydrogen bonding network.

Spatial Distribution Functions

The coordination of the glycerol, choline, and chloride vary significantly as the amount of ChCl in the mixture increases. To visualize these changes, spatial distribution functions (SDF's) were created to illustrate how these interactions assemble in 3 dimensions. Figure IV.6 shows the SDF around a choline molecule as a three-dimensional density distribution map. The illustration shows the distribution of a neighboring molecule (glycerol, choline, or chloride) around the central molecule. In Figure IV.6, as the amount of choline chloride increases, the sites of interaction between the choline and the neighboring molecules do not shift in position, but the amount of interaction changes. As more ChCl is added to the system, the amount of area occupied by choline (red) increases, corresponding to more available choline. The most

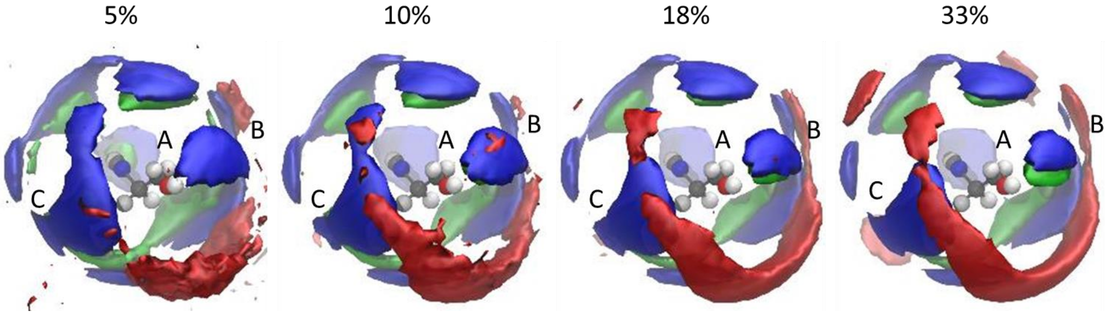

Figure IV.6 – Choline centric spatial distribution functions. Choline-red, chloride-green, and glycerol-blue.

significant changes in these distributions with addition of choline to the system are at the sites marked A, B, and C. At all of these locations, the amount of chloride (green) present decreases as more ChCl is added to the system. At sites B and C, the amount of glycerol (blue) also noticeably diminishes. These changes indicate that the chloride and glycerol are interacting less with the choline and choline-choline interactions are more likely than choline-glycerol or choline-chloride.

Figure IV.7 presents the SDF's of the first solvation shell of a central glycerol molecule with varying choline chloride compositions. As in Figure IV.6, locations of the interacting molecules with the central glycerol molecule do not change as the ChCl concentration increases from 5% to 33%. The SDF's do show however that chloride occupies the volume near the glycerol methylene groups (Hg) in the central glycerol molecule. Figure IV.7 demonstrates that the chloride occupies the volume closest to the central glycerol molecule and tends to be sandwiched between two glycerol molecules, interrupting their hydrogen bonding network.

Network Formation Probabilities

We are interested in understanding the change in assembly and structure of the hydrogen bonding networks that exist in the ChCl/glycerol mixtures as a function of the mixture composition. Thus, understanding the connectivity of the molecules becomes important. Therefore, the probabilities of a coordination number occurring for specific functional group pairs as a function of ChCl compositions were calculated and plotted in Figure IV.8. In Figure IV.8a, the change in the probability of coordination of a glycerol hydroxyl group (OH) with the glycerol methylene group (Hg) decreases with increased

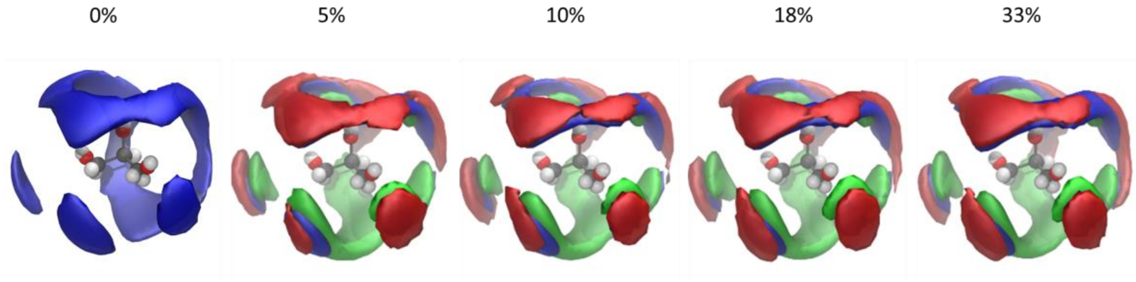

Figure IV.7 – Glycerol centric spatial distribution functions. Choline-red, chloride-green, and glycerol-blue.

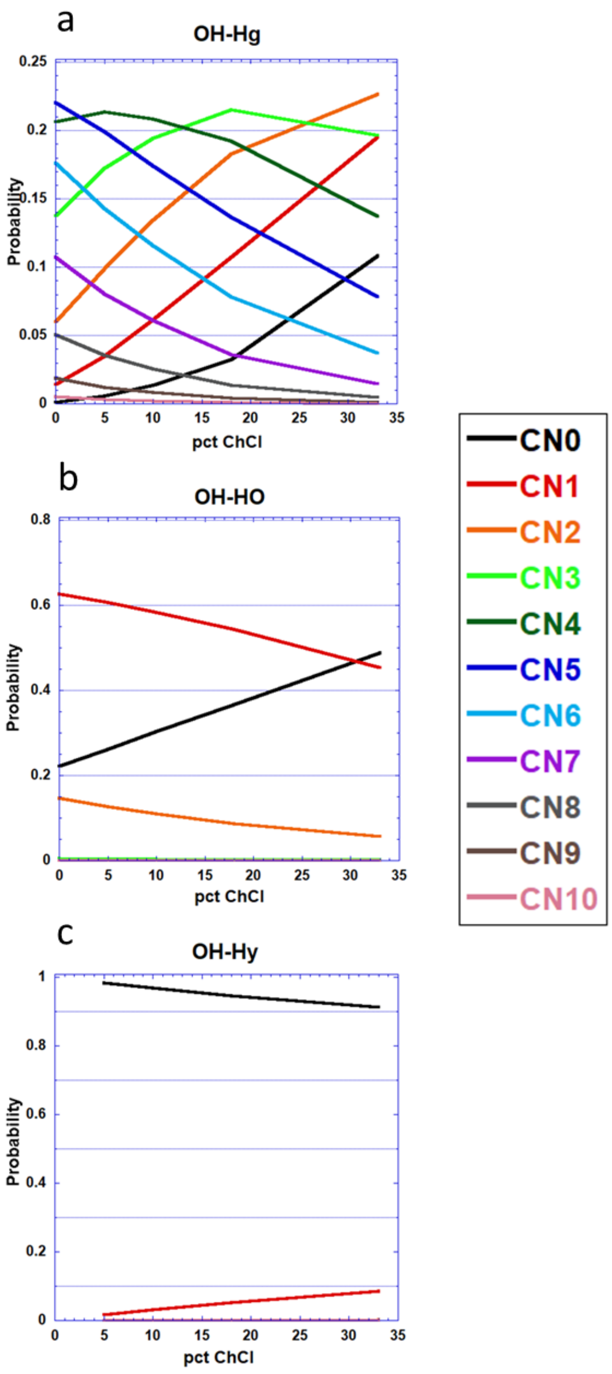

Figure IV.8 –Probabilities of coordination numbers existing at specific mixture compositions for specific functional group pairs a)glycerol hydroxyl-glycerol methylene groups, b) glycerol hydroxyl-glycerol hydroxyl groups, and c) glycerol hydroxyl-choline hydroxyl groups.

ChCl loading. Closer inspection shows that the maximum correlation number is 4 at 5% ChCl, is 3 at 18% ChCl, and is 2 in the eutectic composition of 33%. Moreover, throughout, the number of single connections (CN1) or individual (CN0) glycerol molecules increases as the percentage of ChCl increases. At 33% ChCl:glycerol, there is a 23% probability that a glycerol is only connected to 2 other glycerol molecules. This clearly shows that the glycerol hydrogen bonding network is disrupted or loosened as more ChCl is added to the mixture.

Figure IV.8b displays this same plot for the intermolecular glycerol hydroxyl groups (OH-HO). In pure glycerol the probability that 2 hydroxyl groups (CN1) are interacting is 62% and the probability that 3 groups (CN2) interact is 12%, while having a solitary glycerol hydroxyl (CN0) is 22%. These probabilities steadily change with the addition of ChCl to the mixture. The probability of CN0 increases to 49%, while both CN1 and CN2 decrease to 45% and 6%, respectively. This is another clear indication that fewer glycerol molecules are interacting and forming hydrogen bonds. The final plot that illustrates how the glycerol hydroxyl is interacting with neighboring molecules, Figure IV.8c, shows that the glycerol hydroxyl group (OH) and the choline hydroxyl group (Hy) interaction is only dependent on the composition of the mixture, where the singly coordinations (CN1) and the non-coordinations (CN0) scale linearly with the amount of choline chloride in the mixture.

Figure IV.9a elucidates how the choline hydroxyl groups (Oy) interact with other choline hydroxyl groups (Hy) and shows increased interactions between these groups with added choline chloride. Over this concentration range, the number of molecules

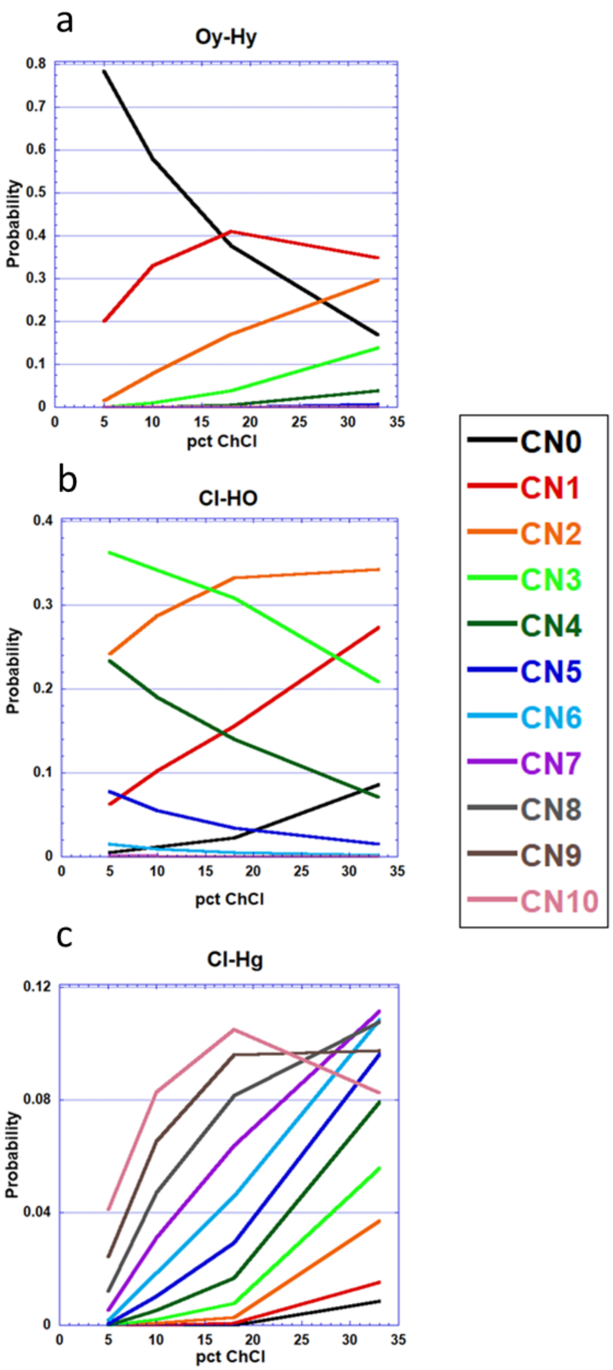

Figure IV.9–Probabilities of coordination numbers existing as a function of mixture composition for a)choline hydroxyl-choline hydroxyl groups, b)chloride-glycerol hydroxyl groups, and c)chloride-glycerol methylene groups.

that are not coordinated with other choline molecules (CN0) steadily decreases with increased choline chloride from 78% to 17%. At the same time, assemblies with higher number of molecules coordinating (CN2, CN3, and CN4) steadily increase. Figure IV.10 shows choline centric interactions of choline and glycerol molecules. These figures show that interactions of the choline chloride hydroxyl groups (Oy) with both the glycerol methylene groups (Hg), Figure IV.10a, and hydroxyl (HO), Figure IV.10b, decrease as more choline chloride is added to the system. The presence of more interactions at 5% ChCl (19% CN5 for Oy-Hg and 23% CN3 for Oy-HO) can be attributed to the small amount of choline in the mixture that is surrounded with glycerol. However, as more ChCl is added to the system these interactions shift to primarily small amounts of single (CN1) and double (CN2) coordinated groups. Since both glycerol and choline have hydroxyl groups that are available to form hydrogen bonds, these interactions could increase with more choline added to the system if the choline was interrupting the glycerol hydrogen bonded network.

The coordination of chloride (Cl) and the glycerol hydroxyl group (HO) are monitored in Figure IV.9b. As the amount of ChCl in the mixture increases, more assemblies with fewer coordinations between the Cl and the glycerol hydroxyl form. This indicates, that while the addition of Cl forms more connections with the glycerol, these connections remain between one or two glycerol molecules, but higher connectivity is not formed. Meanwhile, the chloride and glycerol methylene groups (Hg) have formed a large assembly of interactions, Figure IV.9c, which is consistent with the SDF in Figure IV.7. Examination of this figure shows that the number of coordinated groups is always seven or greater, with a peak of ten coordinated groups

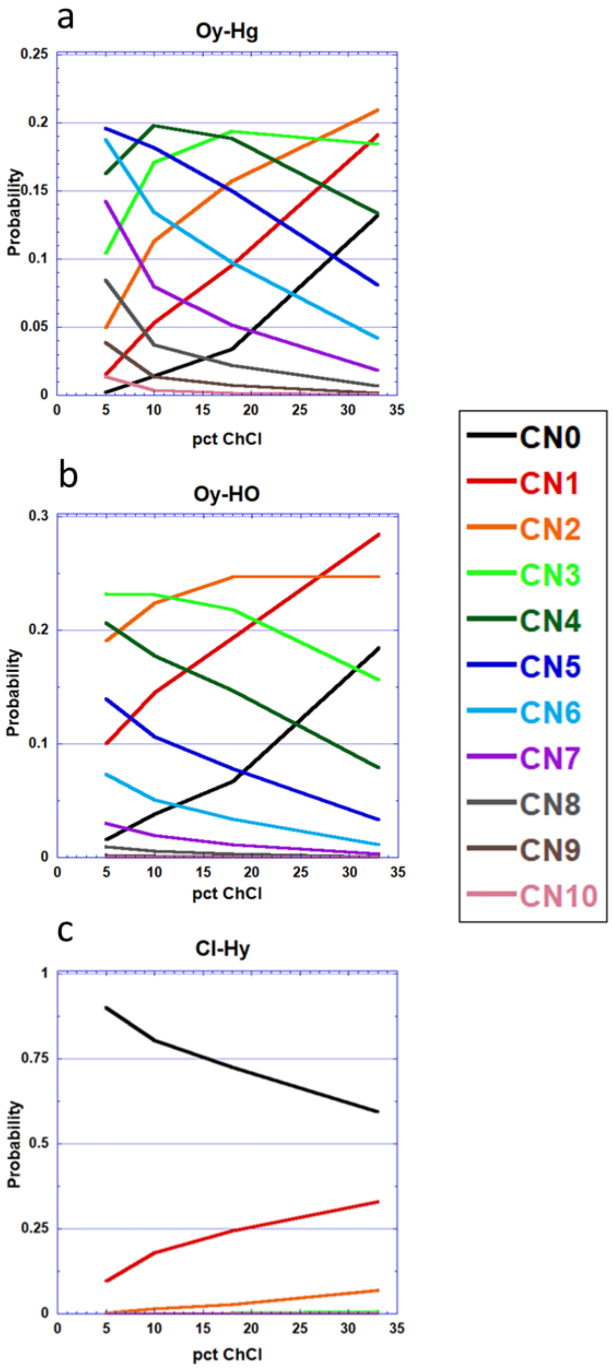

Figure IV.10 –Probabilities of coordination numbers existing as a function of mixture composition for a)choline hydroxyl-glycerol hydroxyl groups, b) choline hydroxyl-glycerol methylene groups, and c)chloride- choline hydroxyl groups.

(CN10) at 18% ChCl and greater than 10% probability of six, seven, and eight coordinated groups at 33% ChCl. This suggests that the chloride is highly coordinated with the glycerol methylene groups. Finally, the interactions of the chloride atoms with the choline hydroxyl groups (Hy) are shown in Figure IV.10c. Here the number of pairwise interactions (CN1) scale with the amount of ChCl in the system, suggesting limited interactions between these groups are forming. The probability of no interactions between Cl and Hy decreases slightly from 90% at 5% ChCl to 60% at 33% ChCl but remains the most likely scenario. This suggests that the chloride and choline separate in these mixtures allowing the chloride to be available to coordinate with the glycerol while the choline becomes available to coordinate with other choline molecules.

Discussion

Wide angle neutron scattering data and the CMD results show a strong agreement in the behavior of the measured mixtures of ChCl:glycerol. The computationally determined peaks formed by the g-g interactions agree with the diffraction data. However, computationally determined peaks that emerge from g-c interactions are less apparent in the neutron data, while interactions between c-c are less well observed. This becomes apparent as partial S(Q) were computationally determined and show that the largest deviations between the diffraction data and the CMD simulations were dominated by interactions between choline-choline.

While the d8-glycerol used is fully deuterated, meaning all the hydrogen has been replaced with deuterium, the d9-choline has only the aliphatic methyl groups deuterated. Therefore, potential hydrogen bonding groups of the glycerol are all deuterated, while the potential hydrogen bonding groups of choline are the protonated hydroxyl groups. This leads to the experimental result where the correlations between deuterated glycerol hydroxyl and deuterated glycerol hydroxyl contribute more significantly in neutron diffraction than the protonated-deuterated or protonated-protonated correlations of choline hydroxyl-glycerol hydroxyl and choline hydroxyl-choline hydroxyl, respectively. Allowing for this deviation, the CMD simulations present a reasonable model of the structure of the mixtures of ChCl/glycerol and their neutron diffraction data.

The position shifts and intensity changes of the peaks in the S(Q) indicate that the addition of ChCl to glycerol decreases the glycerol-glycerol peaks and increases the peaks that track interactions between choline-choline and glycerol-chloride. These peak changes are a result of the structure of the changing glycerol hydrogen bond network. Careful analysis of the population of the coordination shells of the mixture components shows that the chloride plays an important role in disrupting the glycerol hydrogen bonds. Focusing on the coordination shell of the choline hydroxyl shows increasing coordination between neighboring choline hydroxyl groups, suggesting that the cholines tend to form small clusters rather than participate in the glycerol hydrogen bonding network.

The evolution of the glycerol hydrogen bonding network with the addition of more choline chloride indicates that the chloride ions assemble near the glycerol methylene groups and form pair-wise interactions with the glycerol hydroxyl groups. Monitoring the structure of the interactions of the glycerol hydroxyl groups with other glycerol hydroxyl groups indicates that, as ChCl is added to the mixture, the probability of a forming multiple coordinations between glycerol molecules decreases accompanied by an increase of non-interacting glycerol hydroxyl groups (CN0), which increases from 22% to 50%. This is consistent with the loss of glycerol-glycerol hydrogen bonds and a loosening of the hydrogen bonding network.

This interpretation is supported by the distribution of the glycerol, choline, and chloride that is observed in the SDF's, Figures IV.6 and IV.7. In these figures, the proximity of the Cl and glycerol to the choline decreases as more ChCl is added to the system, driving an assembly where the choline molecules tend to hydrogen bond with other choline molecules. This assembly of the choline molecules combined with the fact that the Cl aggregates near the glycerol in these SDF's, suggests that the chloride is available to interact with glycerol molecules and disrupts the glycerol hydrogen bond network. This is evidenced by a decrease in glycerol-glycerol interactions with the addition of ChCl to the system but with few interactions between the glycerol hydroxyl groups and chloride, suggesting that the chloride doesn't completely interrupt the glycerol-glycerol interactions. The data also show that the chloride tends to aggregate near glycerol methylene groups and remain well coordinated in all the mixture compositions.

The number of interactions between functional groups provides insight into the success of hydrogen bond network formation, where multiple coordinations (> 3) can serve as a node in a network, while 2 coordination can serve as a linear connection, and pairwise or no coordinations results in domains that are isolated from a network. Examination of Figures IV.8 shows that the probability of a glycerol hydroxyl interacting with another glycerol hydroxyl steadily decreases as choline chloride are added, showing the significant loosening, and potential disrupting of the glycerol hydrogen bonding network at the 33% ChCl mixture. The dominance of pairwise interaction (CN1) in the glycerol-glycerol interactions indicates the limited connectivity of the hydrogen bonding network as the amount of choline chloride increases in the mixture. in the deep eutectic solvent, Glyceline. Finally, at the 33% ChCl mixture, an isolated glycerol hydroxyl (CN0) is the most common structure with a 49% probability, suggested significant interruption in the glycerol hydrogen bonded network at the formation of the deep eutectic solvent, 33% ChCl. The formation of chloride-glycerol hydroxyl intermolecular interactions are also apparent in Figure IV.9b, an indication that a chloride contributes to breaking up the hydrogen bonding network of the glycerol.

It is interesting that the chloride ion plays an important role in disrupting the glycerol hydrogen bonded network in the formation of the deep eutectic solvent, while the choline is not. This would imply that the choice of counter anion will play an important role in the formation of a deep eutectic solvent. This leads to the prediction that the formation of deep eutectic solvents with glycerol and choline bromide, glycerol and choline fluoride, or glycerol with choline iodide would exhibit significantly different phase behavior than Glyceline and may not form a deep eutectic solvent at all. Preliminary results by collaborators show that the choice of anion can dramatically impact the phase behavior of deep eutectic solvents.

Conclusions

The structure of the ChCl:glycerol mixture has been monitored for changes as the amount of choline chloride increases up to the established eutectic point of Glyceline at

33% ChCl:glycerol. Structural information from CMD simulations and neutron diffraction of the choline chloride: glycerol mixtures with varying compositions offer insight into the specific local interactions that emerge as ChCl is added to the system. Evolutions in neutron diffraction structure factors are observed for deuterated components, especially d8-glycerol interactions, whereas CMD demonstrates that the changes between non-deuterated hydroxyl groups in d9-choline are still accounted for in the structural analysis. These results show that as ChCl is added to glycerol, the chloride ions assemble with the glycerol, while the choline molecules do not significantly participate in the glycerol hydrogen bonding network. The assembly of the chloride ions near the glycerol loosens the interactions between glycerol molecules, thereby disrupting the glycerol hydrogen bond network. The limited role of choline molecules in disrupting the glycerol hydrogen bond network is somewhat surprising as both choline and glycerol have hydroxyl groups that are available for hydrogen bonding. Rather the choline appears to segregate from both the glycerol and chloride forming hydrogen bonds in small pockets with other choline groups as ChCl is added to the glycerol. This results in the availability of the chloride to interact with the glycerol.

Acknowledgements

This work was supported as part of the Breakthrough Electrolytes for Energy Storage (BEES), an Energy Frontier Research Center funded by the U.S. Department of Energy, Office of Science, Basic Energy Sciences under Award# DE-SC0019409. A portion of this research used resources at the Spallation Neutron Source, a DOE Office of Science User Facility operated by the Oak Ridge National Laboratory.

References

1. Abbott, A. P.; Capper, G.; Davies, D. L.; Munro, H. L.; Rasheed, R. K.; Tambyrajah, V., Preparation of novel, moisture-stable, Lewis-acidic ionic liquids containing quaternary ammonium salts with functional side chains. Chemical Communications 2001, (19), 2010-2011.

2. Niedermeyer, H.; Hallett, J. P.; Villar-Garcia, I. J.; Hunt, P. A.; Welton, T., Mixtures of ionic liquids. Chemical Society Reviews 2012, 41 (23), 7780-7802.

3. Abbott, A. P.; Boothby, D.; Capper, G.; Davies, D. L.; Rasheed, R. K., Deep eutectic solvents formed between choline chloride and carboxylic acids: Versatile alternatives to ionic liquids. Journal of the American Chemical Society 2004, 126 (29), 9142-9147.

4. Abbott, A. P.; Capper, G.; Davies, D. L.; Rasheed, R. K.; Tambyrajah, V., Novel solvent properties of choline chloride/urea mixtures. Chemical Communications 2003, (1), 70-71.

5. Hansen, B. B.; Spittle, S.; Chen, B.; Poe, D.; Zhang, Y.; Klein, J. M.; Horton, A.; Adhikari, L.; Zelovich, T.; Doherty, B. W.; Gurkan, B.; Maginn, E. J.; Ragauskas, A.; Dadmun, M.; Zawodzinski, T. A.; Baker, G. A.; Tuckerman, M. E.; Savinell, R. F.; Sangoro, J. R., "Deep Eutectic Solvents: A Review of Fundamentals and Applications", Chemical Review, 2020.

6. Hammond, O. S.; Bowron, D. T.; Edler, K. J., Liquid structure of the choline chloride-urea deep eutectic solvent (reline) from neutron diffraction and atomistic modelling. Green Chemistry 2016, 18 (9), 2736-2744.

7. Hammond, O. S.; Bowron, D. T.; Jackson, A. J.; Arnold, T.; Sanchez-Fernandez, A.; Tsapatsaris, N.; Sakai, V. G.; Edler, K. J., Resilience of Malic Acid Natural Deep Eutectic Solvent Nanostructure to

8. Smith, E. L.; Abbott, A. P.; Ryder, K. S., Deep Eutectic Solvents (DESs) and Their Applications. Chemical Reviews 2014, 114 (21), 11060-11082.

9. Karimi, M.; Eshraghi, M. J., One-pot and green synthesis of Mn3O4 nanoparticles using an all-in-one system (solvent, reactant and template) based on ethaline deep eutectic solvent. Journal of Alloys and Compounds 2017, 696, 171-176.

10. Shekaari, H.; Zafarani-Moattar, M. T.; Shayanfar, A.; Mokhtarpour, M., Effect of choline chloride/ethylene glycol or glycerol as deep eutectic solvents on the solubility and thermodynamic properties of acetaminophen. Journal of Molecular Liquids 2018, 249, 1222-1235.

11. Yadav, A.; Kar, J. R.; Verma, M.; Naqvi, S.; Pandey, S., Densities of aqueous mixtures of (choline chloride plus ethylene glycol) and (choline chloride plus malonic acid) deep eutectic solvents in temperature range 283.15-363.15 K. Thermochimica Acta 2015, 600, 95-101.

12. Alanon, M. E.; Ivanovic, M.; Gomez-Caravaca, A. M.; Arraez-Roman, D.; Segura-Carretero, A., Choline chloride derivative-based deep eutectic liquids as novel green alternative solvents for extraction of phenolic compounds from olive leaf. Arabian Journal of Chemistry 2020, 13 (1), 1685-1701.

13. Bryant, S. J.; Atkin, R.; Warr, G. G., Effect of Deep Eutectic Solvent Nanostructure on Phospholipid Bilayer Phases. Langmuir 2017, 33 (27), 6878-6884.

14. Garcia, G.; Aparicio, S.; Ullah, R.; Atilhan, M., Deep Eutectic Solvents: Physicochemical Properties and Gas Separation Applications. Energy & Fuels 2015, 29 (4), 2616-2644.

15. Hou, Y. C.; Yao, C. F.; Wu, W. Z., Deep Eutectic Solvents: Green Solvents for Separation Applications. Acta Physico-Chimica Sinica 2018, 34 (8), 873-885.

16. Tome, L. I. N.; Baiao, V.; da Silva, W.; Brett, C. M. A., Deep eutectic solvents for the production and application of new materials. Applied Materials Today 2018, 10, 30-50.

17. Li, C. C.; Huang, C. X.; Zhao, Y.; Zheng, C. J.; Su, H. X.; Zhang, L. Y.; Luo, W. R.; Zhao, H.; Wang, S. F.; Huang, L. J., Effect of Choline-Based Deep Eutectic Solvent Pretreatment on the Structure of Cellulose and Lignin in Bagasse. Processes 2021, 9 (2).

18. Nishani K Jayakody, Carla C. Fraenza, Steven G. Greenbaum, David S. Ashby, and Bruce S. Dunn, "NMR Relaxometry and Diffusometry Analysis of Dynamics in Ionic Liquids and Ionogels for Use in Lithium Ion Batteries" Journal of Physical Chemistry B, 2020.

19. Burcu Gurkan, Henry Squire, and Emily Pentzer, "Metal-Free Deep Eutectic Solvents: Preparation, Physical Properties, and Significance", The Journal of Physical Chemistry Letters 2019 10 (24), 7956-7964

20. Celebi, A. T.; Vlugt, T. J. H.; Moultos, O. A., Structural, Thermodynamic, and Transport Properties of Aqueous Reline and Ethaline Solutions from Molecular Dynamics Simulations. Journal of Physical Chemistry B 2019, 123 (51), 11014-11025.

21. D'Agostino, C.; Harris, R. C.; Abbott, A. P.; Gladden, L. F.; Mantle, M. D., Molecular motion and ion diffusion in choline chloride based deep eutectic solvents studied by H-1 pulsed field gradient NMR spectroscopy. Physical Chemistry Chemical Physics 2011, 13 (48), 21383-21391.

22. Towey, J. J.; Soper, A. K.; Dougan, L., The structure of glycerol in the liquid state: a neutron diffraction study. Physical Chemistry Chemical Physics 2011, 13 (20), 9397-9406.

23. Yadav, A.; Pandey, S., Densities and Viscosities of (Choline Chloride plus Urea) Deep Eutectic Solvent and Its Aqueous Mixtures in the Temperature Range 293.15 K to 363.15 K. Journal of Chemical and Engineering Data 2014, 59 (7), 2221-2229.

24. Yadav, A.; Trivedi, S.; Rai, R.; Pandey, S., Densities and dynamic viscosities of (choline chloride plus glycerol) deep eutectic solvent and its aqueous mixtures in the temperature range (283.15-363.15) K. Fluid Phase Equilibria 2014, 367, 135-142.

25. Kaur, S.; Gupta, A.; Kashyap, H. K., How Hydration Affects the Microscopic Structural Morphology in a Deep Eutectic Solvent. Journal of Physical Chemistry B 2020, 124 (11), 2230-2237.

26. Abbott, A. P.; D'Agostino, C.; Davis, S. J.; Gladden, L. F.; Mantle, M. D., Do group 1 metal salts form deep eutectic solvents? Physical Chemistry Chemical Physics 2016, 18 (36), 25528-25537.

27. William Dean, Jeffrey Klein and Burcu Gurkan, "Do Deep Eutectic Solvents Behave Like Ionic Liquid Electrolytes? A Perspective from the Electrode-Electrolyte Interface2" Journal of The Electrochemical Society, 2021.

28. Francisco, M.; van den Bruinhorst, A.; Kroon, M. C., Low-Transition-Temperature Mixtures (LTTMs): A New Generation of Designer Solvents. Angewandte Chemie-International Edition 2013, 52 (11), 3074-3085.

29. Faraone, A.; Wagel, D. V.; Baker, G. A.; Novak, E. C.; Ohl, M.; Reuter, D.; Lunkenheimer, P.; Loidl, A.; Mamontov, E., Glycerol Hydrogen-Bonding Network Dominates Structure and Collective Dynamics in a Deep Eutectic Solvent. Journal of Physical Chemistry B 2018, 122 (3), 1261-1267.

30. Wagle, D. V.; Baker, G. A.; Mamontov, E., Differential Microscopic Mobility of Components within a Deep Eutectic Solvent. Journal of Physical Chemistry Letters 2015, 6 (15), 2924-2928.

31. Hammond, O. S.; Bowron, D. T.; Edler, K. J., The Effect of Water upon Deep Eutectic Solvent Nanostructure: An Unusual Transition from Ionic Mixture to Aqueous Solution. Angewandte Chemie-International Edition 2017, 56 (33), 9782-9785.

32. Zhang, Y.; Poe, D.; Heroux, L.; Squire, H.; Doherty, B. W.; Long, Z. R.; Dadmun, M.; Gurkan, B.; Tuckerman, M. E.; Maginn, E. J., Liquid Structure and Transport Properties of the Deep Eutectic Solvent Ethaline Published as part of The Journal of Physical Chemistry virtual special issue "Deep Eutectic Solvents". Journal of Physical Chemistry B 2020, 124 (25), 5251-5264.

33. Turner, A. H.; Holbrey, J. D., Investigation of glycerol hydrogen-bonding networks in choline chloride/glycerol eutectic-forming liquids using neutron diffraction. Physical Chemistry Chemical Physics 2019, 21 (39), 21782-21789.

34. Neuefeind, J.; Feygenson, M.; Carruth, J.; Hoffmann, R.; Chipley, K. K., The Nanoscale Ordered MAterials Diffractometer NOMAD at the Spallation Neutron Source SNS. Nuclear Instruments & Methods in Physics Research Section B-Beam Interactions with Materials and Atoms 2012, 287, 68-75.

35. McDonnell, M.T.; Olds, D.P.; Page, K.L.; Neufeind, J.C.;. Tucker, M.G.; Bilheux, J.C.; Zhou, W.; Peterson, P.F.; ADDIE: ADvanced DIffraction Environment – a software environment for analyzing neutron diffraction data. Acta Cryst. 2017. A73, a377

36. Plimpton , S. Short-Range Molecular Dynamics. Journal of Computational Physics 1995, 117, 1 – 42.

37. Wang, J.; Wolf, R. M.; Caldwell, J. W.; Kollman, P. A.; Case, D. A. Development and Testing of a General Amber Force Field. Journal of Computational Chemistry 2004, 25, 1157–1174.

38. Frisch, M. J. *et al*. Gaussian 09 Revision A.1. Gaussian Inc. Wallingford CT 2009.

39. Perkins, S. L.; Painter, P.; Colina, C. M. Experimental and Computational Studies of Choline Chloride-Based Deep Eutectic Solvents. Journal of Chemical & Engineering Data 2014, 59, 3652–3662

40. Martínez, J. M.; Martínez, L. Packing optimization for automated generation of complex system's initial configurations for molecular dynamics and docking. Journal of Computational Chemistry 2003, 24, 819–825.

41. Martínez, L.; Andrade, R.; Birgin, E. G.; Martínez, J. M. PACKMOL: A package for building initial configurations for molecular dynamics simulations. Journal of Computational Chemistry 2009, 30, 2157–2164.

Chapter V The Atomic Vibration Effect on Dynamical Bragg Diffraction in Si Crystals

Abstract

The effect of atomic vibration on the first eight orders of dynamical Bragg reflection from $Si(220)$ triple-bounce crystals at ambient temperature has been studied theoretically and experimentally. The Bragg-peak reflectivity at a given order is considered in our theoretical model as a product of the Darwin plateau width and the reflectivity at exact Bragg angle. The results of modeling calculations are probed at the world's first multi-wavelength double crystal diffractometer launched at the pulsed Spallation Neutron Source (SNS). The pulsed structure of neutron beam at SNS allows implementation of the time-of-flight technique in dynamical diffraction experiments offering an opportunity of conducting spectroscopic tests, in addition to conventional rocking curve measurements. The results of this research show strong effects of the atomic vibration at the high orders of Bragg reflection from $Si(220)$, decreasing the Darwin plateau width by a factor of ~ 6 and the Bragg-peak reflectivity by a factor of ~ 5 at the eighth order. The effect on the Darwin plateau is valuable from a practical point of view because of the significant angular resolution increase, which can be controlled not only by changing the order of Bragg reflection but also by variation of temperature. Therefore, the results of this startup research can lead to the development of a new class of temperature-controlled X-ray and neutron optical devices utilizing single crystals, the angular resolution of which can be improved by heating.

Introduction

In spite of the fact that dynamical diffraction can be experimentally observed only on large, nearly perfect Si and Ge crystals, this technique found an important application in neutron interferometry[1] and ultra-small-angle neutron scattering (USANS).[2] The Bonse-Hart USANS instrument extends the Q-range of a conventional high-resolution small-angle neutron scattering (SANS) machine to smaller $Q's$ by two orders of magnitude offering an opportunity to observe micron-size structural inhomogeneities. Here $Q = \frac{4\pi\theta}{\lambda}$ is the length of the scattering vector, θ is the diffraction angle where $\theta \approx sin(\theta)$, and λ is the wavelength. The combined USANS/SANS technique launches studies of hierarchical structures common in materials, Earth, energy and environmental sciences.[3] Nowadays, Bonse-Hart USANS instruments are routinely available at major neutron scattering facilities worldwide and the International Consortium on USANS coordinates progress in this scientific field.[4] Growing interest in the Bonse-Hart USANS technique has stimulated further developments and an advanced multi-wavelength (MW-USANS) instrument has recently been constructed at the Spallation Neutron Source, USA. Further theoretical studies of the multi-wavelength concept and preliminary tests of the MW-USANS apparatus reveal an interesting anomalous effect of atomic vibration on the high orders of Bragg reflection.[5] According to calculations based on classical dynamical diffraction theories, thermal vibration of the crystallographic lattice increases the instrument's angular resolution. It is remarkable, because the atomic vibration decreases the Bragg-peak reflectivity of crystals operating in the kinematic regime which is a parasitic effect. This study is focused on the effect of atomic vibration at ambient temperature on the dynamical Bragg diffraction from $Si(220)$ crystals.

Theoretical Background

The dynamical Bragg diffraction is usually described in terms of the Darwin and Ewald reflectivity functions Equations 5.1, 5.2, and 5.3, which are identical for $|y| \leq 1$ but differ in the range of wings $|y| > 1$

$R(y)_{D,E} = 1, |y| \leq 1$ Equation 5.1

$R(y)_D = [|y| - (y^2 - 1)^{0.5}]^2, |y| > 1$ Equation 5.2

$R(y)_E = 1 - (1 - y^{-2})^{0.5}, |y| > 1$ Equation 5.3

Here $y = \frac{|\theta - \theta_B|}{\delta\theta}$ is the reduced angular parameter and $\delta\theta$ is the half-width of the Darwin Plateau (DP). Equation 5.1 corresponds to the Darwin-Ewald range and Equations 5.2 and 5.3 describe Darwin and Ewald solution of the wings range correspondingly. The full DP width is defined as Equation 5.4, where, $n = 1, 2, 3, \ldots$ is the order of Bragg reflection, λ_n is the corresponding wavelength, $|F(h,k,l)|$ is the

$2\delta\theta_n = 2\left[\frac{|F(h,k,l)|}{\pi V_0 \sin(2\theta_B)}\right][b_c \exp\{-W_n\}\lambda_n^2] = 2\delta\theta_n^* exp\{-W_n\}$ Equation 5.4

magnitude of the geometrical structure factor, V_0 is the unit cell volume, θ_B is the Bragg angle, b_c is the bound nuclear coherent scattering length and $exp\{-W_n\}$ is the Debye-Waller factor (DWF). The exponent $W_n = B[\frac{sin\theta_B}{\lambda_n}]^2$, where $B = 8\pi^2 u^2$ and u is the atomic root-mean-square displacement perpendicular to the Bragg plane.[6] The $2\delta\theta_n^*$ is the DP width of an “artificial crystal” free of atomic vibrations. Figure V.1 shows the $R(y)_E$ Ewald reflectivity function in the range $-3 \leq y \leq 3$ and the triple Bragg reflected $R(y)_E^3$, which is consistent with the design of $Si(220)$ triple-bounce crystals under study.

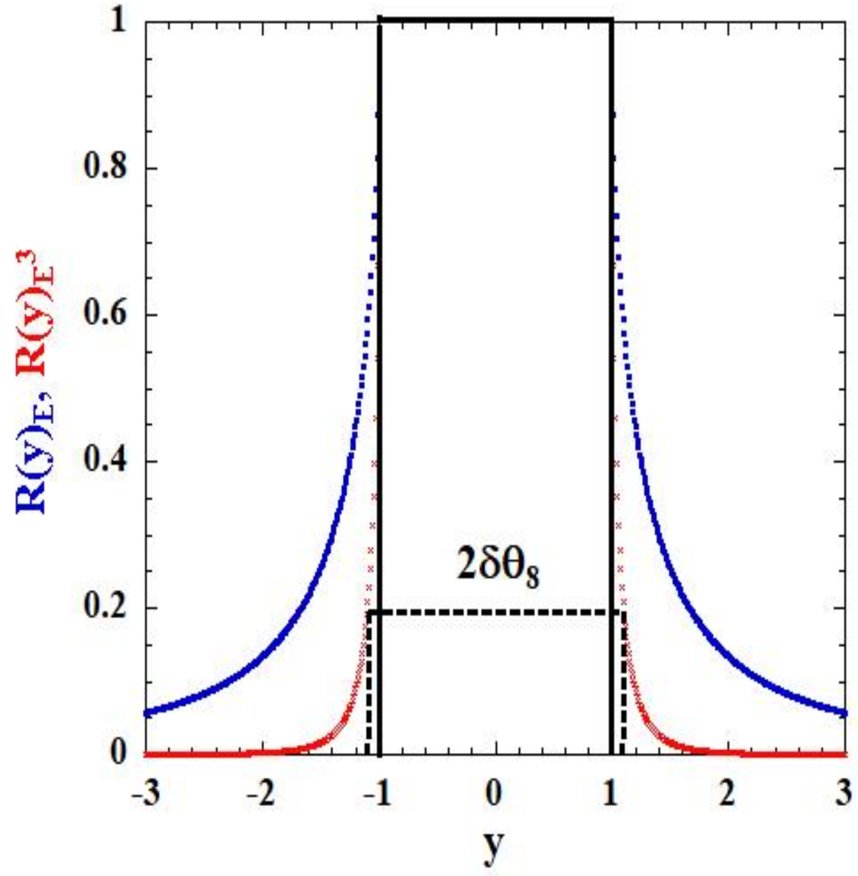

Figure V.1 - The Ewald functions $R(y)_E$ (blue squares) and $R(y)_E^3$ (red crosses); the black solid lines show the Bragg-peak area for $R(y)_E^3 = 1$ and the black dashed lines that for $R(y)_E^3 = \ 0.2$. The $2\delta\theta_8$ is the DP width at $n = 8$.

The Bragg-peak in this theoretical model is defined in Equation 5.5 as a part of $R(y)_E^3$ confined in the range $|y| \leq 1$ where the reflectivity $R(y)_E^3$ equals the unity. Here

$$I(y)_{peak,n} = \int_{-1}^{+1} R(y)_E^3 dy = R(\theta_B)_n^3 |2\delta\theta_n|. \qquad \text{Equation 5.5}$$

$R(\theta_B)_n^3$ is the Bragg-peak reflectivity at θ_B, which corresponds to $R(0)_E^3$ in the y-scale. The rectangular shape of the Ewald function in the range $|y| \leq 1$ allows one to consider $I(y)_{peak,n}$ as a product of the Bragg-peak reflectivity and its θ-resolution $2\delta\theta_n$, which is important for the experimental measurements. Table V.1 contains $2\delta\theta_n$, $2\delta\theta_n^*$ and $exp\{-W_n\}$ calculated for $Si(220)$ at $\theta_B = 69.83^o$ using the following parameters $b_{c,Si} = 0.415 \times 10^{-4}$Å, $|F(220)| = 8$, $V_0 = 160.19$ Å^3 and $B = 0.45 \pm 0.02$ Å^2 at $T = 293^o K$.[6,7] The θ-resolution gain factor $g_n = \delta\theta_n^* / \delta\theta_n$, also shown in Table V.1, demonstrates the effect of the atomic vibrations on $2\delta\theta_n$, the maximum of which at $n = 8$ is as great as $g_8 \approx 6.7$.

Rocking Curve Measurements

The experimental $2\delta\theta_{n,exp}$ for $n = 1 - 4$ are obtained from rocking curves measured at the empty MW-USANS instrument used in the dynamical diffraction study as a multi-wavelength double-crystal diffractometer (MW-DCD). Figure V.2 shows the optics scheme of the MW-DCD consisting of the $Si(220)$ channel-cut triple-bounce monochromator (M) and analyzer (A) crystals and the detectors. The crystal goniometers are mounted on a vibration isolated granite table and the instrument room temperature stability is kept with the accuracy $\Delta T \approx \pm 0.2\ ^oC$.

Table V.1 - The effect of the atomic vibrations on $2\delta\theta_n$, calculated for $Si(220)$ at $\theta_B = 69.83^o$

n	λ_n, Å	$\exp\{-W_n\}$, $B = 0.45$ Å^2	$2\delta\theta_n^*$, $arcsec$	$2\delta\theta_n$, $arcsec$	g_n
1	3.6	0.970	5.40	5.24	1.03
2	1.8	0.885	1.35	1.20	1.13
3	1.2	0.760	0.60	0.46	1.30
4	0.9	0.614	0.34	0.21	1.62
5	0.72	0.466	0.22	0.10	2.20
6	0.6	0.334	0.15	0.05	3.00
7	0.514	0.224	0.10	0.024	4.17
8	0.45	0.142	0.08	0.012	6.67

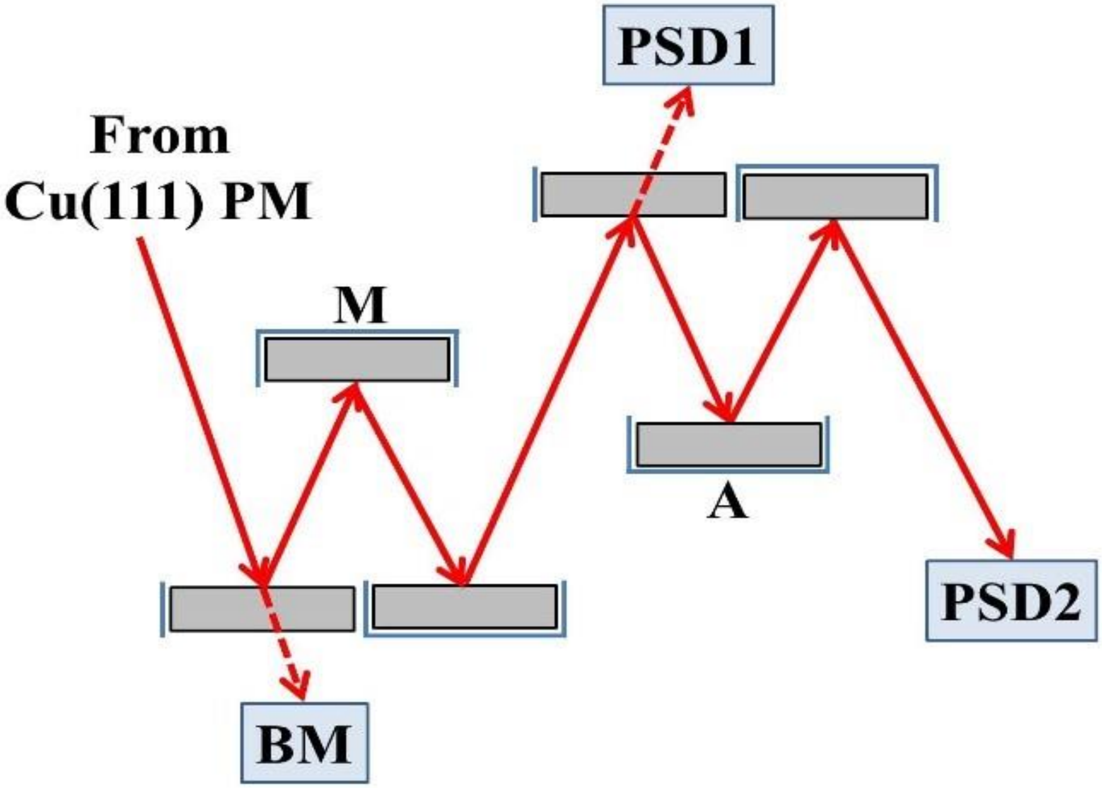

Figure V.2 - The optical scheme of the MW-DCD on $Si(220)$ M and A triple-bounce crystals with the cadmium shielding (blue lines). BM is the N beam monitor and PSD 1, 2 are the ^{3}He position sensitive detectors.

The Courtois-Mutti 2D-focusing pre-monochromator (PM) on $Cu(111)$ mosaic crystals, which is not shown in Figure V.2, is a secondary source of neutron radiation for the MW-DCD. This optical component set up for the matched Bragg angle $\theta_{B,PM} = 59.6^{o}$ generates the spectrum of Bragg reflections from the $Cu(111)$ family separated in time-of-flight (TOF) and focuses the beam at the sample position. The TOF technique is used to select the order of Bragg reflection n and integrate the peak intensity in $\lambda_{min,n} \leq \lambda_n \leq \lambda_{max,n}$. The peak intensity also is integrated over the illuminated area of the PSD2 (Figure V.2); therefore, the rocking curve measurements at the MW-DCD are similar to that at the single-wavelength reactor-based DCD. The systematic error of this experiment is estimated as $\Delta\delta\theta_{n,exp}/\delta\theta_{n,exp} \approx \pm 5\%$.

The rocking curve studies are made by executing $(\theta_B \pm \theta)$ scans of the $Si(220)$ A and fitting the experimental data by the conventional formula, Equation 5.6. Here $I(\omega)$

$$I(\omega) = \int R_M(y) R_A(y+\omega) dy. \qquad \text{Equation 5.6}$$

is the convolution of the monochromator $R_M(y)$ and the analyzer $R_A(y)$ reflectivity functions $R_M(y) = R_A(y) = R_{E,n}^{3}\left(\frac{|\theta-\theta_B|}{\delta\theta}\right)$. An example of data analysis for $n = 2, \lambda_2 = 1.8$ Å is shown in Figure V.3 and the numerical $2\delta\theta_{n,exp}$ and $g_{n,exp} = \delta\theta_n^*/\delta\theta_{n.exp}$ for $n = 1 - 4$ are given in Table V.2 along with $2\delta\theta_n^*$ and $2\delta\theta_{,n}$.

Comparing $2\delta\theta_{n,exp}$ with $2\delta\theta_n$ one can note that the difference $\varepsilon_n = 2\delta\theta_{n,exp} - 2\delta\theta_n$ is nearly identical and ε_n averaged over $n = 1 - 4$ is $< \varepsilon_n > \approx 0.055$ $arcsec$. This broadening of $2\delta\theta_{n,exp}$, as has been convincingly established from independent tests of the MW-DCD, is a parasitic effect caused by drift of the monochromator and analyzer goniometers with

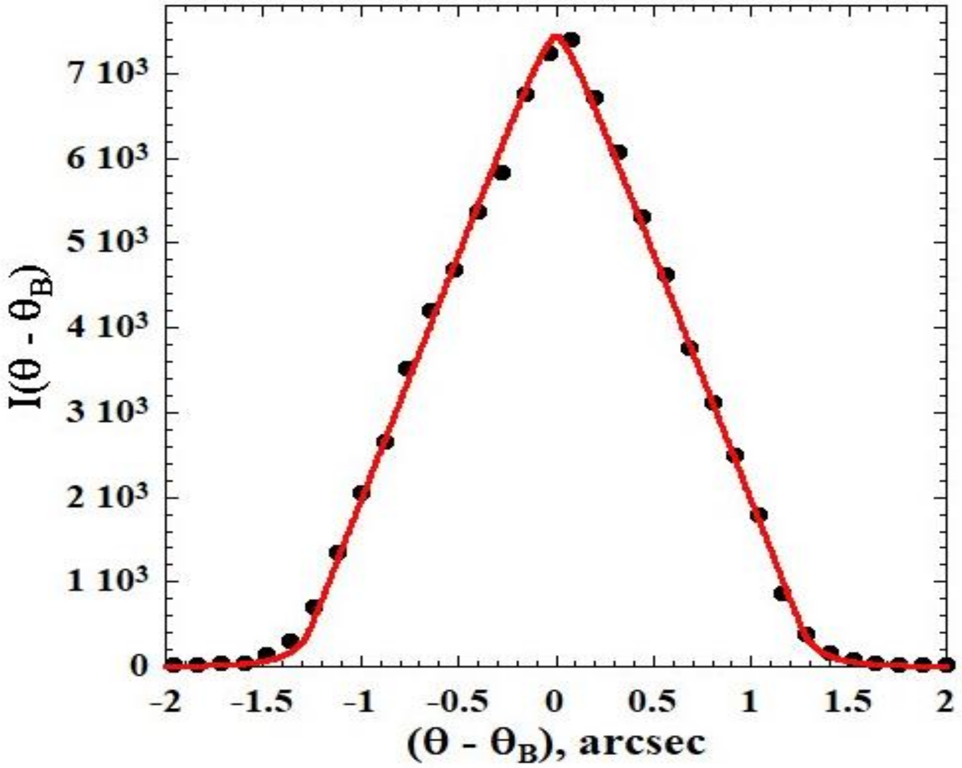

Figure V.3 - The experimental (black closed circles) and fitting (red solid line) rocking curves obtained for $n = 2$.

Table V.2 - The numerical $2\delta\theta_{n,exp}$ and $g_{n,exp} = \delta\theta_n^*/\delta\theta_{n.exp}$ for $n = 1 - 4$, associated with $2\delta\theta_n^*$ and $2\delta\theta_{,n}$.

n	$2\delta\theta_n^*$,$arcsec$	$2\delta\theta_n$, $arcsec$	$2\delta\theta_{n,exp}$, $arcsec$	$g_{n,exp}$
1	5.40	5.24	5.30±0.06	1.02±0.05
2	1.35	1.20	1.26±0.06	1.07±0.06
3	0.60	046	0.51±0.026	1.18±0.06
4	0.34	0.21	0.25±0.012	1.36±0.05

respect to each other due to the room temperature fluctuation $\Delta T \approx \pm 0.2\ ^{o}C$. The DP width $2\delta\theta_5 = 0.1\ arcsec$ becomes comparable with $< \varepsilon_n > \approx 0.055\ arcsec$, which makes impossible the rocking curve measurements in the range $n = 5 - 8$. It is worthy to note that $2\delta\theta_{n,exp} - < \varepsilon_n >$ corrected for the parasitic drift are in excellent agreement with $2\delta\theta_n$ calculated for $n = 1 - 4$.

TOF Spectra Measurements

The Bragg-peak reflectivity of the $Si(220)$ triple-bounce crystal estimated from the rocking curve study is $0.97 \leq R(\theta_B)^3_{n,exp} \leq 0.87$ does not change significantly in the range $n = 1 - 4$. However, it is reasonable to expect the Bragg-peak reflectivity loss below $\lambda_n = 0.9$ Å because the thermal diffuse scattering (TDS) grows with the decrease of wavelength.[8,9] Therefore, the MW-DCD instrument is reconfigured to probe the loss of $R(\theta_B)^3_{n,exp}$ at $n = 5 - 8$ by comparing the TOF spectra of the $Si(220)$ M and $Cu(111)$ PM matched at $n = 4$. In this setup the $Si(220)$ A is removed from the instrument and the $Cu(111)$ PM and $Si(220)$ M are fixed at the exact corresponding Bragg angles. The$Si(220)$ M and $Cu(111)$ PM spectra are detected by the BM and PSD1 as shown in Figure V.2; both of the detectors are calibrated, and the experimental data corrected for the detector efficiency. The TOF measurements are free of mechanical movements and also cannot be affected by the temperature drift because the full-width half-maximum of the $Cu(111)$ PM rocking curve is much greater than the $2\delta\theta_n$ of $Si(220)$ M.

The TOF approach is based on the fact that in λ-space the wavelength resolution $\Delta\lambda_n$ does not depend on the regime of diffraction because the Bragg rule $\lambda_n = 2d_n sin\theta_B$ is applicable for the $Cu(111)$ mosaic crystal as well as for the $Si(220)$ single crystal. The relative λ-resolution can be calculated by the conventional formula $\frac{\Delta\lambda_n}{\lambda_n} = ctg\theta_B \Delta\theta$, where the Bragg angle for $Si(220)$ M is $\theta_{B,M} = 69.63^o$ and for the $Cu(111)$ M $\theta_{B,PM} = 59.6^o$. Therefore, the $\Delta\lambda_n$ for both of the crystals is similar with the accuracy $\sim \pm 0.1\%$. This similarity reflects a fact that the $Si(220)$ single crystal does not change the λ-resolution significantly but sets up a strong $\theta - \lambda$ correlation instead. The similarity of corresponding Bragg peaks at the $Cu(111)$ PM and $Si(220)$ M spectra offers an opportunity to probe $R(\theta_B)^3_{n,exp}$ for $n = 5 - 8$ using the Equation 5.7. Here

$$R(\theta_B)^3_{n,exp} = R(\theta_B)^3_{4,exp}\left[\frac{\delta\theta_4 I(\lambda_n)_M}{\delta\theta_n I(\lambda_n)_{PM}}\right]. \qquad \text{Equation 5.7}$$

$R(\theta_B)^3_{4,exp} \approx 0.87$ for $n = 4$ estimated from the rocking curve measurements and $I(\lambda_n)_{PM}$ is the Bragg-peak intensity of the Cu(111) PM. Figure V.4 shows spectra of the $Cu(111)$ PM (red opened circles) and $Si(220)$ M (black closed circles) matched at $\lambda_4 = 0.9$ Å. The Bragg-peak intensity of $Si(220)$ M $I(\lambda_n)_M$ for $n = 4 - 8$ normalized as $\frac{\delta\theta_4}{\delta\theta_n} I(\lambda_n)_M$ are shown by blue crossed squares connected by a dashed line. Because $I(\lambda_4)_M = I(\lambda_4)_{PM}$, the ratio between $\frac{\delta\theta_4}{\delta\theta_n} I(\lambda_n)_M$ and $I(\lambda_n)_{PM}$ in the range $n = 5 - 8$ gives the $R(\theta_B)^3_{n,exp}$ loss caused by the TDS with respect to $R(\theta_B)^3_{4,exp} \approx 0.87$. The numerical values of $R(\theta_B)^3_{n,exp}$ obtained by (5), $2\delta\theta_{n,exp}$and $g_{n,exp}$ for $n = 5 - 8$ are given in Table V.3.

The TDS spreads over $\pm 5^o - 10^o$ in the angular space[8,9] with respect to the elastic dynamical Bragg reflections from $Si(220)$ M confined in 0.1 – 0.012 *arcsec* in the range $n = 5 - 8$ (see column 3 in Table V.3). Therefore, the TDS generates a flat background in the vicinity of $Si(220)$ M Bragg reflections the intensity of which is several orders of

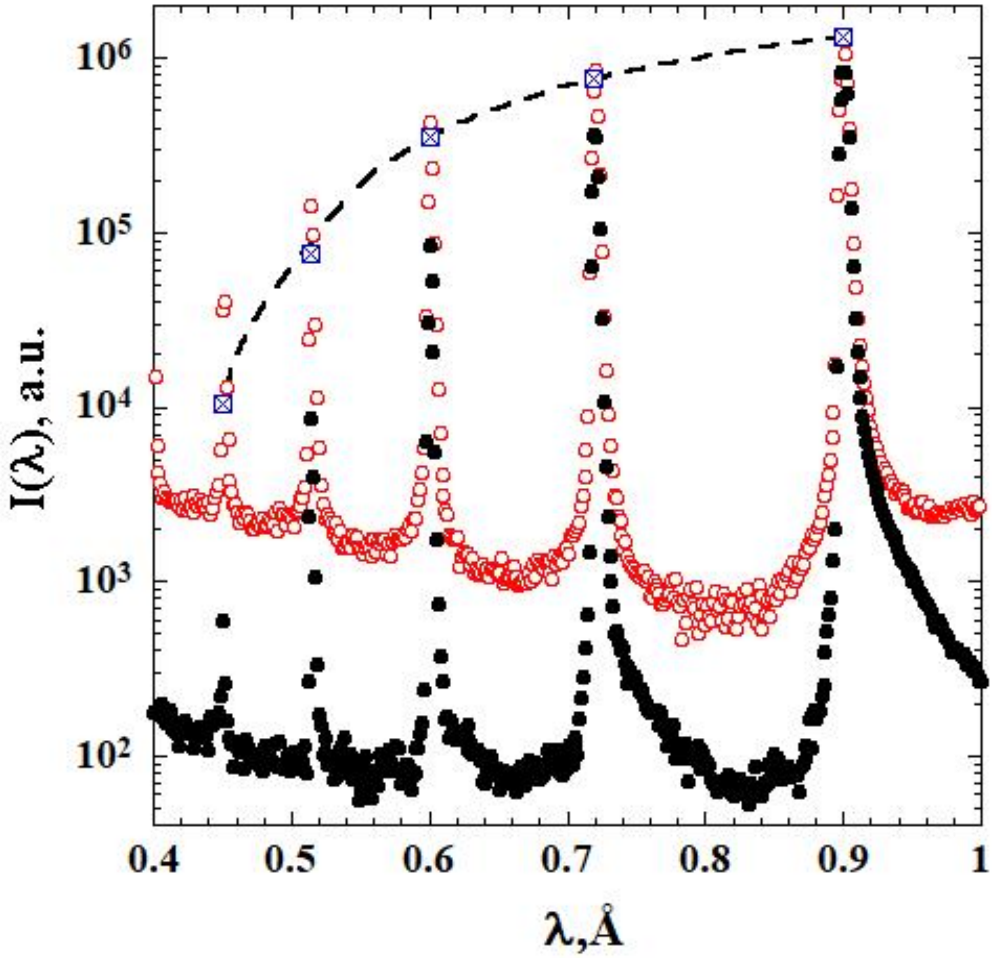

Figure V.4 - Spectra of the $Cu(111)$ PM (red open circles) and $Si(220)$ M (black closed circles) matched at $\lambda_4 = 0.9$ Å. The Bragg-peak intensities $\delta\theta_4 I(\lambda_n)_M/\delta\theta_n$ normalized for $n = 4$ are shown by blue crossed rectangles connected by the dashed line.

Table V.3 - The numerical values of $R(\theta_B)^3_{n,exp}$ obtained by (5), $2\delta\theta_{n,exp}$ and $g_{n,exp}$ for $n = 5 - 8$

n	$R(\theta_B)^3_{n,exp}$, $arcsec$	$2\delta\theta_{n,exp}$, $arcsec$	$g_{n,exp}$
5	0.78±0.04	0.1015±0.0005	2.17
6	0.66±0.03	0.0515±0.0005	2.91
7	0.46±0.02	0.0261±0.0005	3.85
8	0.20±0.01	0.0130±0.0005	6.15

magnitude lower than the corresponding $R(\theta_B)^3_{n,exp}$. This background does not change the shape of the Ewald function $R(y)^3_E$ (Figure V.1) but reduces only the Bragg-peak reflectivity $R(\theta_B)^3_{n,exp}$. The decrease of $R(\theta_B)^3_{n,exp}$ leads to broadening of $2\delta\theta_{n,exp}$ as shown in Figure V.1 for $n = 8$ as $2\delta\theta_8$; the corresponding numerical experimental data including $g_{n,exp}$ are given in Table V.3. The final result presented in Figure V.5 demonstrates the growth of the θ-resolution gain with the increase of n caused by the atomic vibration at ambient temperature, which reaches the maximum $g_{8,exp} \approx 6$ at $n = 8$. However, the atomic vibration also generates the parasitic TDS which grows with the increase of n causing significant loss of the Bragg-peak reflectivity which at $n = 8$ is $R(\theta_B)^3_{8,exp} = 0.2$.

Summary

These rocking curve measurements demonstrated unique capability of the MW-USANS instrument to span $2\delta\theta_{n,exp}$ from 5.3 $arcsec$ to 0.25 $arcsec$ for $n = 1 - 4$ without changing the Bragg angle. The θ-resolution of the MW-USANS instrument at $n = 4$ is 6.2 times higher than that for the reactor-based BT-5 USANS instrument at NIST[10] and 4.2 times greater than the θ-resolution of the USANS instrument Kookaburra at ANSTO.[11] However, in our opinion the most interesting result of this study, which could possibly find broad application in advanced X-ray and neutron optical devices, is the significant θ-resolution gain related to the decrease of the bound coherent scattering amplitude b_c in the range $n = 5 - 8$ by the atomic vibration at $T = 293^o K$. It is reasonable to emphasize that the amplitude of atomic vibration depends on temperature and as a result the DWF, $exp\,\{-W_n = \frac{Q_n^2 u(T)^2}{2}\}$, can also be controlled by T.[6, 7] The mean-square atomic displacement $u(T)$ increases with the

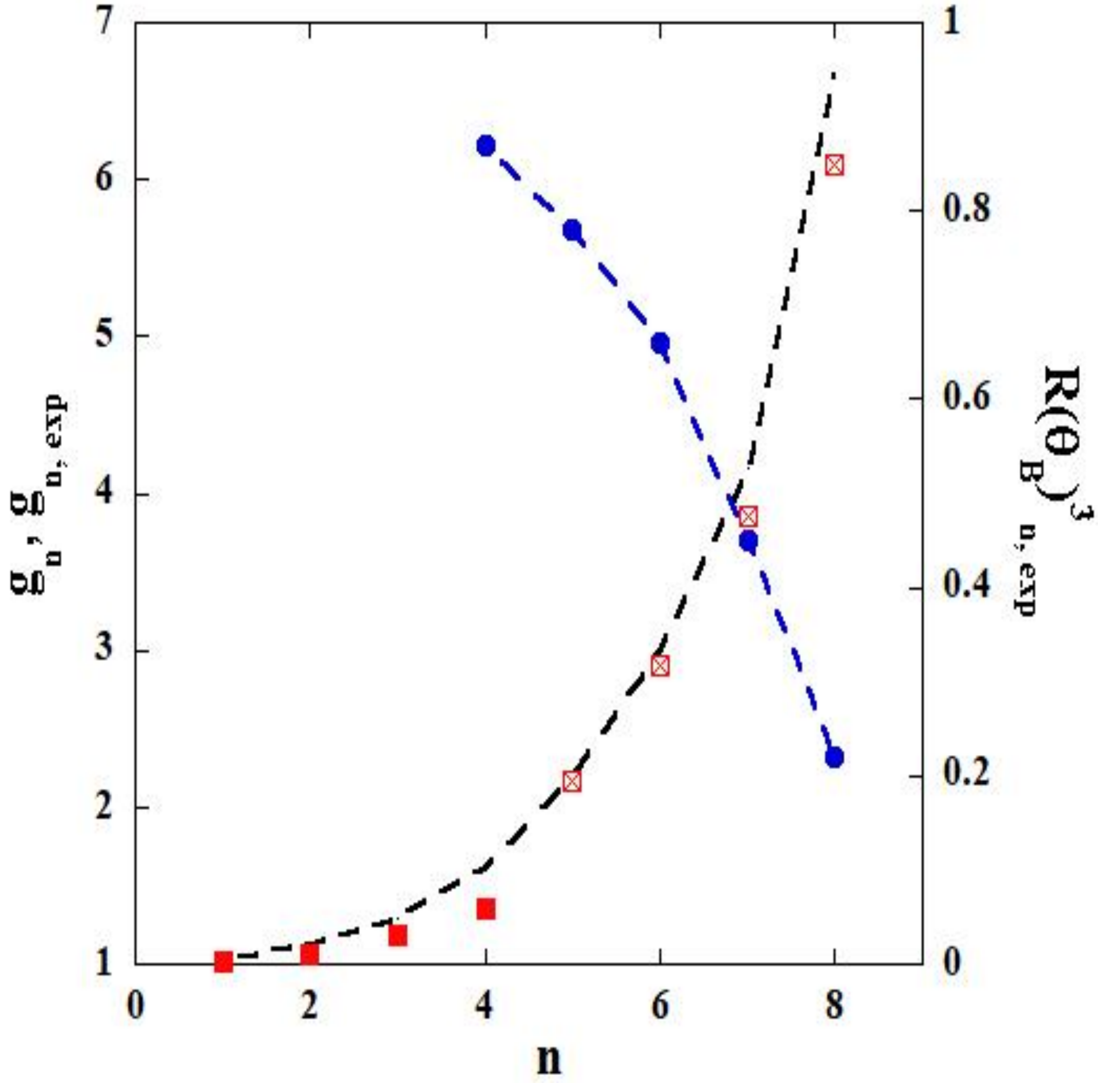

Figure V.5 - The theoretical $g_n$for $n = 1 - 8$ (black dashed line), experimental $g_{n,exp}$ for $n = 1 - 4$ (red squares) and $g_{n,exp}$ for $n = 5 - 8$ (red crossed squares). The $R(\theta_B)^3_{n,exp}$ for $n = 4 - 8$ is given by blue circles connected by the dashed line.

increase of T; therefore, heating the monochromators operating in the dynamical Bragg diffraction regime leads to the θ-resolution gain $g(T)_n$ at a given n. This dynamical diffraction effect is remarkable because it is known that heating of mosaic crystal-monochromators only decreases the Bragg-peak reflectivity without noticeable effects on θ-resolution. However, the parasitic Bragg-peak intensity loss affects these results; Figure V.5 shows that $R(\theta_B)^3_{n,exp}$ decreases significantly in the range $n = 5 - 8$, which correlates with the increase of $g(T)_n$. Therefore, it would be interesting to conduct further experiments on single crystal-monochromators with temperature variation leading to the development of new neutron and X-ray optical components controlled by temperature.

Acknowledgements

The author is thankful to M.A. Agamalian, J. M. Carpenter, P. Courtois, P. Mutti, A. D. Stoica, K. C. Littrell, A. Kolesnikov and A. Podlesnyak for discussions of the results and fruitful notes. This research used resources (USANS-BL1A) at the Spallation Neutron Source, a DOE Office of Science User Facility operated by the Oak Ridge National Laboratory.

References

1. H. Rauch and S. A. Werner, Neutron Interferometry, Clarendon Press, Oxford (2000).

2. M. Agamalian, T. Imae *et al.*(eds), Ch. 2.1.3.1, Neutrons in Soft Matter, J. Wiley & Sons Inc., p. 73-94 (2011).

3. R. Triolo & M. Agamalian, L. Liang *et al.* (eds), Ch. 20, Neutron Application in Earth, Energy & Environmental Sciences, Springer, p. 571-594 (2009).

4. Ch. Rehm & M. Agamalian, Neutron News, 24, 15 (2013).

5. Carpenter, J. M.; Agamalian, M.; Littrell, K. C.; Thiyagarajan, P.; Rehm, C. Time-of-flight implementation of an ultrasmall-angle neutron scattering instrument. Journal of Applied Crystallography 2003, 36, 763-768

6. V. F. Sears & Shelley, Acta Crystallogr., 30, 345 (1997).

7. C. Flensburg & R. F. Stewart, Physical Review B, 60, 284 (1999).

8. M. Agamalian, J. M. Carpenter & J. W. Richardson, Physics Letters, A 373, 292 (2009).

9. M. Agamalian, J. M. Carpenter & W. Treimer, J. Appl. Cryst., 43, 900 (2010).

10. J. G. Barker. C. J. Glinka, J. Moyer, M. H. Kim, A. R. Drews & Agamalian, J. Appl. Cryst., 38, 1004 (2005).

11. Ch. Rehm, L. de Campo, A. Brule, F. Darmann, F. Bartsch & A. Berry, J. Appl. Cryst., 51, 1 (2018).

Chapter VI Conclusions and Future Work

The advancement of energy research has required a combination of development of novel materials and application of multiple techniques, such as neutron scattering, to determine the structure of materials and further enhance energy related capabilities. Neutron scattering techniques such as small-angle neutron scattering (SANS), ultra-small-angle neutron scattering (USANS), diffraction, and reflectometry have been used to determine structure and assembly of conjugated polymer Poly(3,4-ethylenedioxythiophene):poly(styrene sulfonate) (PEDOT:PSS) blends, surface induced layering of Tween-20/1-butanol surfactant in D_2O and toluene microemulsions, and hydrogen bond networks in choline chloride: glycerol mixtures leading to deep eutectic solvents.

Polymer Blends

PEDOT:PSS is known to form domains when cast as a film onto a surface, that can be preserved upon annealing of the film. The addition of dimethyl sulfoxide (DMSO) to the pre-cast solution breaks up the large aggregates formed when blending PEDOT and PSS. This disruption allows the formation of smaller PSS domains with well aligned PEDOT fibrils in the presence of only 1wt.% DMSO in the solution with consistent decrease in domain size up to 5wt.% DMSO. The smaller, well-packed domains increase the surface area available between the polymers and enable increased conductivity within the polymer blend film. The morphological changes in PEDOT:PSS are independent of deposition method as the addition of DMSO to the pre-cast solution changes the domain size and fibril realignment consistently in both spin-cast and ultra-sonic spray cast films. The consistent change in the blends demonstrate that by spin-casting a solution into a film, as opposed to ultra-sonic spray casting the solution, faster evaporation times trap the PEDOT fibrils into smaller PSS domains, that can be associated with increased conductivity of the film.

Microemulsions

Bicontinuous microemulsions (BME) form by the assembly of surfactant boundaries between water and oil sub-phases. Neutron reflectometry indicates that these microemulsions (ME) of D_2O/Tween-20/1-butanol/toluene form layers that resemble perforated lamellae, or well-defined layers of water a that have channels of the oil separated by a surfactant boundary, or vice versa, at a surface that varies with the composition of the ME. These lamellae in ME's with higher water content often appear more perforated and are also significantly thicker, while lower water content ME's form layers that are purer, tend to be thinner and have larger fluctuations between D_2O-rich and oil-rich solutions. The presence of the thinner layers combined with the purity of each lamellae creates pathways for charge transfer across the surfactant within the system as well as between the ME and an electrode.

Electrode surfaces are often amphiphilic platinum or glassy carbon. Measuring the structure of microemulsions by reflectometry on surfaces that have comparable amphiphilicity, an oil and surfactant layer is observed at this surface with lamellae forming between the surface and the bulk material. While hydrophilic surfaces also form lamellae, the thick D_2O-rich layers inhibit the formation of inter-subphase pathways that will also prevent charge transfer. The increase in number of thinner layers observed in 30% D_2O microemulsions on an amphiphilic surface should allow increased charge transfer at both the surfactant boundary and the electrode surface.

Deep Eutectic Solvents

Mixture of choline chloride (ChCl) in glycerol leading up to Glyceline, a deep eutectic solvent (DES) of 33% ChCl: glycerol, have been analyzed by co-analyzing wide angle neutron scattering and molecular dynamic simulations. Neutron diffraction combined with molecular dynamics enables better models of the system to be built, allowing increased efficiency of scattering experiments. The structural changes observed in diffraction data match closely with the trends of the molecular dynamics, however, it has been shown that interactions of deuterated glycerol dominate the scattering data. While the choline and chloride interactions within the mixtures are less prominent in scattering data they are defined, and molecular dynamic simulations show the behavior of these molecules to be important.

Transitions in the structure of the glycerol: glycerol network are observed using fully deuterated glycerol and partially deuterated choline chloride in the mixtures, where the data indicate that the chloride anion disrupts the glycerol hydrogen bond network. While the glycerol: glycerol interactions decrease, there is a substantial increase in choline: choline interactions suggesting that hydrogen bonds between choline molecules are forming, freeing the chloride to interact with the glycerol methylene groups and possibly form hydrogen bonds with the glycerol hydroxyl groups.

Atomic Vibrations

Improving the ability to collect and analyze data is required to advance the development of energy materials. Increasing efficiencies of ultra-small-angle neutron scattering (USANS) allows more productive experiments to be performed. The recent development of USANS at ORNL has shown that reduction of vibrations in silicon monochromator and analyzer crystal pairs combined with the ability to measure over multiple wavelengths improves the θ-resolution of the instrument, allowing a lower Q region to be measured and improving the signal-to-noise ratio of the instrument. The combined methods of improvement make USANS a more effective tool for bridging the gap between traditional nano and micromolecular measurements and macromolecular measurements.

Future Work

Several other possible improvements to time-of-flight USANS are feasible. Of these there are mechanical improvements such as increased control of the temperature between the monochromator and analyzer crystals, improved motor controls, and further reduction of vibrations within the crystals. Increased control of the monochromator and analyzer crystals would improve the ability to match the wavelength spread and improve the θ-resolution of the rocking curves. Combined with the use of piezo-electric translation motors, the step size of the rotation on the analyzer crystal could be improved from the existing 0.003 arcseconds by an order of magnitude, leading to the possibility of measuring rocking curves of wavelength numbers 7 and 8, 0.51 Å and 0.45 Å, respectively. Reduction of the vibrations in the monochromator and analyzer crystals by further controlling the environment of the instrument with direct temperature control and housing the crystals in a controlled gas environment would further reduce the environmental effects on the crystals thereby reducing the noise in rocking curve measurements, improving the θ-resolution. Better θ-resolution could provide series of improved measurements both of the optical components of USANS and with materials studied on USANS. By building a repository of data for these measurements, machine learning could be applied to proposed material studies to select the highest quality samples, along with methodology to further advance the quality of measurements.

However, further tests that would greatly improve the performance of USANS have yet to be realized. Having precise temperature control of the crystals may allow the monochromator to be tuned to match wavelengths with the incident beam and analyzer crystal. Tuning the monochromator would improve the flux through the sample by increasing the number of neutrons reflected from the pre-monochromator. Even more so, precise control of the temperature on the monochromator would allow increased control of the mean-square atomic displacement, reducing the natural vibrations within the crystal, and the accuracy of the Debye-Waller factor measurement.

Polymer Blends

Improved instrument capabilities could lead to additional measurements on polymer blends, like PEDOT:PSS, where lower-Q Guinier plateaus could be measured as well as extending the data to higher-Q to overlap more with SANS and VSANS measurements. This would enable faster and more reliable measurements where additional thermoelectric polymer structures could be analyzed. Exploring how additional additives to the pre-deposition solution, such as ethylene glycol, may affect the structure could exemplify the results that the domain changes are occurring in pre-cast solutions as opposed to a result of the deposition method. Additionally, a thorough examination of how the polymer domains change with dimethyl sulfoxide (DMSO) and a post-annealing bath of ethylene glycol across different casting methods may show how these fibrils and domains continue to develop. The increased variation in domain size in the ultra-sonic spray cast films may absorb ethylene glycol more effectively than their spin-cast counterparts, which would allow the adaptation of the polymer blend as a performing thermoelectric material and could increase industrial production of organic thermoelectrics.

Microemulsions

The formation of lamellae within a BME at an electrode surface suggests the structure of the BME has a significant role in the transfer of charges from the ME system to the electrode. To further determine the role of the ME surface structures with an electrode, several advanced measurements can be performed. Using different contrasts such as deuterated toluene with and without D_2O, would increase the ability to determine where the oil in the ME assembles in the layers structure as compared to the surfactant and the water. Preforming these same reflectometry measurements with a redox-active agent, ferrocene, would allow static measurements of ME's as they are used in cyclic voltammetry measurements, allowing close correlation between the electrochemical performance and the structure of the ME. Lastly, in-situ electro-chemical/surface structure measurements would give an accurate portrayal of the structure during electrochemical use. This would provide insight into whether the presence of an electric charge changes the structure at the layering of the ME at the surface or how accurately the structure observed in static measurements relates to the charge transfer.

Additional ventures include using other soft matter novel electrolytes for redox flow batteries, such as Nanoscale Organic Hybrid Materials, NOHMs. NOHMs are inorganic core particles, such as silicon, grafted with a canopy of polymer chains by either ionic or covalent bonds. These chains can be on the order of 2-5nm. SANS measurements have been performed on NOHMs, but surface structures of these NOHMs have yet to be published. If structures similar to ME are formed, then polarization of the NOHMs, and other soft particles, may be a result of the presence of an electrode. On the other hand, if the structure of the bulk mixtures are maintained near the surface, then the formation of lamellae may be unique to bicontinuous microemulsions and like materials.

Deep Eutectic Solvents

Likewise, there an many possibilities of mixtures that can form DES's. To date, only a handful of the most promising mixes and DES's with the most readily available materials have been evaluated. Exploring how the structural changes in many of these promising DESs will offer insight into the assembly and structure of a variety of DES assemble as their composition approaches the eutectic point. Initial studies have shown that choline or the hydrogen bond donor may display faster dynamics on an atomic scale. Determining how the structure and interactions of these mixtures change when making different DES's would allow development of storage materials with targeted properties. Additionally, a compilation of data could be used to improve molecular dynamic simulations. Improved simulations would allow development of machine learning procedures to build models of the DES with the most defined hydrogen bond networks, that would allow focused research on developing DES for industrial use.

Summary

The improvement of analytical tools and the ability to measure higher quality data improves the quality of research that can be conducted. Combined with thorough investigations of the structures of soft matter (polymer blends, ME, DES, etc.), these efforts will advance the field of neutron scattering and its role in development of energy-related materials. These developments in both instrumentation and prospective materials can help lead to improvement in energy infrastructure making energy available to many homes through a large grid power supply. Additionally, advancement of both thermoelectrics and battery materials may, individually or combined, be developed to provide energy sources for remote locations. The efficient implementation of energy related materials and how the structure of these materials affects the electrical performance is a crucial step in reaching these goals and continues to develop.

Vita

Luke Heroux received a Bachelor's and Master's of Applied Physics from Southern Illinois University Carbondale. He is married and has two children that are the center of his life. He has been working at Oak Ridge National Laboratory (ORNL) as a Scientific Associate in Neutron Sciences since 2005, where he has contributed to the design, build, commissioning, and operations of several neutron scattering instruments. While working at ORNL, he was determined to get his PhD in Materials Science and Engineering. Upon graduation he will continue to work at ORNL to further advance his contributions to energy science.